Faculty of Informatics - Papers (Archive)

Faculty of Engineering and Information Sciences

January 2006

A Molecular Line Survey of W3(OH) and W3 IRS 5 from 84.7 to 115.6 GHz: Observational Data and Analyses

S. J. Kim
KyungHee University, Korea

H. D. Kim
University of Wollongong

Y. Lee
Taeduk Radio Astronomy Observatory, Korea

Y. C. Minh
Taeduk Radio Astronomy Observatory, Korea

R. Balasubramanyam
Raman Research Institute, Bangalore, India

See next page for additional authors

Recommended Citation

A Molecular Line Survey of W3(OH) and W3 IRS 5 from 84.7 to 115.6 GHz: Observational Data and Analyses

Abstract

We have carried out observations toward the W3 complex and G34.3+0.15 using the TRAO 14 m radio telescope to examine in detail the chemical variations occurring while molecular clouds evolve from the prestellar to the H II region phase. Observations include spectral surveys of these objects between 84.7 and 115.6 GHz; mapping observations toward W3(OH) with the emissions of CS (2−1), HCN (1−0), HNC (1−0), and HCO+ (1−0); and mapping of CS (2−1) emission toward W3 IRS 5. Chemical model calculations are used to estimate the age of W3(OH) by comparing with the fractional abundances of detected molecules. We found that G34.3+0.15 and W3(OH) are at a similar evolutionary stage, although large differences in the fractional abundances are found in CH3CN and HC3N. Overall, the properties of the detected species and abundances in three regions support the view that chemistry varies as molecular clouds evolve from a cold, collapsing phase to a high-temperature phase, such as the hot core and H II phase. Chemical model calculations for W3(OH) indicate that the evolutionary age of the cloud is 104–105 yr with temperature in the range 10–60 K.

Disciplines

Physical Sciences and Mathematics

Publication Details

Authors

S. J. Kim, H. D. Kim, Y. Lee, Y. C. Minh, R. Balasubramanyam, M. G. Burton, T. J. Millar, and D. W. Lee

A MOLECULAR LINE SURVEY OF W3(OH) AND W3 IRS 5 FROM 84.7 TO 115.6 GHz: OBSERVATIONAL DATA AND ANALYSES

SANG-JOON KIM,[1] HUN-DAE KIM,[2] YOUNGUNG LEE,[3] YOUNG CHOL MINH,[3] RAMESH BALASUBRAMANYAM,[4]
MICHAEL G. BURTON,[5] TOM J. MILLAR,[6] AND DONG-WOOK LEE[1]

ABSTRACT

We have carried out observations toward the W3 complex and G34.3+0.15 using the TRAO 14 m radio telescope to examine in detail the chemical variations occurring while molecular clouds evolve from the prestellar to the H II region phase. Observations include spectral surveys of these objects between 84.7 and 115.6 GHz; mapping observations toward W3(OH) with the emissions of CS (2–1), HCN (1–0), HNC (1–0), and HCO$^+$ (1–0); and mapping of CS (2–1) emission toward W3 IRS 5. Chemical model calculations are used to estimate the age of W3(OH) by comparing with the fractional abundances of detected molecules. We found that G34.3+0.15 and W3(OH) are at a similar evolutionary stage, although large differences in the fractional abundances are found in CH$_3$CN and HC$_3$N. Overall, the properties of the detected species and abundances in three regions support the view that chemistry varies as molecular clouds evolve from a cold, collapsing phase to a high-temperature phase, such as the hot core and H II phase. Chemical model calculations for W3(OH) indicate that the evolutionary age of the cloud is 10^4–10^5 yr with temperature in the range 10–60 K.

Subject headings: H II regions — ISM: abundances — ISM: individual (W3(OH), W3 IRS 5, G34.3+0.15)

1. INTRODUCTION

It is known that chemical properties of molecular clouds vary during their evolution. The onset of central protostars, compared with the cold dark collapsing phase, plays a critical role in driving the chemistry in the surrounding dense region by providing a high temperature and density. Molecular line surveys, among many observational techniques, are one of the most powerful methods for the investigation of the chemistry. The identified molecules, which are sensitive to various chemical reactions in the molecular clouds, can be used to investigate the formation and evolution of molecular clouds. Representative line surveys performed over the last few decades are listed in Table 1. Valuable information on interstellar chemistry and the evolution of molecular clouds has been obtained from the surveys. However, as shown in Table 1, they have been limited to a few objects, such as Sgr B2 (Cummins et al. 1986; Turner 1989; Sutton et al. 1991) and the nearby Orion-KL region (Johansson et al. 1984; Jewell et al. 1989; Turner 1989; Blake et al. 1986, 1996; Ziurys & McGonagle 1993; Schilke et al. 1997).

Recently, other sources have been chosen for molecular line surveys: the ultracompact H II region G34.3+0.15 (MacDonald et al. 1996; Kim et al. 2000); the low-mass star-forming region IRAS 16293−2422 (van Dishoeck et al. 1995); the protostellar region IRAS 17470−2853 (Kim et al. 2002); and the late-type star IRC +10216 (Kawaguchi et al. 1995; Cernicharo et al. 2000). It is important to study the sources for which significant chemical variations are expected, as predicted by models. Detailed ex-

amination has been undertaken for individual species present in Orion-KL and Sgr B2 (Turner 1991) in order to test the models. Although the results toward these two sources have provided us with interesting information on the nature of dense cores, the complex physical structure of Orion-KL and Sgr B2 has limited our understanding of the chemical processes. The molecular abundances derived from these objects contain large uncertainties due to the blending of adjacent transitions compared to low-mass and isolated objects. Therefore, Orion-KL and Sgr B2 do not provide a favorable environment for the study of relative chemical variations and ultimately for the determination of the evolutionary stage, although observations toward the objects have enabled us to understand the close relationship between the chemistry and the evolution of molecular clouds.

Observations toward the hot core (MacDonald et al. 1996) and the cold halo (Thompson & MacDonald. 1999) of the source G34.3+0.15 have revealed significant chemical variations between these two distinct physical components within this object. A distinct chemistry was also noticed from observations of SO$_2$, CH$_3$OH, and H$_2$CS (Helmich et al. 1994) and submillimeter molecular line surveys (Helmich & van Dishoeck 1997) of the W3 region.

Models of gas-phase, ion-molecule chemistry can reasonably reproduce the observed abundance of carbon-chain species in the cold dark clouds (Herbst et al. 1984; Millar & Freeman 1984). However, such ion-molecule chemical models alone cannot satisfactorily account for the observed high abundance of molecules containing H or S atoms in star-forming molecular clouds. Coupling of gas-phase and grain-surface reactions (e.g., van Dishoeck & Blake 1998) has been emphasized in recent chemical models in order to cope with the discrepancy. Representative models have been developed for hot cores by Millar et al. (1991) and by Charnley et al. (1995). According to these models, hydrogen, sulfur, ionized, and neutral molecules are readily deposited onto dust surfaces as the density increases during the collapsing phase of interstellar clouds. The formation of complex, heavy species containing hydrogen becomes inhibited, leading to slow reactions of those species in the earlier collapsing phase ($t < 10^4$ yr).

[1] Department of Astronomy and Space Science, KyungHee University, Youngin, Kyunggi 449-701, Korea; sjkim1@khu.ac.kr.
[2] School of Information Technology and Computer Science, University of Wollongong, NSW 2500, Australia.
[3] Taeduk Radio Astronomy Observatory, San 36-1, Whaam-Dong, Youseong-Gu, Taejeon 305-348, Korea.
[4] Department of Astronomy and Astrophysics, Raman Research Institute, Sadashivanagar, Bangalore 560080, India.
[5] School of Physics, University of New South Wales, Sydney, NSW 2052, Australia.
[6] Department of Physics, UMIST, P.O. Box 88, Manchester M60 1QD, UK.

TABLE 1
REPORTED MOLECULAR LINE SURVEYS

Sources	Telescope	FWHM	Frequency (GHz)	Resolution (MHz)	Line Density (Transition/GHz)	Observations
Orion A	OSO 20 m	47″	72–91	1	8.5	Johansson et al. (1984)
IRC +10216					2.3	
Orion A	OVRO 10.4 m	0.″5	247–263	1.03	15.2	Blake et al. (1986)
Sgr B2	BTL 7 m	2.″9	70–150	1	9.14	Cummins et al. (1986)
Orion A	NRAO 12 m	24″	330–360	2	5.4	Jewell et al. (1989)
Orion A	OVRO 10.4 m	0.″5	215–247	16.2	17.0	Sutton et al. (1985)
Sgr B2(M)	CSO 10.4 m	20″	330–355	1	6.7	Sutton et al. (1991)
Sgr B2/Orion-KL	NRAO 11 m	83″	70–115	1	14.3/17.1	Turner (1989)
G34.3+0.15	JCMT 15 m	13″	330–360	0.756	0.6	Thompson & MacDonald (1999)
G34.3+0.15	TRAO 14 m	58″	86–165.3	1	2.0	Kim et al. (2000, 2001)
G34.3+0.15	JCMT 15 m	14″	330–360	0.33	11.4	MacDonald et al. (1996)
G5.89−0.39................	JCMT 15 m	13″	330–360	0.756	4.7	Thompson & MacDonald (1999)
IRC +10216	IRAM 30 m	19″	129–173	1	8.6	Cernicharo et al. (2000)
IRC +10216	Nobeyama 45 m	35″	28–50	0.25	8.6	Kawaguchi et al. (1995)
Orion-KL...................	FCRAO 14 m	40″	150–160	1	18.0	Ziurys & MacGonagle (1993)
IRAS 17470−2853	Mopra 22 m	30″	90–96	0.5	3.5	Kim et al. (2002)

Radiation from the protostar then heats up the surrounding gas and grains, releasing volatile species from the dust surface back to gas phase. This stage is called the hot core phase and lasts 10^4–10^5 yr after the onset of star formation (van Dishoeck & Blake 1998).

We surveyed W3 region to investigate the chemical evolution as predicted by recent chemical models. We also observed G34.3+ 0.15 in order to identify several missing lines from a previous survey (Kim et al. 2000). In addition, high-spectral-resolution observations for molecules of interest (CS, HCO$^+$, HCN, HNC, CH$_3$CN, and CH$_3$CCH) were carried out in G34.3+0.15. The W3 region contains several objects at different evolutionary stages, and G34.3+0.15 is a well-known hot core associated with an ultracompact H II region. Our TRAO observations toward W3 and G34.3+0.15 provide us with valuable information on interstellar chemistry, because the chemical properties of these sources, differing in mass, core size, and evolutionary stage, are useful for investigating the relationships between the chemical variations and these parameters.

The contents of this paper are as follows: § 1 presents background information on line surveys, evolutionary scenarios, and models presented in the literature. In § 2, general aspects of the W3 complex, focusing on W3(OH) and W3 IRS 5, are given. In §§ 3 and 4, we present the observational procedures, line identifications, and spectral displays. In § 5, we discuss individual species of interest detected in the survey. In § 6, we discuss the chemical variations as well as the isotopic ratios of C and S atoms found from G34.3+0.15, W3(OH), and W3 IRS 5. In § 7, the cloud morphology found from CS, HCO$^+$, HCN, and HNC mappings is presented. In § 8, chemical results from model calculations are given. We summarize the results in § 9.

2. W3 COMPLEX

The W3 complex consists of several infrared sources (Wynn-Williams & Becklin 1974; Jaffe et al. 1983; Colley 1980) at different evolutionary stages and core masses. The various objects include well-developed shell structure in the H II regions (W3B, W3C, and near IRS 3 and IRS 4), and several ultracompact H II regions (W3F, W3M; and near IRS 7 and IRS 5). Strong OH and H$_2$O masers, viz. W3(OH) and W3(H$_2$O), separated by 6″ from each other, are also observed.

At least two hot cores have been revealed in W3 from observations of NH$_3$ lines (Mauersberger et al. 1988). Its distance is estimated to be 1.83 kpc, residing in the Perseus arm of the galaxy (Imai et al. 2000). Helmich & van Dishoeck (1997) performed spectral line surveys through the 345 GHz window toward W3 IRS 4, W3 IRS 5, and W3(OH). Significant differences in the physical and chemical conditions were found in IRS 4, IRS 5, and W3(H$_2$O), and the gas temperature seems highest ($T \sim 220$ K) toward W3(H$_2$O) compared with those in IRS 4 and IRS 5 (Helmich et al. 1994). High-velocity ($\Delta V = 52$ km s^{-1}) flows near W3 IRS 5 and an intermediate-velocity ($\Delta V = 26$ km s^{-1}) wing near W3(OH) are found in ^{12}CO emission (Bally & Lada 1983).

2.1. W3(OH)

The ultracompact H II region, W3(OH), is an extensively studied site for the investigation of star formation and its influence on the surrounding regions (Wyrowski et al. 1999). Three peaks are distinguished with subarcsecond resolution observations in the thermal dust continuum emission originating from the hot core region of W3(H$_2$O; Wyrowski et al. 1999). Continuum observations reveal that W3(OH) has a shell structure in the H II region (Dreher & Welch 1981). H66α, H76α, and H110α radio recombination lines having full width at half-maximum (FWHM) of 36, 41, and 69 km s^{-1}, respectively, are observed (Sams et al. 1996). H41α, CH$_3$CN [5(2)–4(2)], HCN (1–0), HCO$^+$ (1–0), and ^{13}CO (1–0) are detected with amplitudes of 0.4, 0.1, 5.9, 5.5, and 7.6 K, respectively, from observations with the Nobeyama 45 m telescope (Forster et al. 1990). Keto et al. (1992) made mid-infrared and molecular line observations of W3(OH) and compared them with G34.3+0.15.

2.2. W3 IRS 5

W3 IRS 5 is a bright infrared source with a total luminosity of $3 \times 10^5 L_\odot$ (Campbell et al. 1995) and is separated by $\sim 75''$ from W3 IRS 4, which is brighter than W3 IRS 5 in the submillimeter wavelength range (Jaffe et al. 1983). W3 IRS 5 is younger than W3(OH) and appears to be at an earlier stage, evolving toward a hot corelike object (Helmich et al. 1994). Very long baseline interferometry measurement (Imai et al. 2000) of radial velocities and proper motions of water masers in the W3 IRS 5 region reveals two groups of maser components, which are associated with at least two different outflows.

Strong ^{12}CO self-absorption and ^{13}CO and HCN emission peaks are seen toward IRS 5; the maximum ^{12}CO emission is observed toward the compact H II region; and a CS peak is found $8''$ west of the OH 1720 MHz maser (Dickel et al. 1980). The possible presence of disklike structure around a cluster of embedded stars in the mid-infrared images of IRS 5 is inferred (Persi et al. 1996). The total H_2 mass of the molecular cores associated with IRS 5 is estimated to be 1100 $M_\odot$ derived from ^{13}CO (1–0) and C^{18}O (1–0) observations (Roberts et al. 1997). A luminosity of 6.0×10^5 $L_\odot$ and a cloud mass of 1600 $M_\odot$ have been derived using 230 GHz continuum observations (Gordon 1987) for the entire complex of W3.

3. OBSERVATIONS

We carried out molecular line surveys toward W3(OH) and W3 IRS 5 using the Taeduk Radio Astronomy Observatory (TRAO) 14 m telescope between 2001 November and 2002 February. The receiver system was a low-noise SIS receiver operating in single-sideband mode. For the observations of W3(OH), the back ends were two filter banks in serial mode, each of which has a 1 MHz resolution and 256 MHz bandwidth, providing a total bandwidth of 512 MHz at each local oscillator (LO) tuning. Sensitive 250 kHz measurements toward W3(OH) and W3 IRS 5 were also performed using two 256 channel filter banks in parallel mode after completing the 1 MHz observations of W3(OH), IRAS 18450−0200, and IRAS 18335−0711.

During the observations the typical system temperature was 300 K between 85 and 110 GHz and was 600 K at 115 GHz. Position switching mode observations were carried out, taking a reference position to be $30'$ away in right ascension, which was confirmed to be free of emission. Calibration was performed using the standard chopper-wheel method, which corrects for atmospheric attenuation and scattering of forward spillover, and the intensity was derived in terms of T_A^* scale (Ulich & Hass 1976). The beam sizes of the TRAO 14 m telescope are $64''$ and $55''$ at 85 and 115 GHz, respectively.

The total on-source integration time of each LO tuning for the 1 MHz observation was 300 s, achieving channel-to-channel rms noise of 0.03–0.05 K, which is consistent with that in G34.3+ 0.15 (Kim et al. 2000). Therefore, these observations provided an opportunity to compare the chemical properties of the W3 and G34.3+0.15 regions, with data taken with the same telescope system and sensitivity. Pointing and focusing were checked using χ Cygni.

Almost all of the molecular transitions previously detected from the 1 MHz surveys toward G34.3+0.15 (Kim et al. 2000), W3(OH), IRAS 18335−0711, and IRAS 18450−0200 (this work) were also considered for the 250 kHz surveys toward W3(OH) and W3 IRS 5. We also observed selected molecules (HCO$^+$, CS, HCN, HNC, and their isotopic variants) with 250 kHz resolution toward the ultracompact H II region G34.3+0.15 to examine isotopic ratios and the HCN hyperfine ratio in detail. We measured line emissions from SO$_2$, HNCO, CH$_3$OH [0(0)–1(−1) E], and CH$_3$OH [2(1)–1(1) A−] transitions toward G34.3+0.15.

The detected molecules and their transitions show close agreement between G34.3+0.15 and IRAS 18450−0200, and between W3(OH) and IRAS 18335−0711, suggesting that physical/ chemical condition and evolutionary stage are similar. To estimate physical conditions, as well as to determine the initial parameters for chemical model calculations, mapping observations were carried out toward W3(OH) for the transitions of CS (2–1) and HCN (1–0) over $10' \times 10'$, HNC (1–0) over $8' \times 8'$, and HCO$^+$ (1–0) over $6' \times 7'$. We carried out only CS (2–1) mapping toward W3

IRS 5, because the line strengths of other species are too weak to map with the relatively large-beam size of TRAO. Mapping observations of CS (2–1) and HCO$^+$ in IRAS 18450−0200 and IRAS 18335−0711 were performed covering almost the same area as W3(OH). CS (2–1) mapping of IRAS 18450−0200 shows irregular and elongated distribution in the N-S direction, whereas for IRAS 18335−0711 spherical distribution is shown. The CS (2–1) distribution is consistent with that of 8.6 GHz radio continuum (Walsh et al. 1998). There is no report on continuum map for IRAS 18335−0711. We will present images and detailed analyses of molecular lines detected in IRAS 18450−0200 and IRAS 18335− 0711 in future work.

The source positions of W3(OH) and W3 IRS 5, and the central position of G34.3+0.15, are as follows:

$W3(OH)$.—$\alpha = 02^h23^m16\overset{s}{.}9$, $\delta = 61°38'56\overset{''}{.}4$ (1950.0; Helmich et al. 1994).

$W3\ IRS\ 5$.—$\alpha = 02^h21^m53\overset{s}{.}1$, $\delta = 61°52'20\overset{''}{.}0$ (1950.0; Helmich et al. 1994).

$G34.3+0.15$.—$\alpha = 18^h50^m46\overset{s}{.}3$, $\delta = 01°11'13\overset{''}{.}0$ (1950.0; Kim et al. 2000).

4. DATA REDUCTION AND DISPLAY

4.1. Spectra and Images

Spectra taken with the 1 MHz resolution of the 512 channels spectrometer in serial mode have been averaged and then baseline subtracted using the SPA data reduction package developed at the FCRAO observatory. Some bad channels especially at the edge of the spectra were significant at the upper frequency region when LSB mode observations were performed. The number of bad channels in the worst spectra is about 15–20, equivalent to 15–20 MHz. The total bandwidth for every observation is 512 MHz, but observations were carried out by stepping the central frequency by 500 MHz, resulting in an overlap of approximately 6 MHz between spectra.

For the 250 kHz resolution observations, the spectrometers were configured in a parallel mode, and an average of signals was taken. The typical noise in an averaged spectrum is 0.03– 0.05 K for 1 MHz data and 0.06–0.09 K for 250 kHz data. The reduced spectra presented in Figures 1 and 2 were taken toward W3(OH) with the 1 MHz and 250 kHz bandwidths, respectively. The spectra in Figure 1 were obtained by combining two neighboring spectra, giving a bandwidth of ∼1 GHz. In Figures 3 and 4, 250 kHz spectra taken from W3 IRS 5 and G34.3+0.15, respectively, are presented.

Data taken with mapping observations were made into images using the Contour and Trigrid functions in IDL, and then the images were compared with those processed using CLASS. The two images, which were drawn in terms of antenna temperature, showed a good agreement with each other. The contour maps in Figure 5 were made by taking signals stronger than 5 σ, which corresponds to 0.4 K.

4.2. Line Identification

Line identifications were made exclusively using the catalog of Lovas (1992). The catalog lists molecular transitions detected from Orion-KL, Sgr B2, and from various interstellar molecular clouds. The number of detected lines in the catalog is sufficient for the use in the line identifications of our 3 mm observations. The identified line frequencies were determined by Gaussian fitting after correcting by the corresponding Doppler shifts of −46 and −39 km s^{-1} for W3(OH) and W3 IRS 5, respectively, and then compared with the rest frequencies from the Lovas catalog.
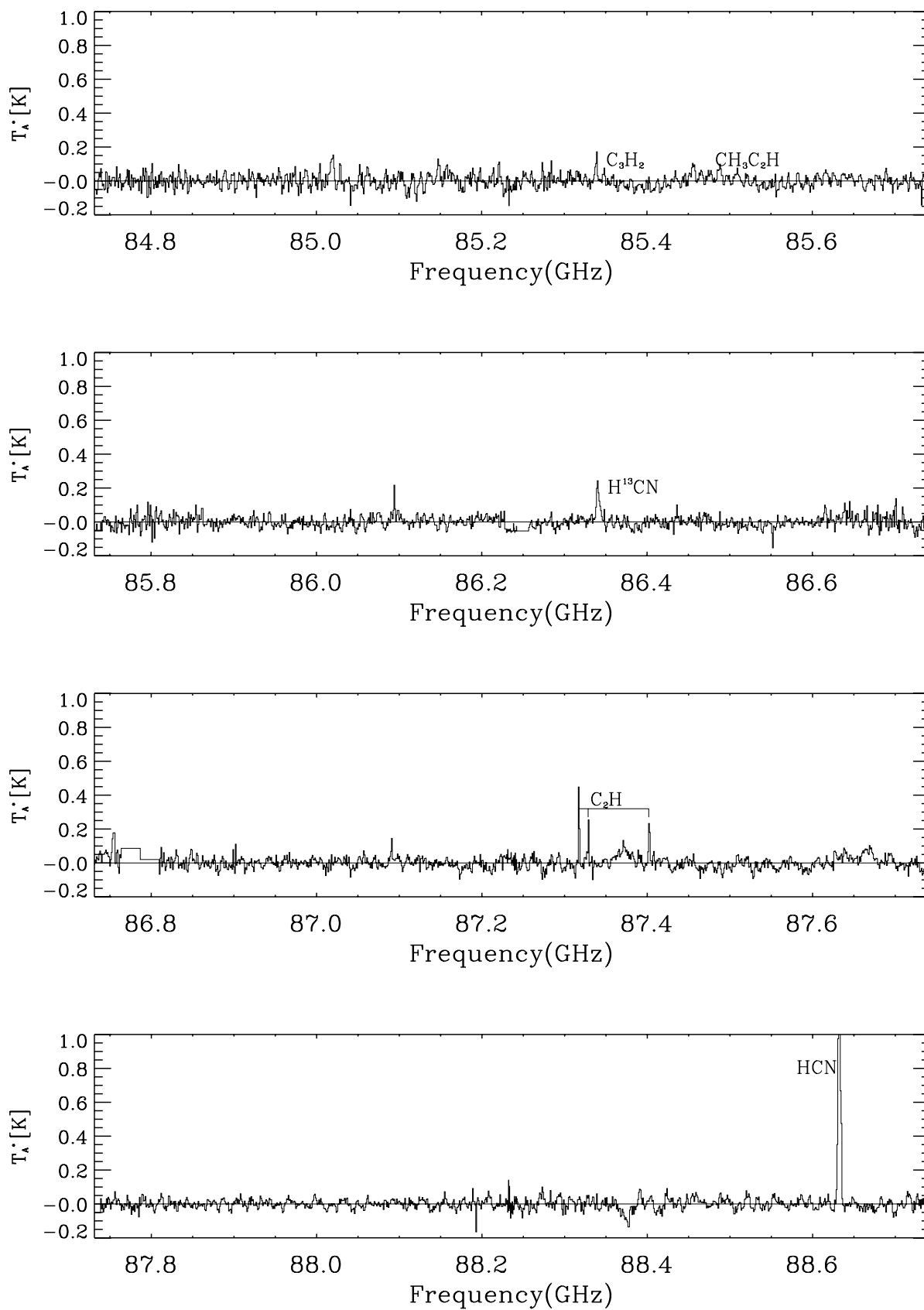
FIG. 1.—Spectra of W3(OH), from 84.8 to 115.4 GHz, obtained during 2001 November–December with the TRAO 14 m telescope. Each panel combines two neighboring frequency measurements to have about 1 GHz bandwidth.
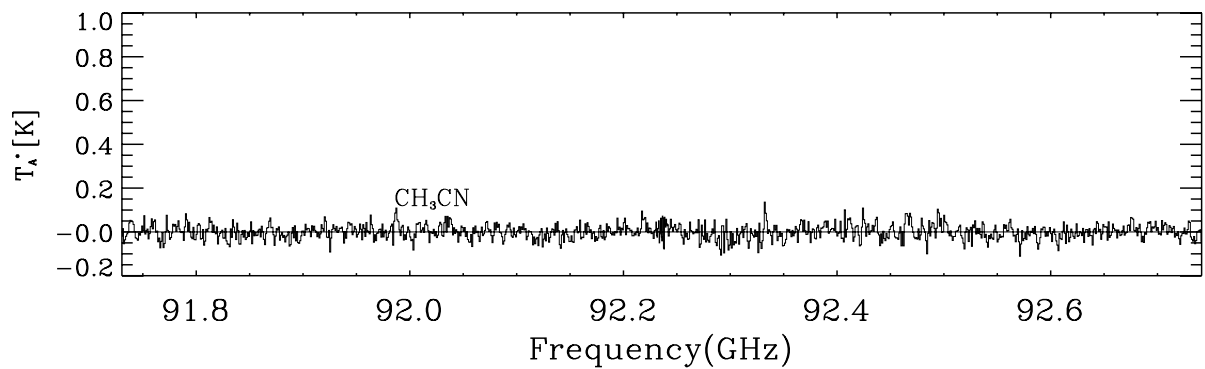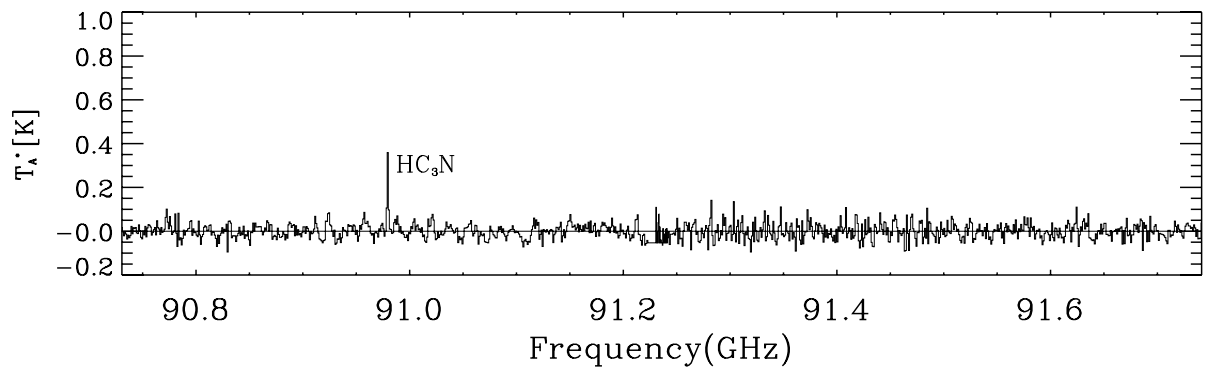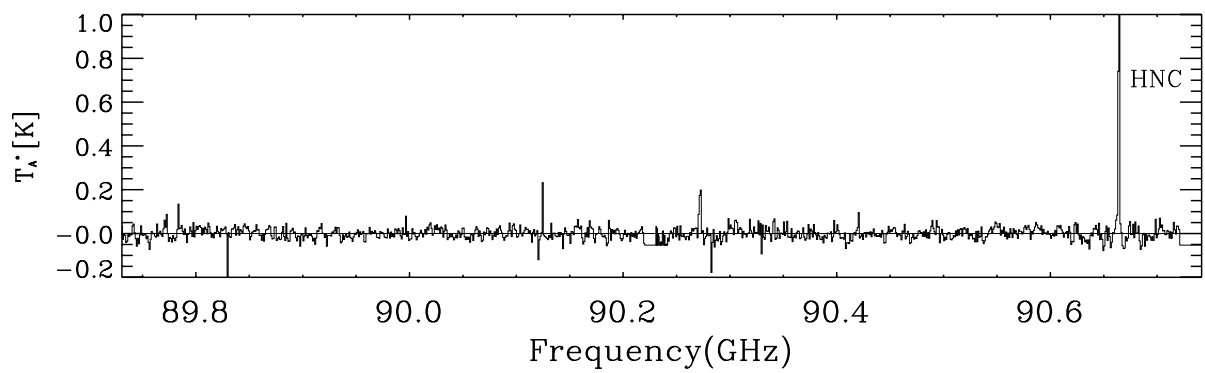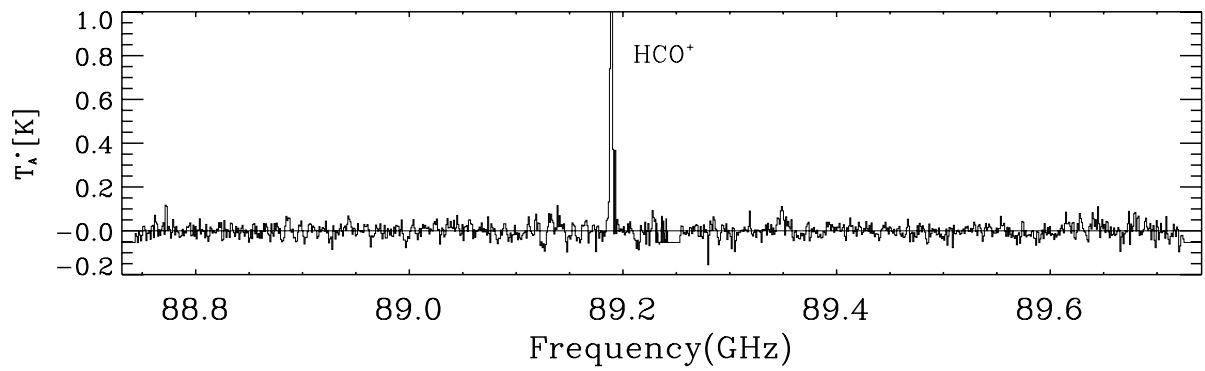
Fig. 1.—*Continued*
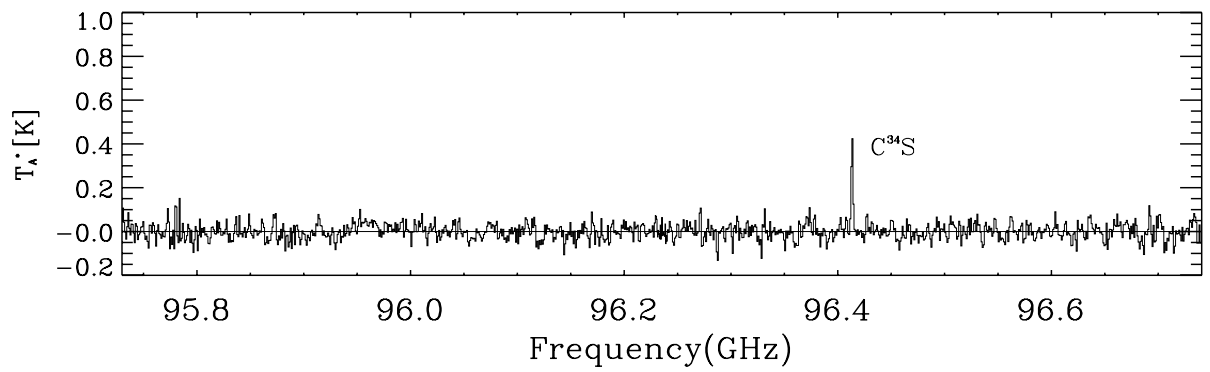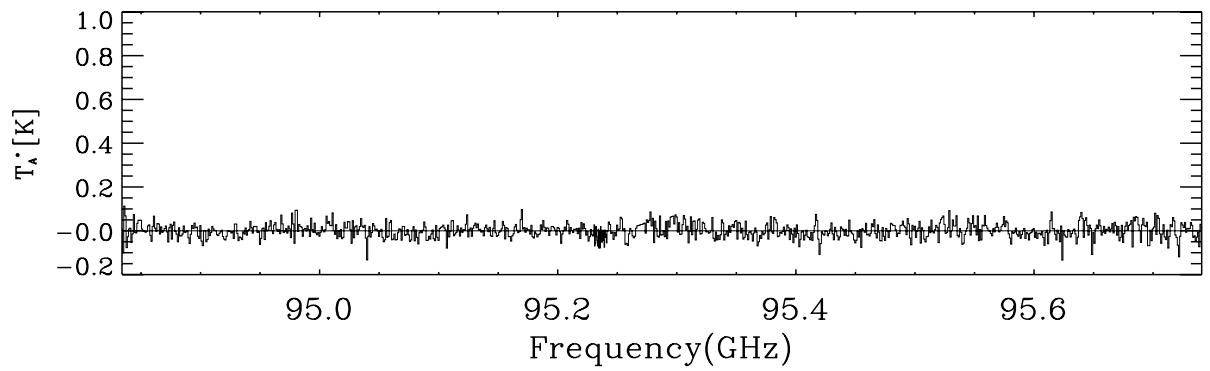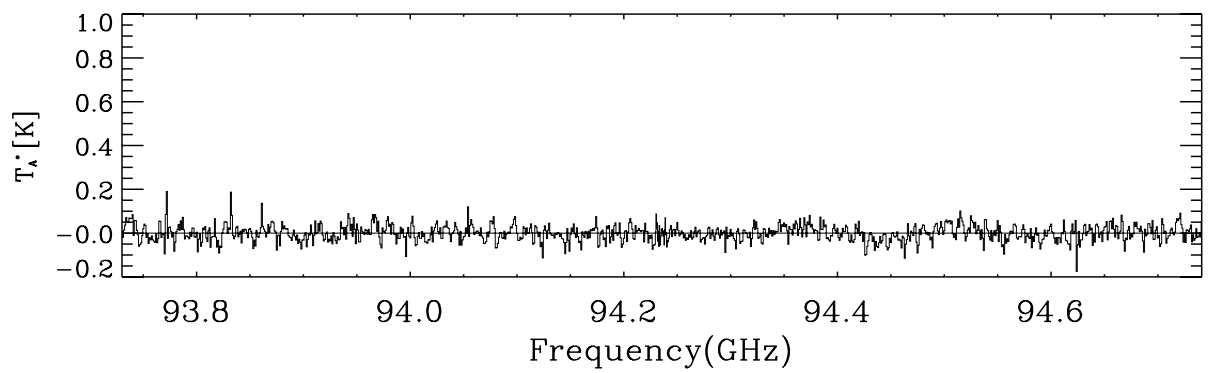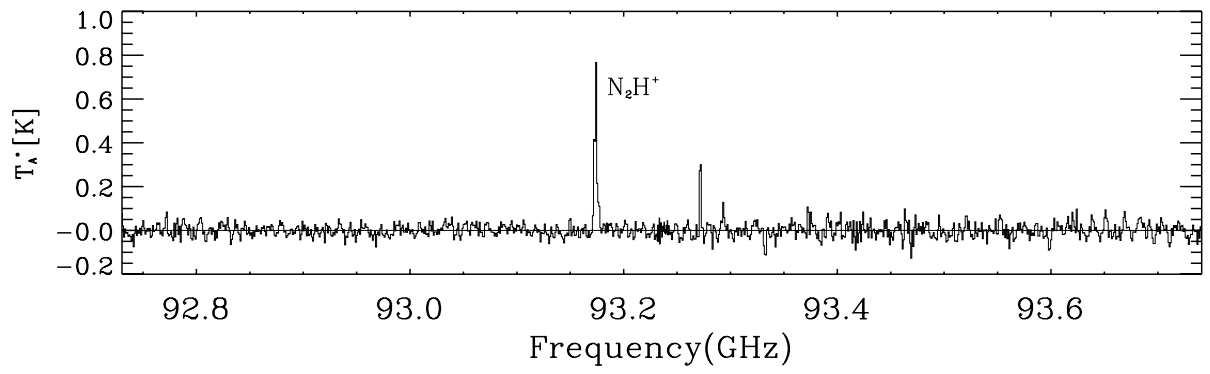
Fig. 1.—*Continued*
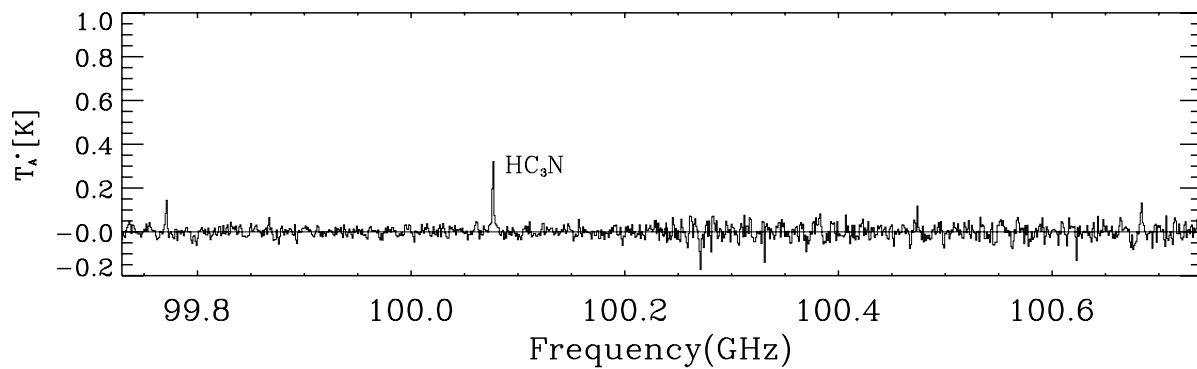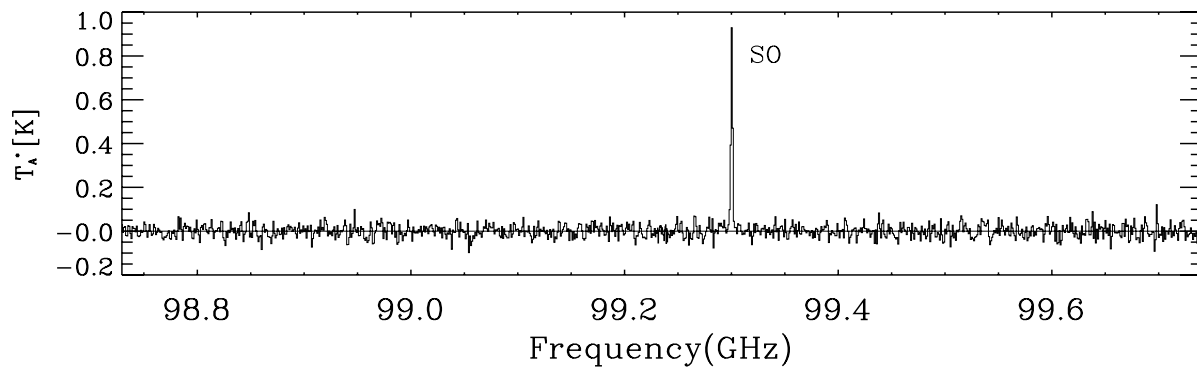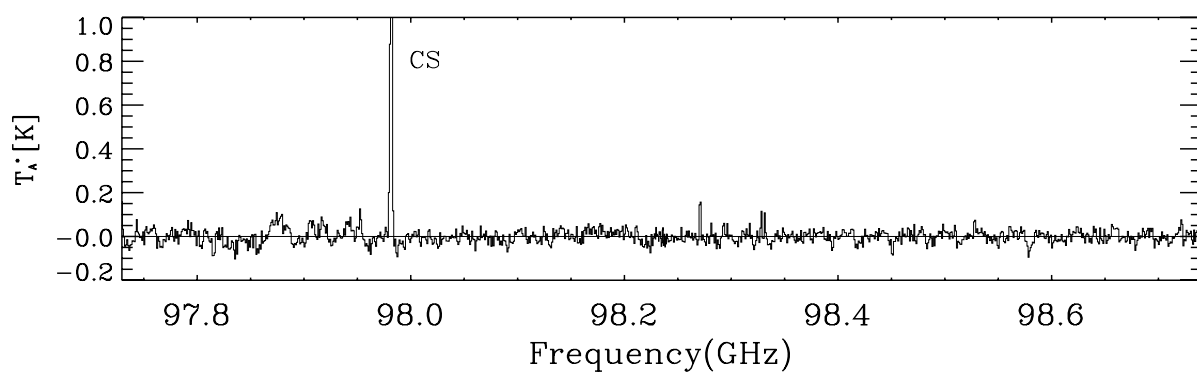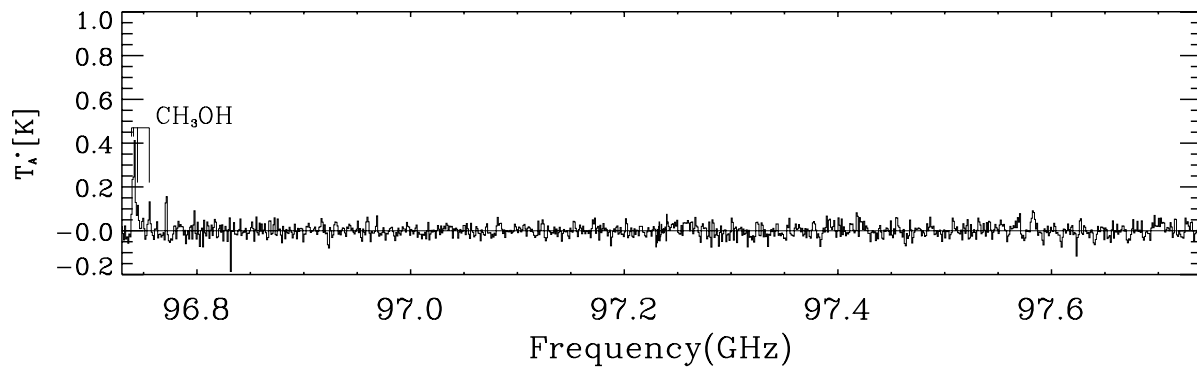
166

Fig. 1.—*Continued*

Fig. 1.—*Continued*

CH₃OH

Fig. 1.—*Continued*

169

Fig. 1.—*Continued*

FIG. 1.—*Continued*

171
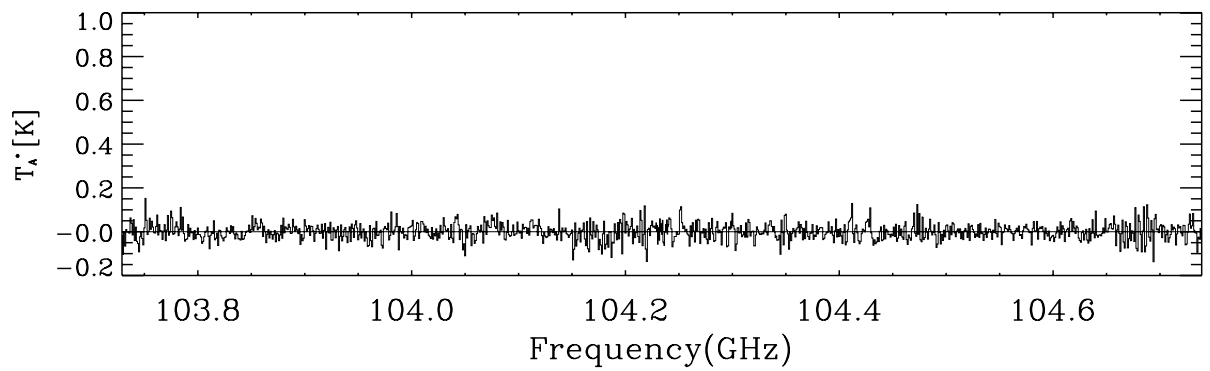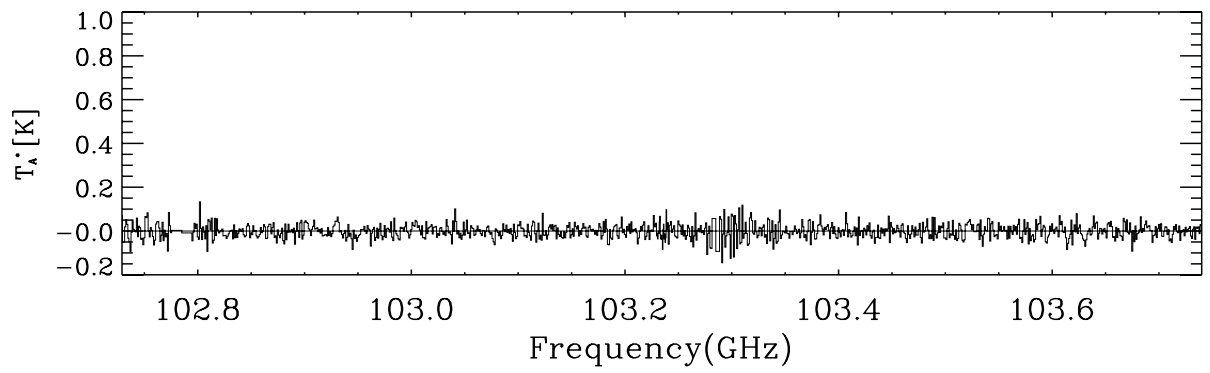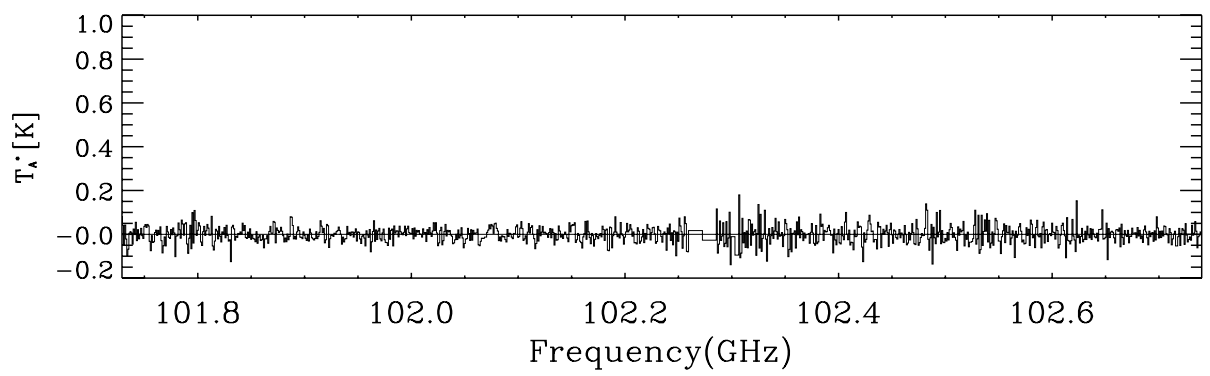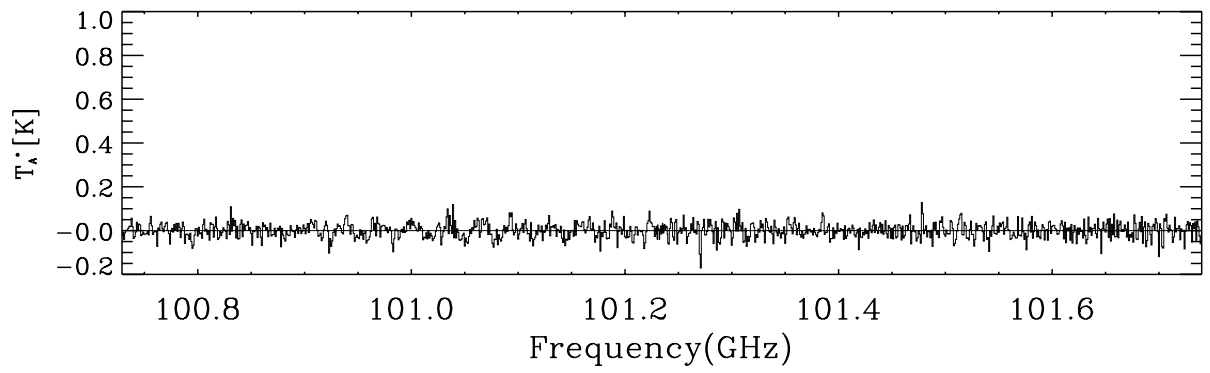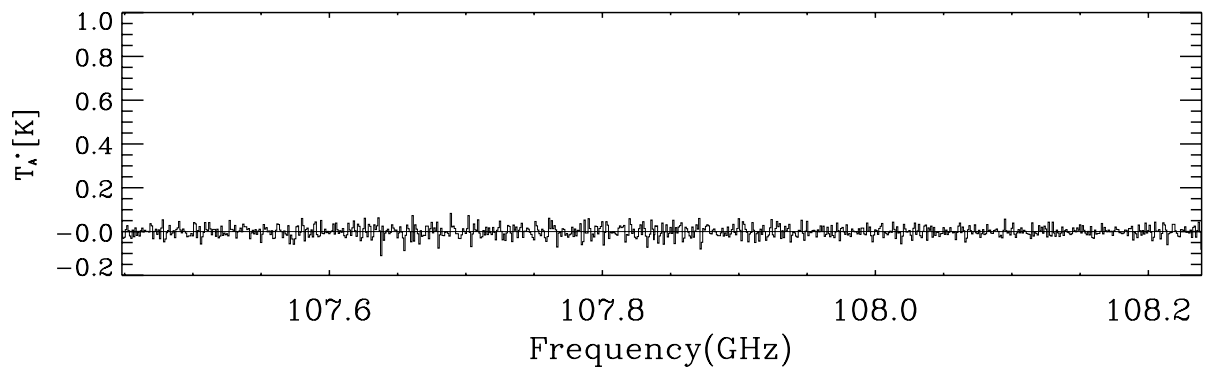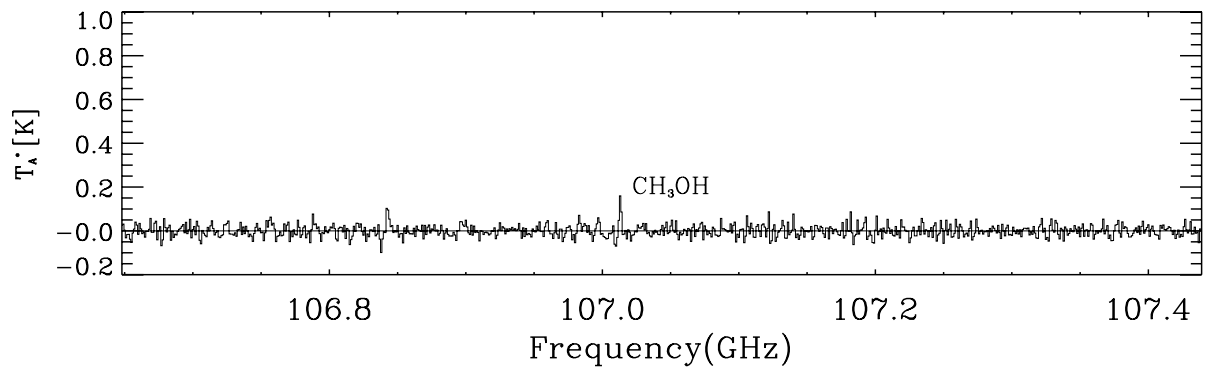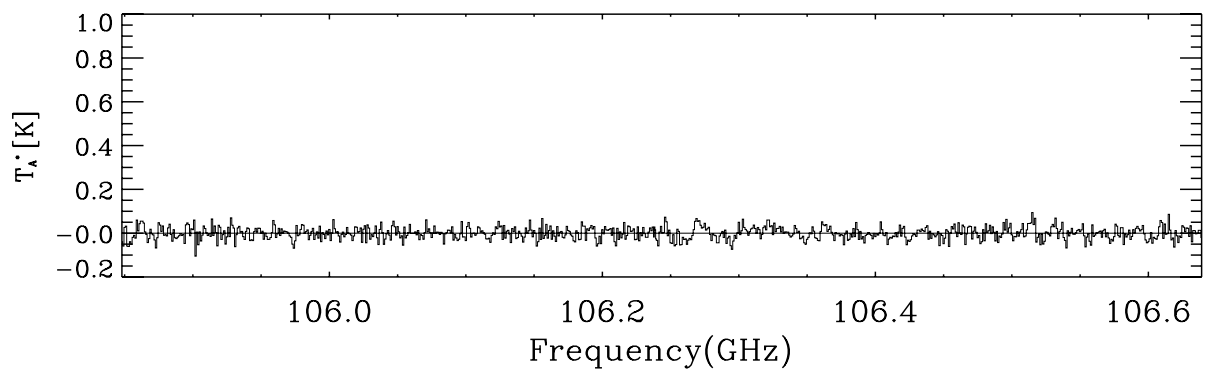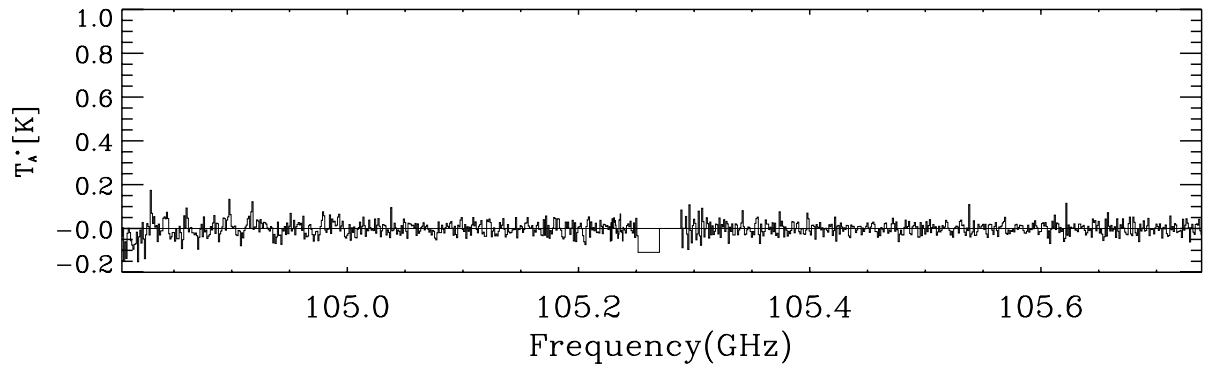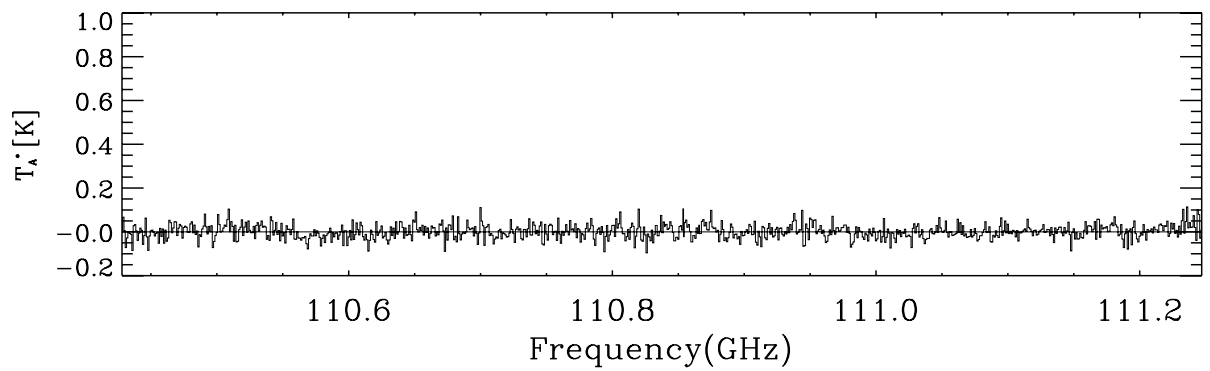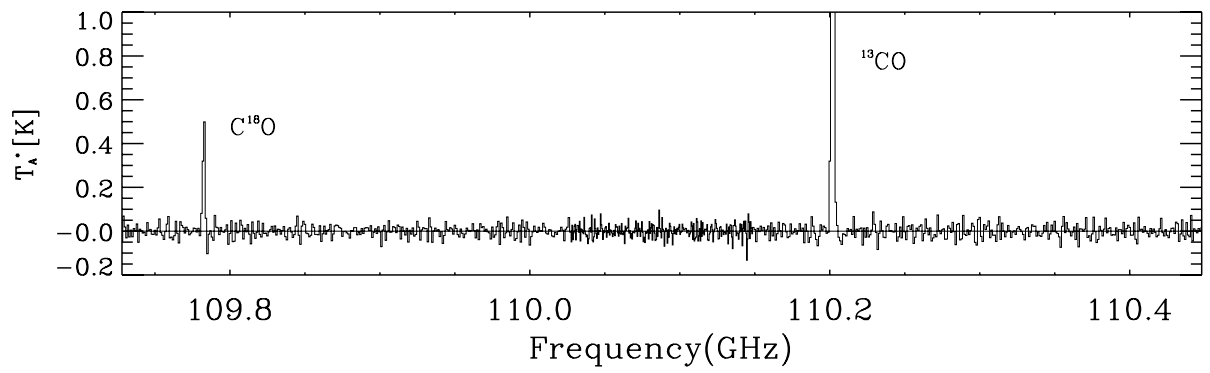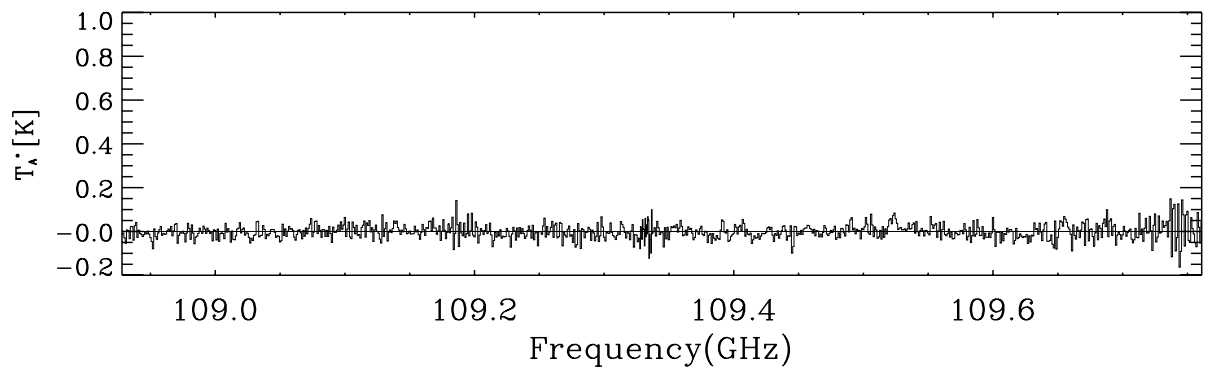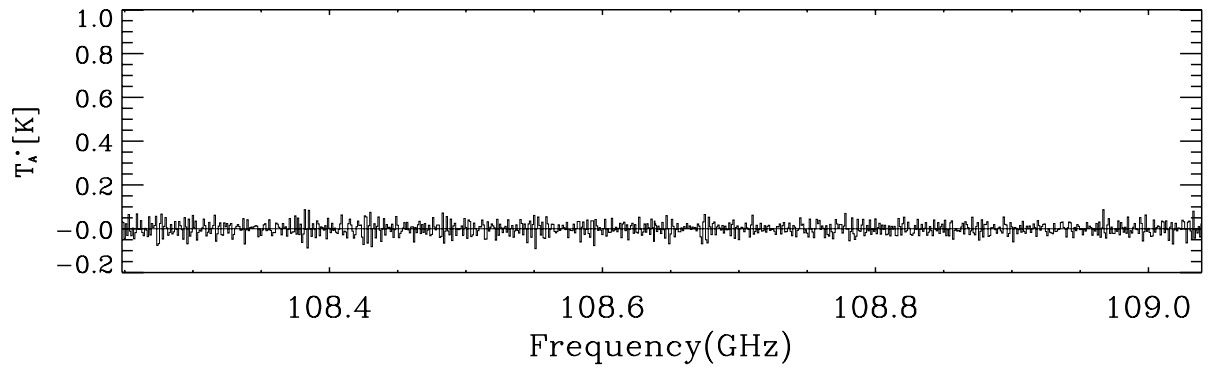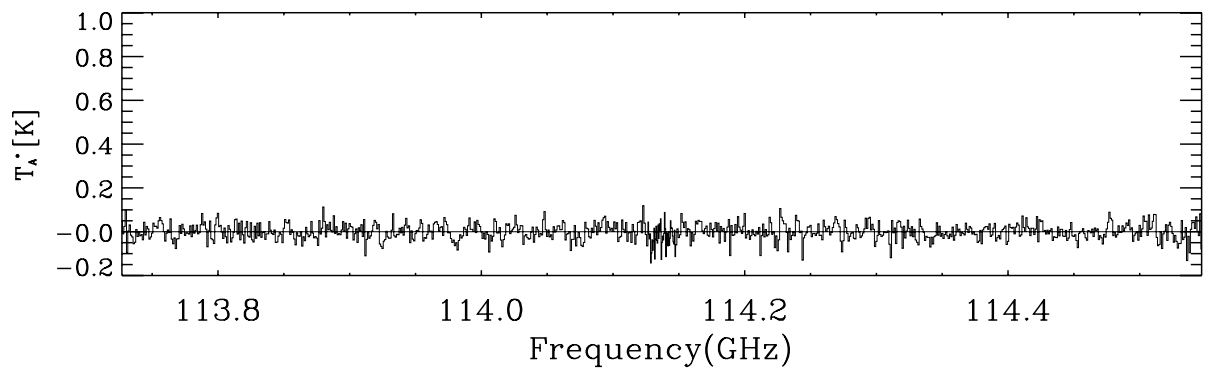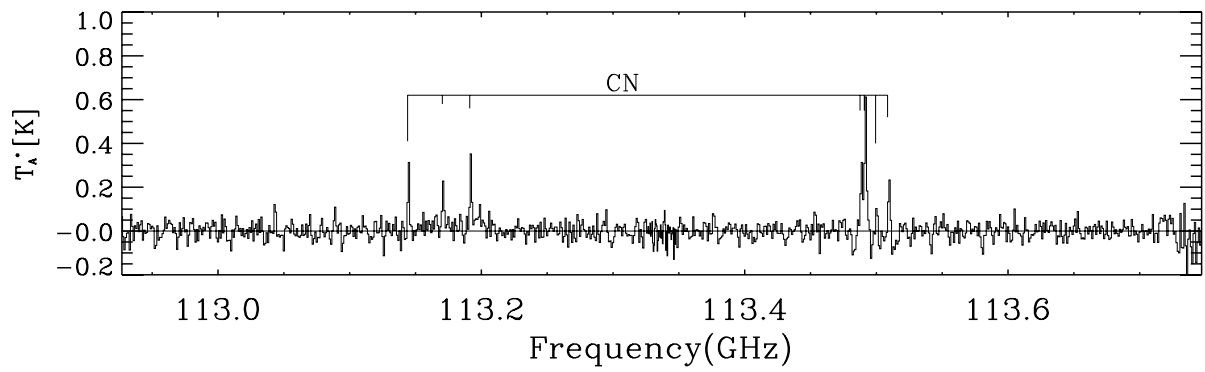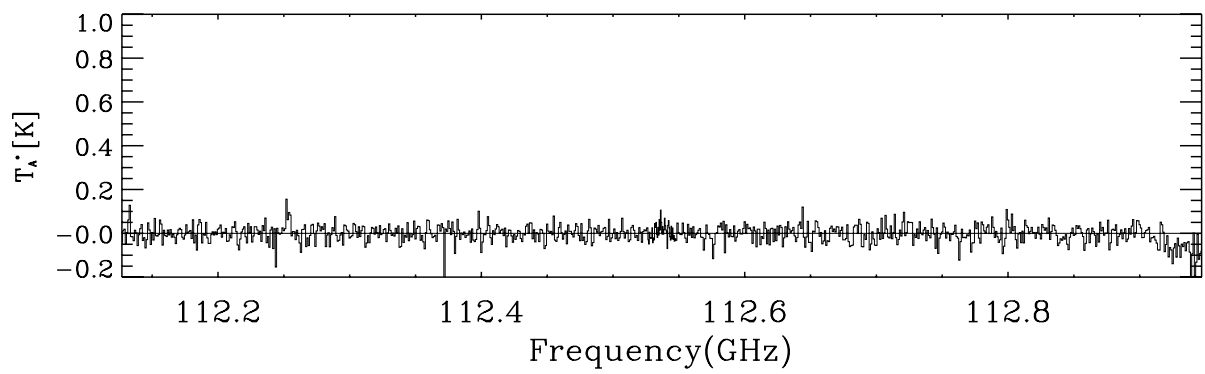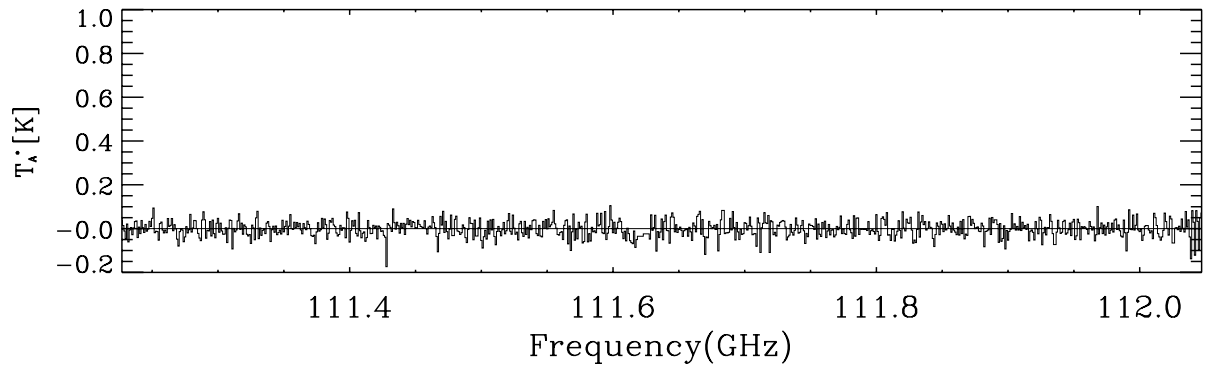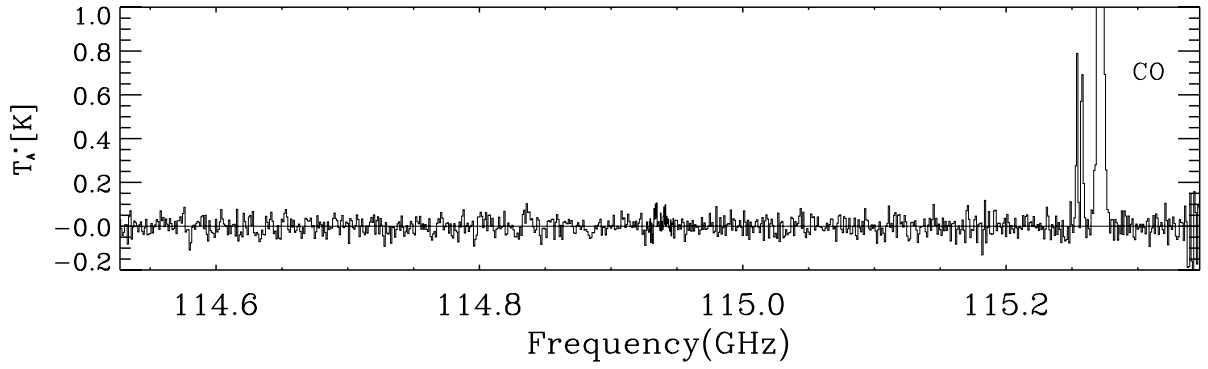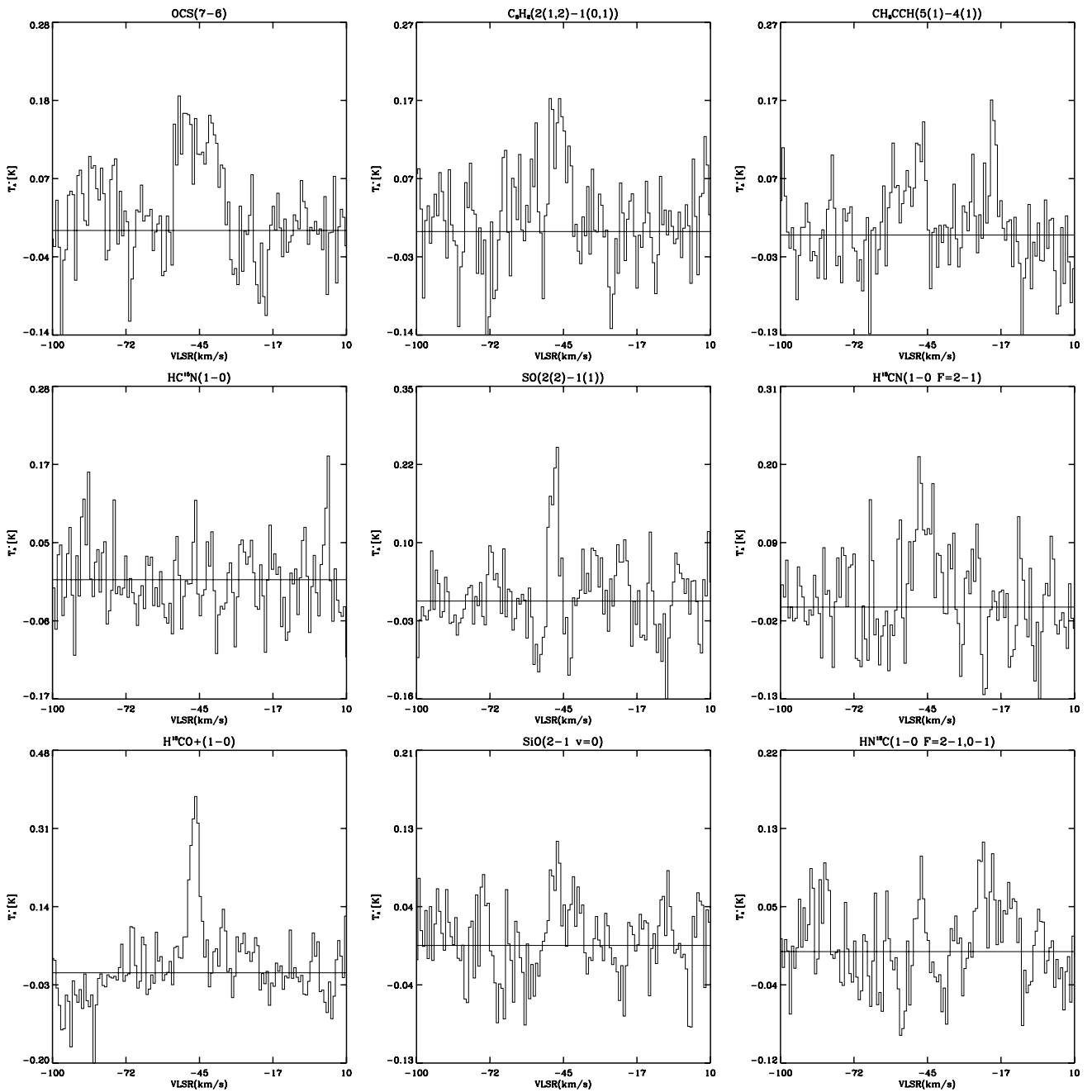
FIG. 1.—Continued

FIG. 2.—Spectra of individual lines in W3(OH) observed with 250 kHz resolution.

172

F<small>IG</small>. 2.—*Continued*

173

Fig. 2.—*Continued*

174

Fig. 2.—*Continued*

175
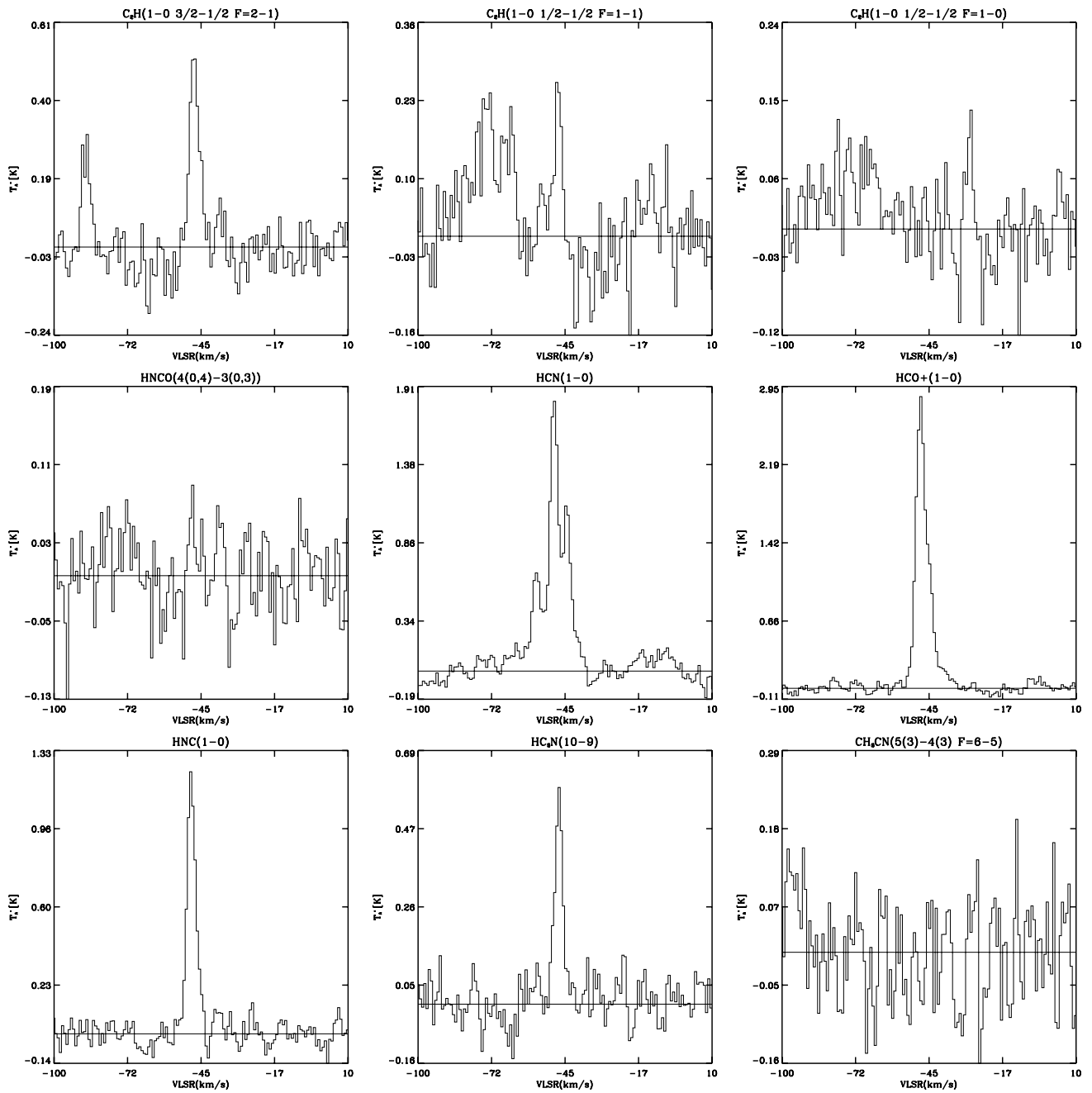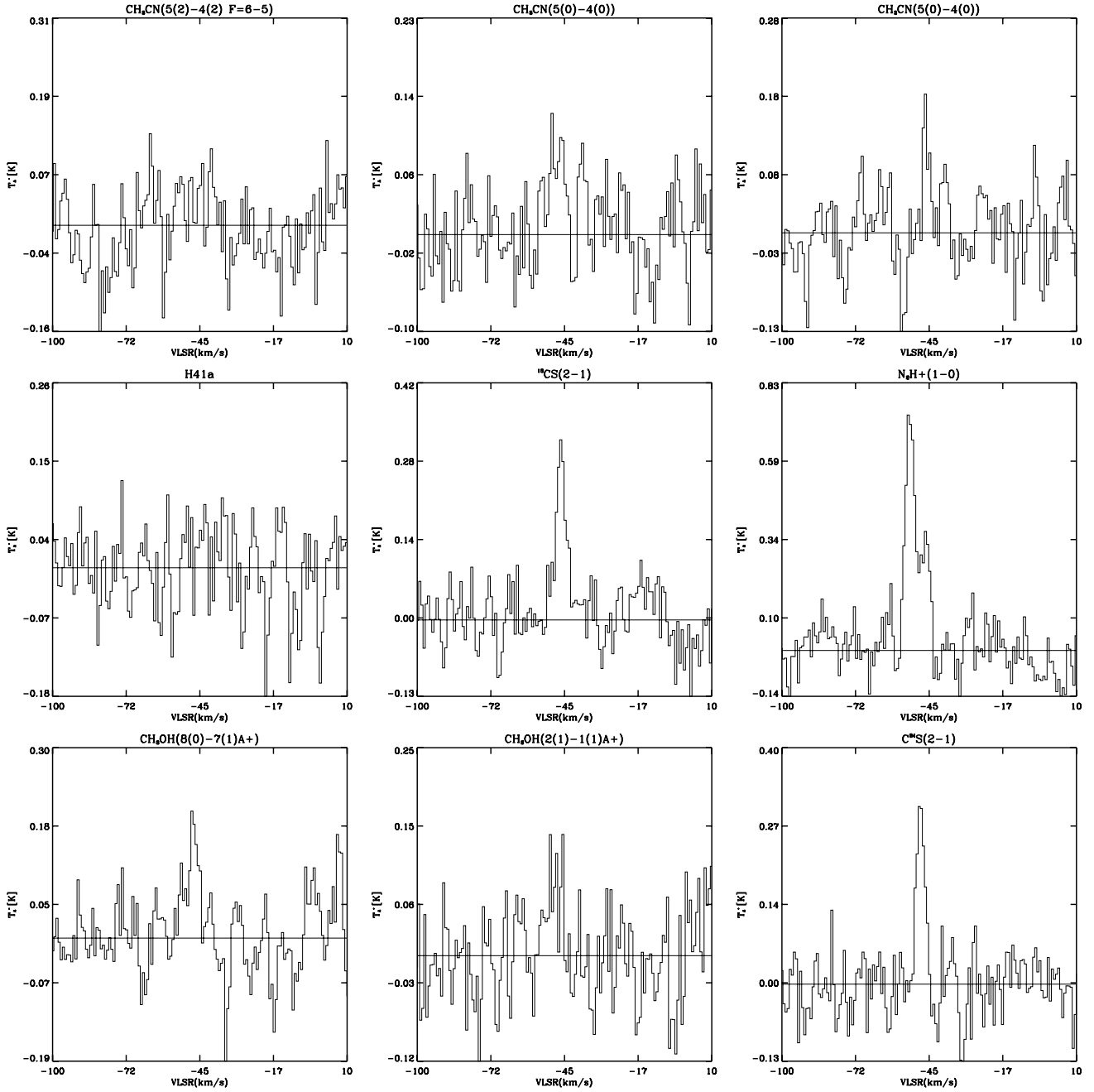
Fig. 2.—*Continued*
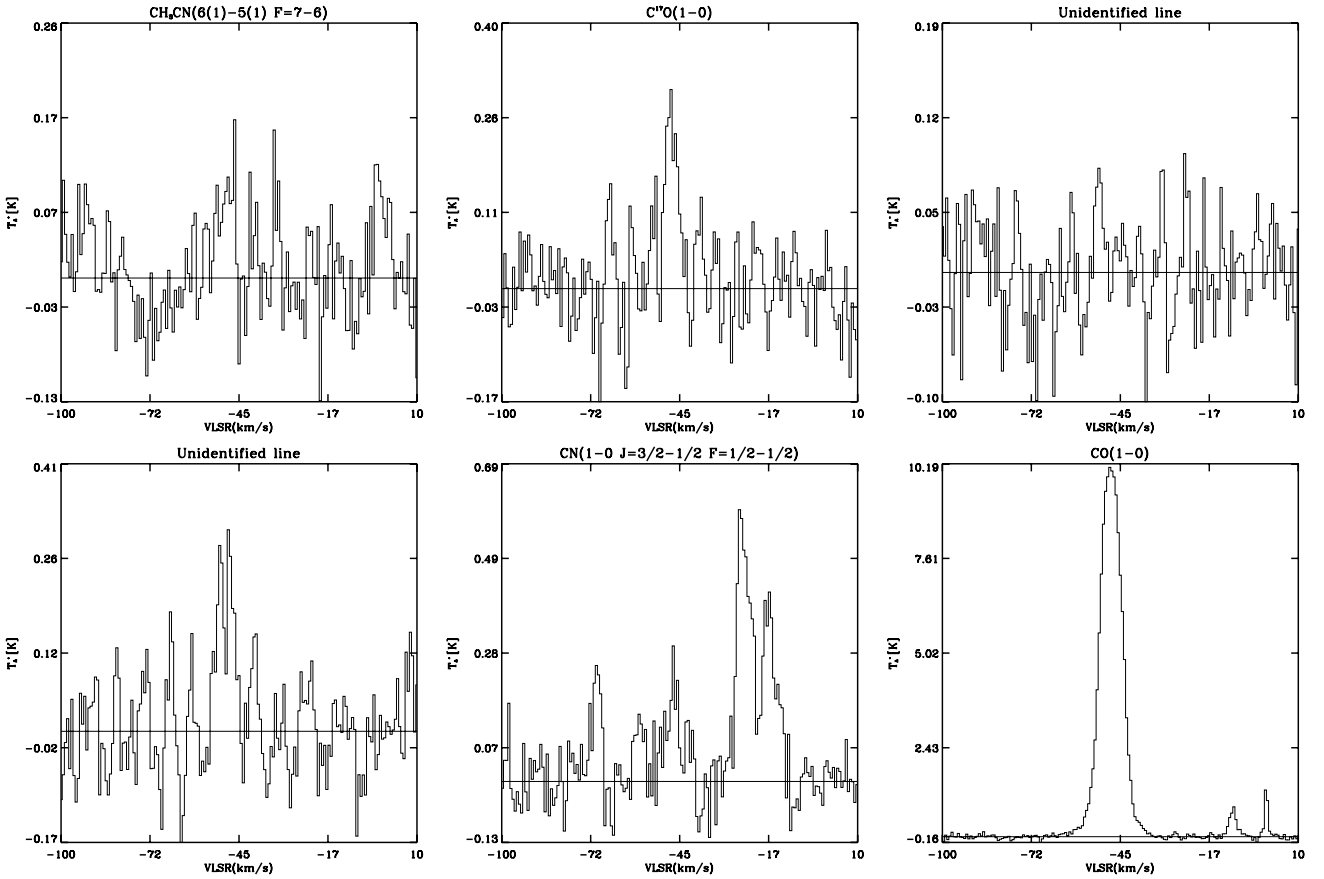
FIG. 2.—*Continued*

A total of 43 transitions including blended lines from 18 species were detected in the 1 MHz observations toward W3(OH), whereas 75 lines from 28 species were detected in the 250 kHz resolution observations (Table 2). As shown in Table 2, most of the lines detected at 250 kHz resolution are weak ($\sim$0.1–0.2 K), except for a few lines such as HC$_3$N (12–11) and H^{13}CO$^+$ (1–0). The H^{13}CO$^+$ (1–0) transition was only observed in 250 kHz resolution; the nondetection of H^{13}CO$^+$ (1–0) in 1 MHz spectrum was due to bad channels in the vicinity of the emission line. Only 20 lines were detected in W3 IRS 5 (Table 2). The detection of H41α recombination line in W3 IRS 5 was interesting, because it was not detected in W3(OH) but was observed in G34.3+ 0.15 (Kim et al. 2000). HNCO [4(0, 4)–3(0, 3)], CH$_3$OH [0(0)– 1($-$1) E], and CH$_3$OH [2(1)–1(1) $A-$] transitions were confirmed from high-resolution observations toward the ultracompact H II region G34.3+0.15 (Table 3).

Though none of the SO$_2$ transitions in the 3 mm wavelength were detected from the 1 MHz spectral resolution surveys of Kim et al. (2000), a number of SO$_2$ transitions were observed from Orion-KL with strong intensities. Therefore, their detections were expected especially in G34.3+0.15, because in the context of chemistry G34.3+0.15 is more like that in Orion-KL. As a result, we confirmed the SO$_2$ [3(1, 3)–2(0, 2)] transition in G34.3+0.15, W3(OH), and W3 IRS 5. However, SO$_2$ [27(3, 25)–26(4, 22)], having an energy level difference of 370 K in temperature, was only detected in G34.3+0.15, just above the noise level (Fig. 4). SO$_2$ [25(3, 23)–24(4, 20)] was not detected.

In order to show the difference in sensitivity between the 1 MHz and 250 kHz spectrometers, we present relative sensitivity curves for the two spectrometers in Figure 6. The sensitivity curves

were obtained from the observations of the SiO ($v = 1, J = 2-1$) line of a point source, χ Cygni, with a short exposure time.

5. INDIVIDUAL MOLECULES

In this section, we present derived abundances of molecules. Since our telescope beam size is large, the derived abundances are affected by the following beam-filling effects. Assuming that antenna response and source brightness distribution are both Gaussian, the beam-filling factor (η_s) can be written as (e.g., Nummelin et al. 1998)

$$\eta_s = \theta^2(\text{source})/[\theta^2(\text{telescope beam}) + \theta^2(\text{source})],$$

where $\theta(\text{source})$ is the source size and $\theta(\text{telescope beam})$ is the beam size of the antenna. Then, the corrected brightness temperature is

$$T_{\text{bc}} = T_{\text{mb}}/\eta_s,$$

where T_{mb} is the main-beam brightness temperature. If a source is smaller than the telescope beam, the derived abundance will be underestimated. The source sizes are, however, often not known. Therefore, we caution that our derived abundances are likely to be underestimated for small sources. Distribution of SiO molecules, for instance, is known to be compact, whereas that of CO is mostly extended. The derived column abundances of SiO listed in Table 4, therefore, are underestimated. On the other hand, the CO distribution is expected to be larger than the telescope beam size. In this paper, we consider the sidelobes of the beam by taking forward spillovers and scattering factors in the column densities.
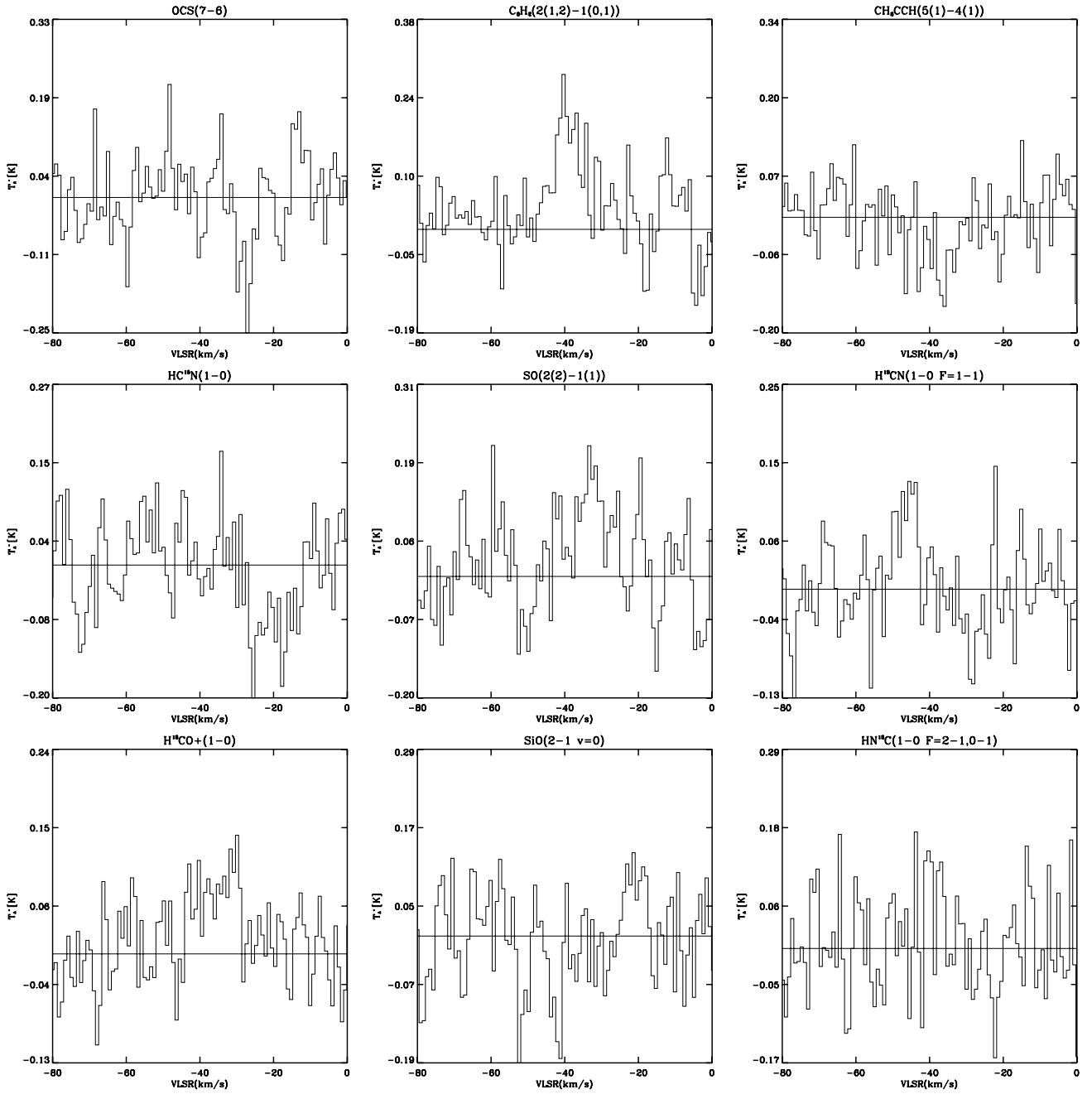
Fig. 3.—Spectra of lines in W3 IRS 5 observed with 250 kHz resolution.

F<small>IG</small>. 3.—*Continued*

179

F{IG}. 3.—*Continued*

180

CS(2−1)

SO(3(2)−2(1))

HC^{15}N(11−10)

H${}_2$CS(3(1,3)−2(1,2))

CH${}_3$CCH(6(1)−5(1))

H${}_2$CS(3(0,3)−2(0,2))

SO${}_2$(3(1,3)−2(0,2))

H${}_2$CS(3(1,2)−2(1,1))

CH${}_3$OH(0(0)−1(−1)E)

T_A^*[K]

VLSR(km/s)

F$_{IG}$. 3.—*Continued*

181
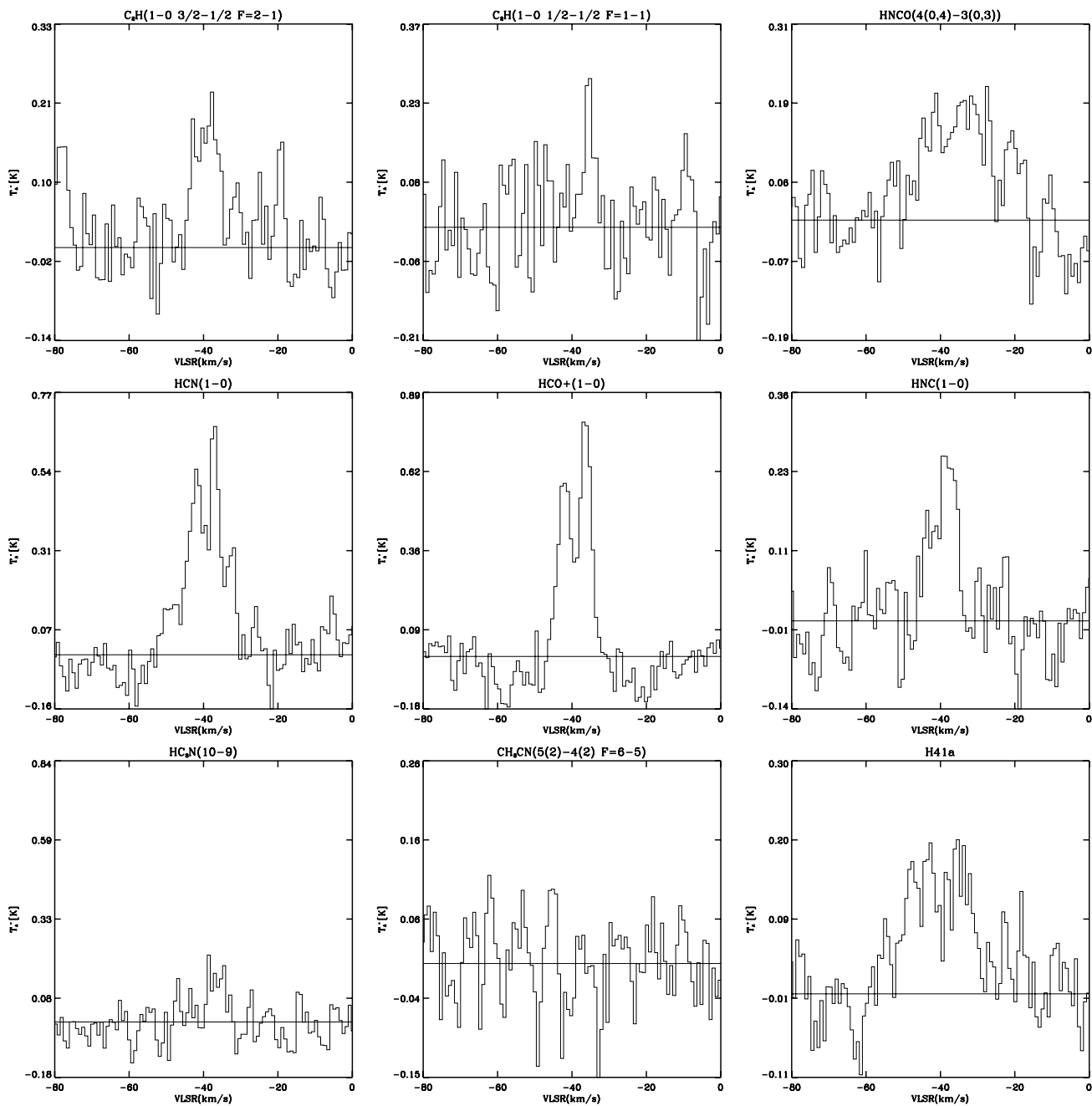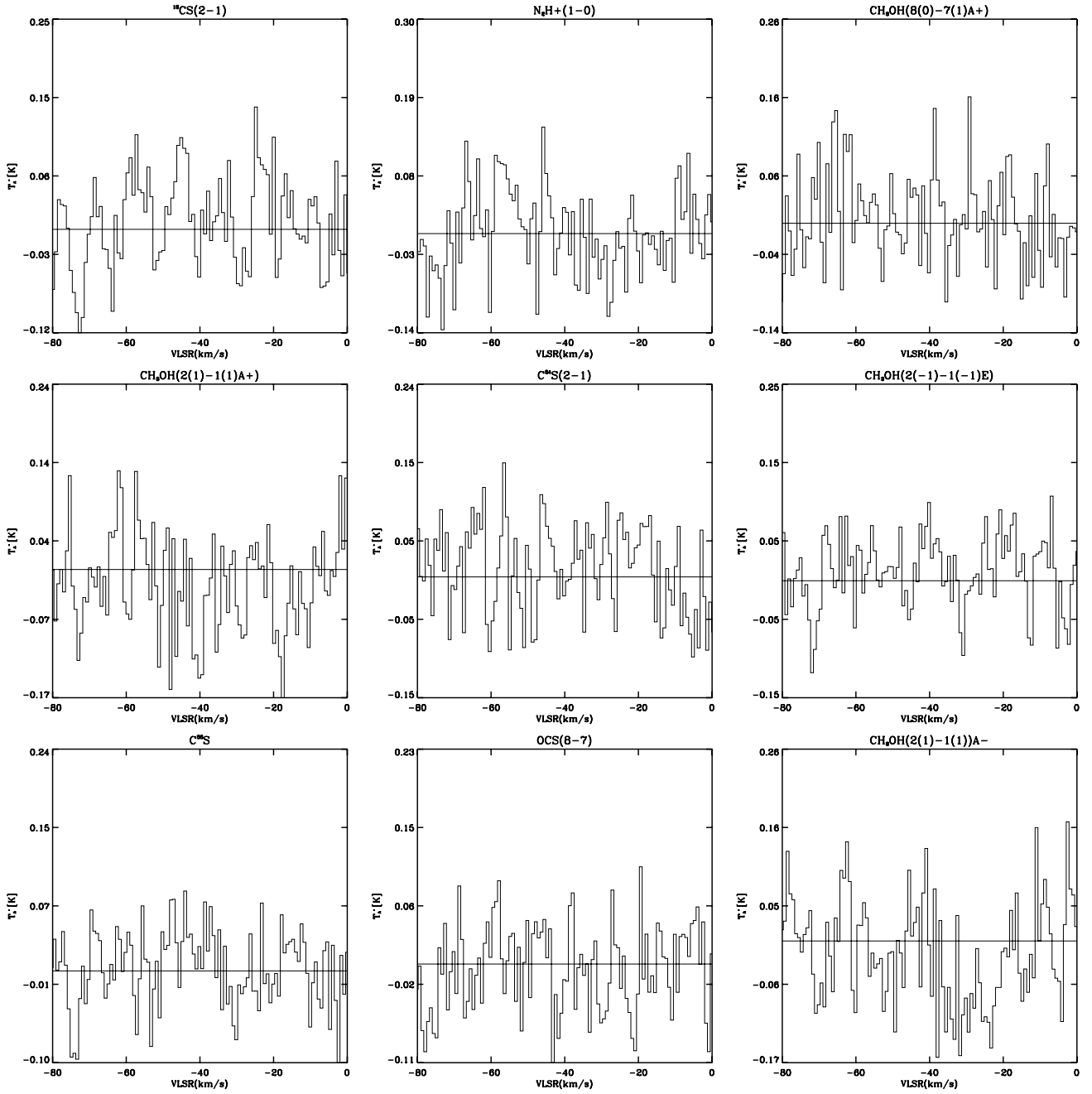
Fig. 3.—*Continued*

Fig. 3.—*Continued*

Therefore, the effects of beam filling would not be very significant for large sources. Comparisons of our results with those of other authors, who used smaller beams, should also be done with caution.

5.1. *Ionized Species*—HCO^+ *and* N_2H^+

The molecule HCO^+ is important because it is formed at a more primitive level of chemistry than species like H_2CO and NH_3, and the role of ion-molecule chemistry can be tested directly (Turner 1995). HCO^+ is closely linked with CO in both the diffuse- and dense-cloud regimes; hence, it provides a probe of ion-molecule chemistry, because the abu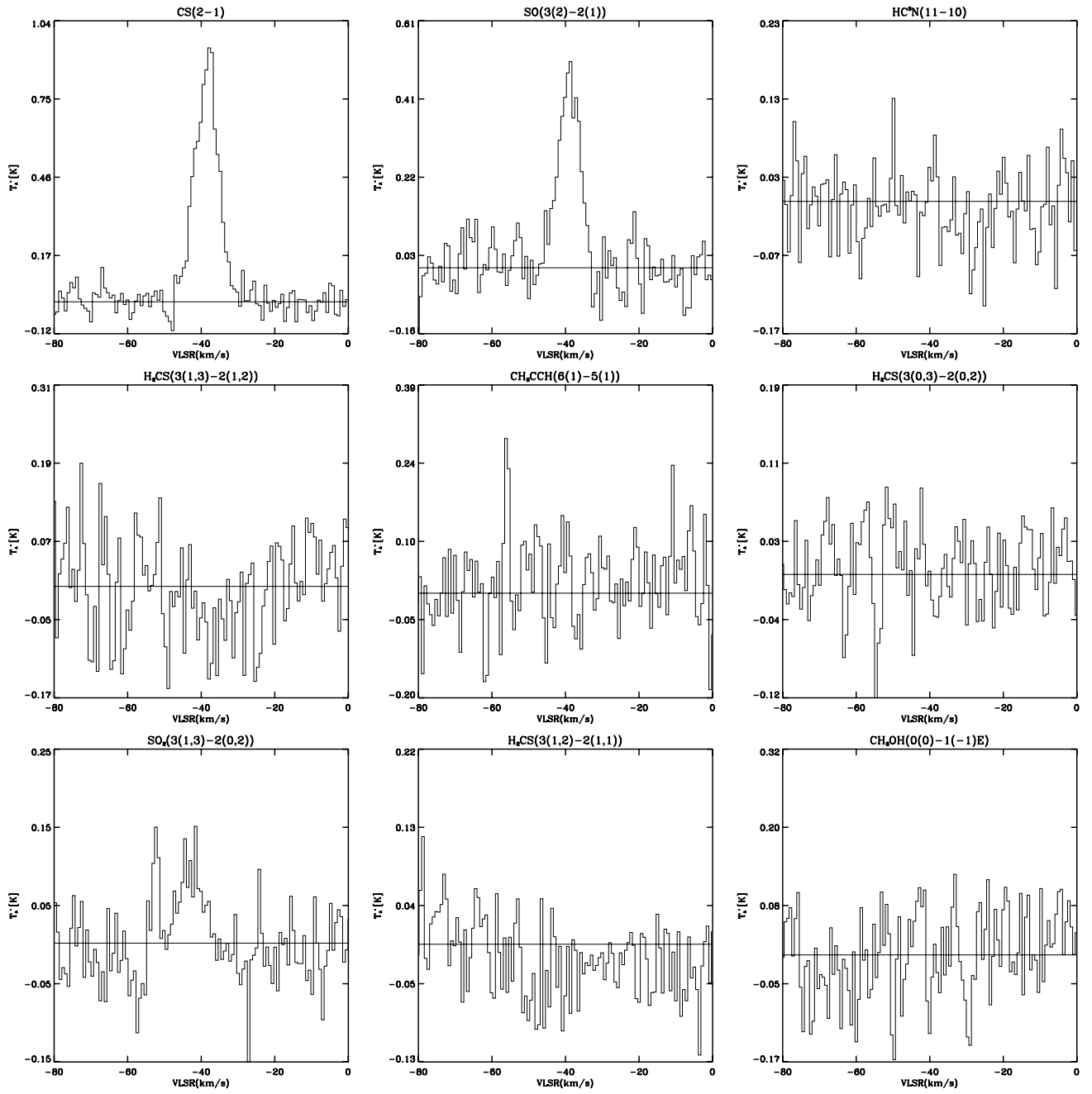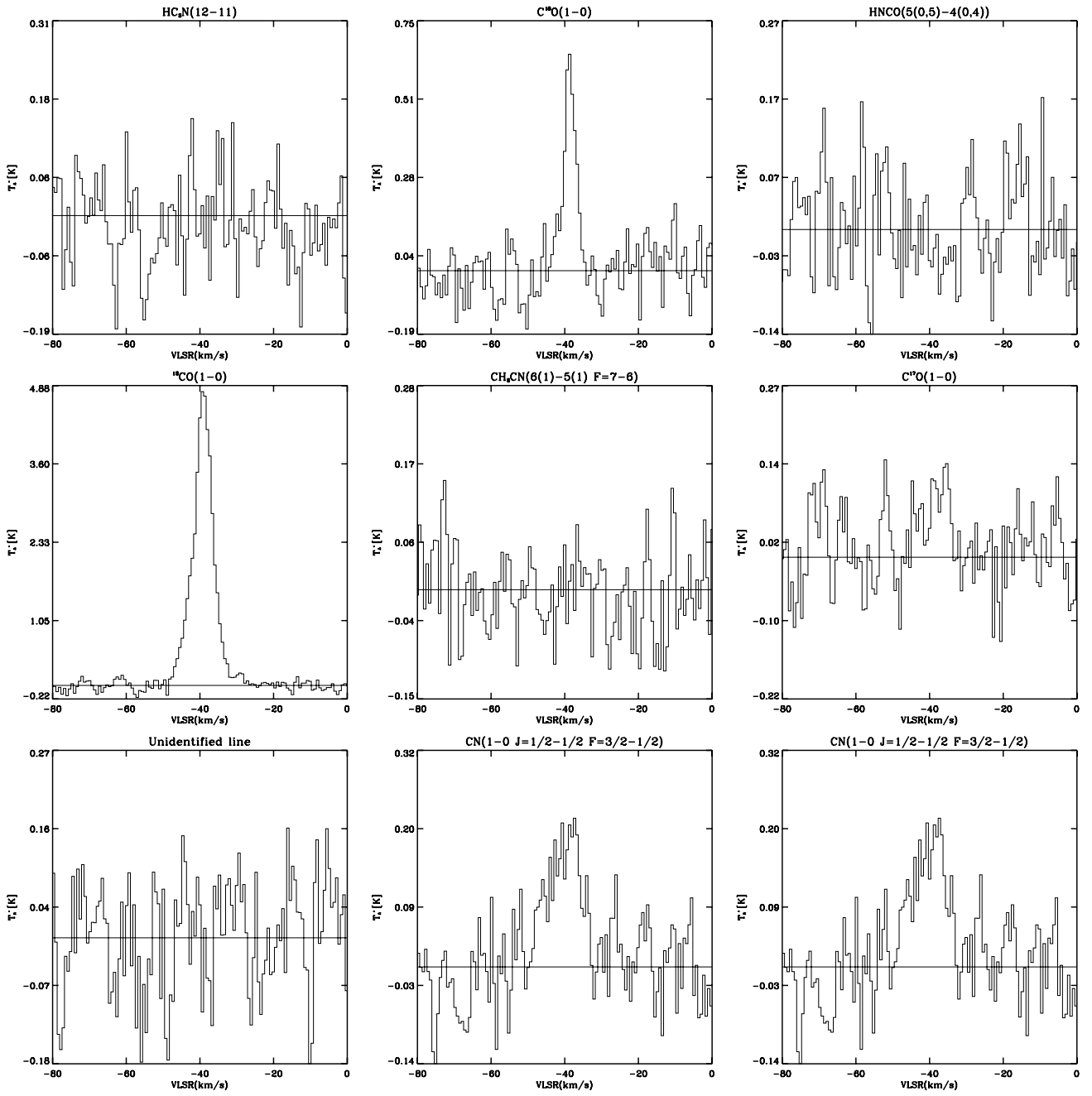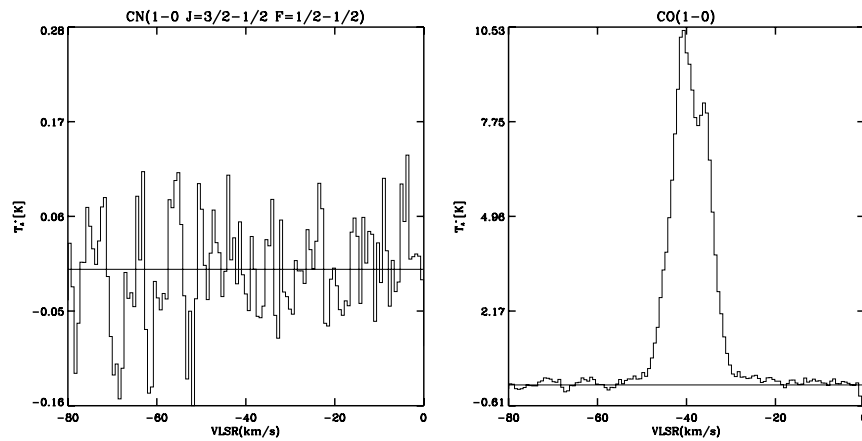ndance of CO and its isotopomers are particularly well understood as a result of the models of van Dishoeck & Blake (1986, 1988).

In some sources containing low-mass young stellar objects, HCO^+ appears to be influenced by stellar outflows, and N_2H^+, on the other hand, seems to trace preferentially the quiescent outer envelope (Bachiller 1996a, 1996b; Mardones et al 1997; van Dishoeck & Blake 1998). N_2H^+ is known to be more abundant in the quiescent medium than in shocked regions (Bachiller 1996a, 1996b). In contrast to HCO^+, no line wings are seen in N_2H^+ (Womack et al. 1992). While N_2H^+ is known to be a good tracer of cold clouds, HCO^+ has been widely used to investigate infall motions of prestellar cores (Gregersen et al. 1997). The high abundance of HCO^+ in such active regions can be accounted by desorption process of ice mantle components, H_2O and CO, by shock heating (Rawlings et al. 2000).

In this survey, we detected several ionized species, such as HCO^+, $H^{13}CO^+$, and N_2H^+, in W3(OH), whereas N_2H^+ was not detected in W3 IRS 5. Column densities for N_2H^+ have been found to be 5×10^{12} cm^{-2} and $\sim 10^{14}$ cm^{-2} in cold and warm clouds, respectively (Womack et al. 1992); but it is apparently absent from hot and shocked gas clouds (Womack et al. 1992; Bachiller 1996a, 1996b). Therefore, it is likely that either dispersion by shocks generated by outflows from the embedded source (Womack et al. 1992; Bachiller 1996a, 1996b) or depletion of the species on the dust (Bergin et al. 2002) is responsible for the non-detection of N_2H^+ in our observations toward W3 IRS 5.

Self-absorption in the line of HCO^+ was seen in G34.3+0.15 and W3 IRS 5, however, no self-absorption was found in W3(OH) (Fig. 7). The low column density of HCO^+ in G34.3+0.15, therefore, might be influenced by absorption in the surrounding cold envelope. The spectral feature of HCO^+ is found to be redshifted by 3 km s^{-1} from the central velocity (58 km s^{-1}), and an absorption feature was seen at ~ 61 km s^{-1}. While the strong HCO^+ peak in the G34.3+0.15 spectrum appears to be redshifted, it is blueshifted in W3 IRS 5. The HCO^+ spectral feature of W3 IRS 5 seems to be incompatible with the nominal spectral shapes of the infalling/collapsing models (Zhou et al. 1993). An explanation may be because HCO^+ in W3 IRS 5 might have been affected by the outflows.

Helmich & van Dishoeck (1997) obtained an HCO^+ column density of $N = 2 \times 10^{14}$ cm^{-2} toward $W3(H_2O)$. [Note that W3(OH) and $W3(H_2O)$ are separated by $6''$.] The result is very similar to the value of $N = 1.23 \times 10^{14}$ cm^{-2} found from our observations in the direction of W3(OH), which would include $W3(H_2O)$ in the same beam.

On the other hand, the abundance ratio of HCO^+ relative to N_2H^+ was found to be ~ 22 in W3(OH) (Table 4). The excitation temperature (~ 5 K) adopted in our calculation is a reasonable value for heavy molecules, and therefore the derived N_2H^+ column density would not differ from the realistic density. In addition, the line intensity (0.6 K) of N_2H^+ observed in W3(OH) indicates that it is not optically thick. A high ratio of HCO^+/N_2H^+ is predicted by the reaction $N_2H^+ + CO \rightarrow HCO^+ + N_2$, which involves destruction of N_2H^+ and the production of HCO^+ (Snyder & Watson 1977).

5.2. *Sulfur-bearing Species*—OCS, SO, CS, and SO_2

The abundances of sulfur-bearing species in the star-forming regions have been found to be significantly different from those in dark or quiescent regions (Charnley 1997). Sulfur-bearing species are known to form efficiently from reactions involving parent H_2S. The widely accepted theory of H_2S formation is that sulfur freezes out onto grains during the collapsing phase, and it remains on the grains in the form of H_2S until it is evaporated by heating in a hot core (Charnley 1997; Hatchell et al. 1998). CS is often used as a tracer of dense gas region, and it results from reactions of S^+ and S with CH and C_2 (van Dishoeck & Blake 1998).

We observed several optically thin, isotopic variants of CS in W3(OH) and G34.3+0.15, and we derived column densities and optical depths using these optically thin lines (Table 4). CS column density ratios between W3(OH) and G34.3+0.15, derived from isotopic variants, are similar to within a factor of 2. On the other hand, CS column densities of W3(OH), derived from its isotopic variants, appear to be similar.

We have carried out large velocity gradient (LVG) model calculations to construct models for comparison with observations. Comparisons were made for excitation temperatures, optical depths, and the observed intensities of CS (2–1) for W3(OH) and G34.3+0.15. In the models, we examined H_2
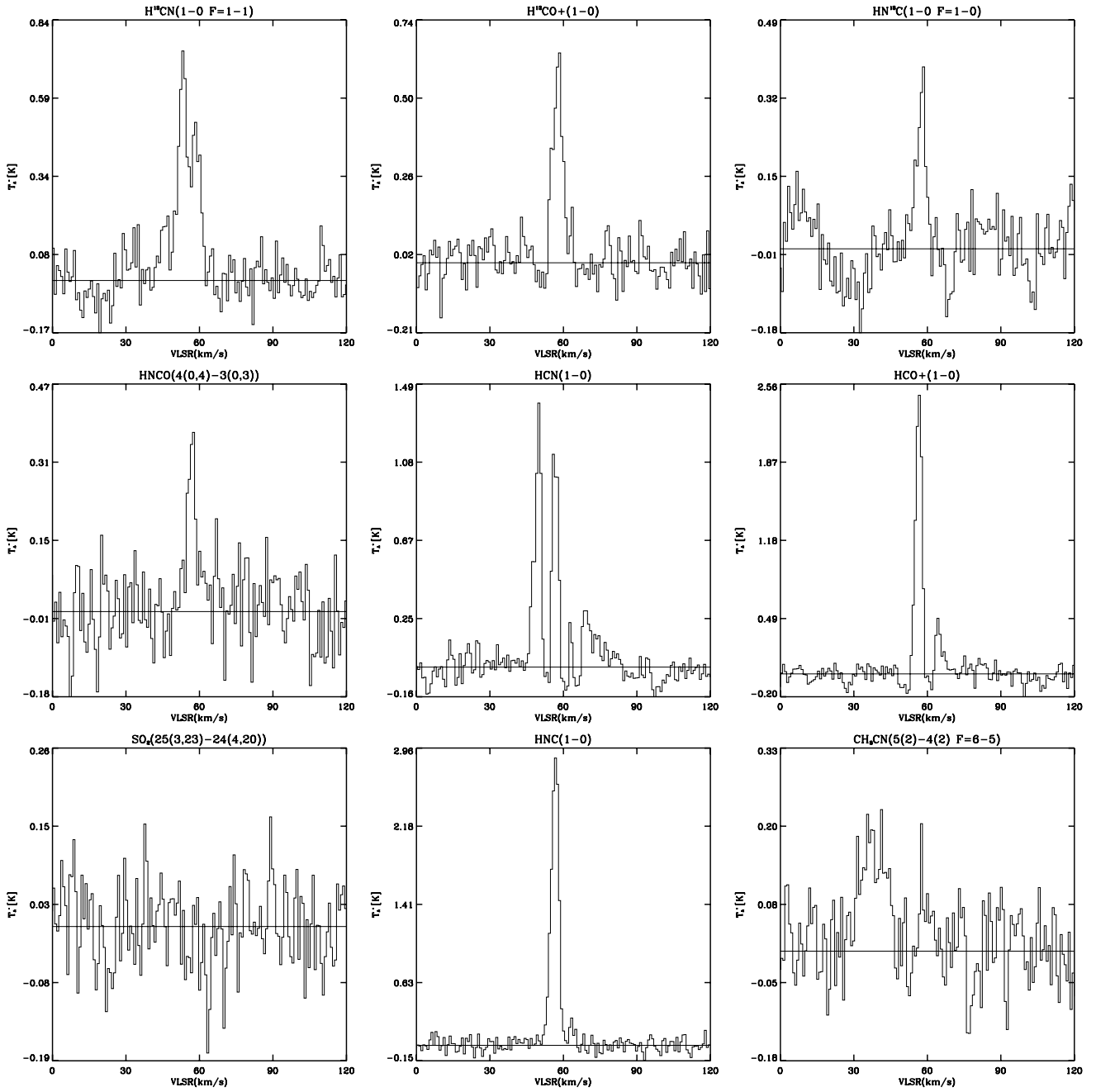
FIG. 4.—Spectra of lines in the ultracompact H II region G34.3+0.15 observed with 250 kHz resolution.

Fig. 4.—*Continued*

185
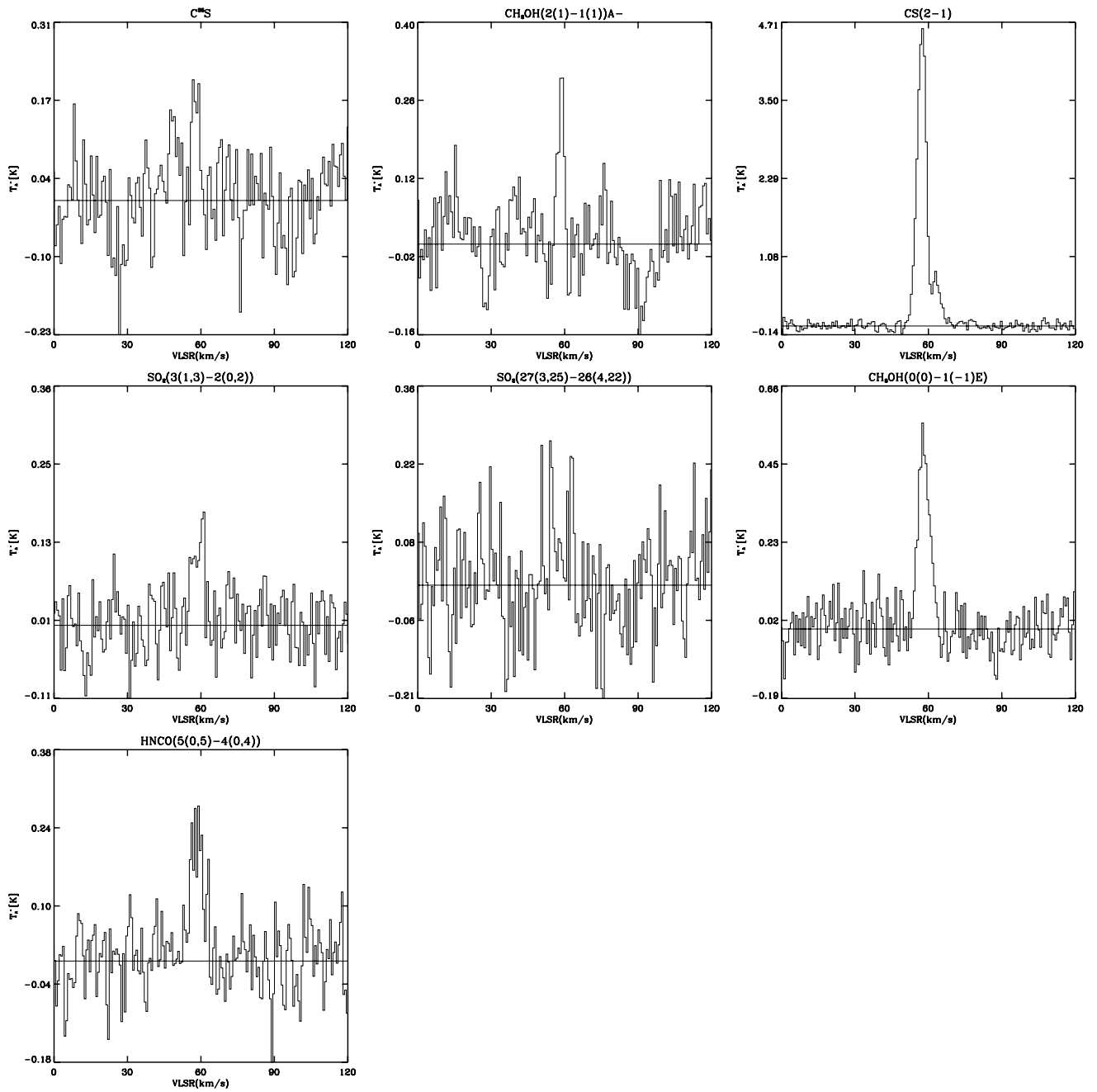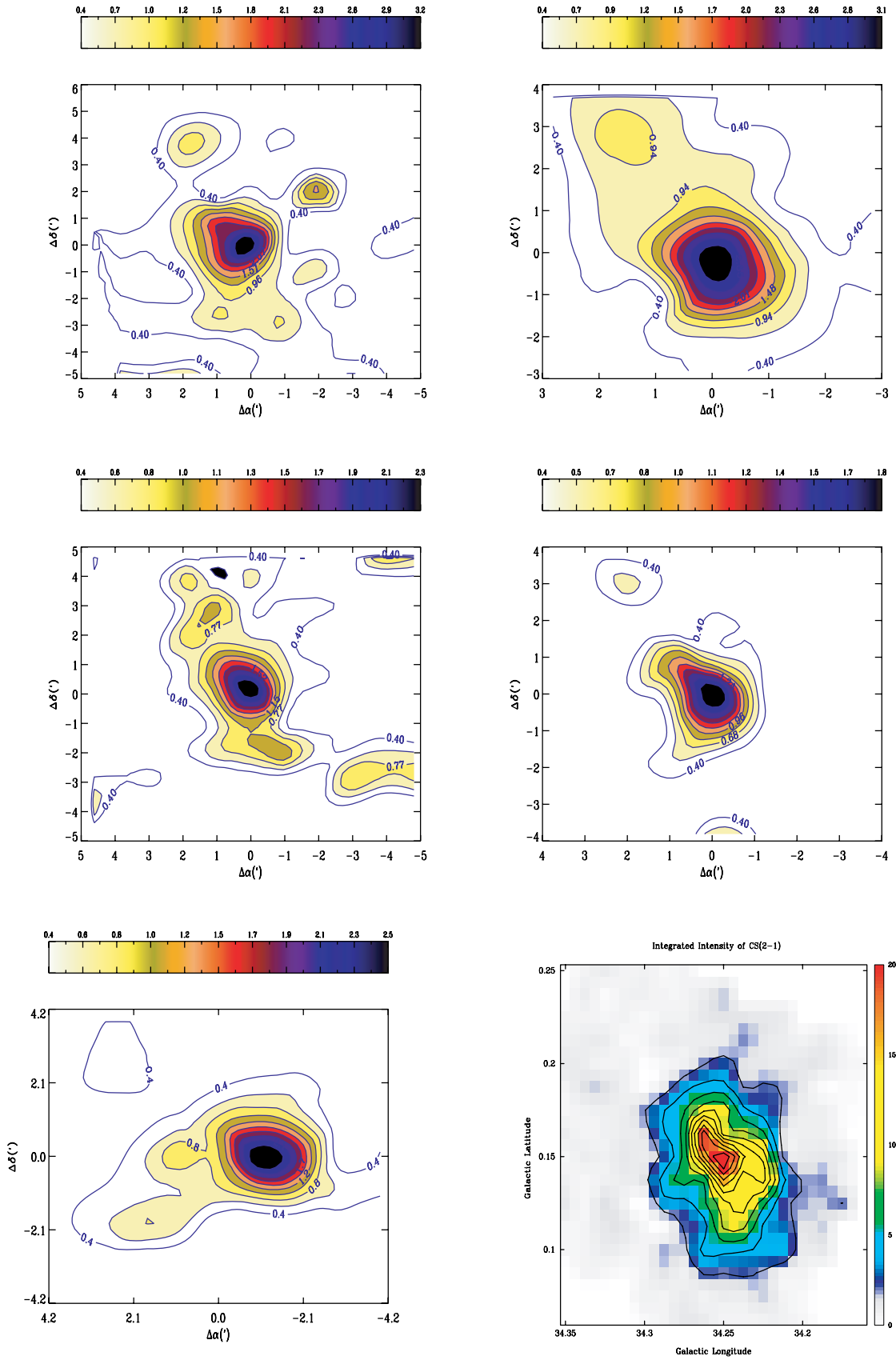
Fig. 5.—Map of CS (2−1) map (*upper left panel*), HCO⁺ (1−0) (*upper right panel*), HCN (1−0) (*middle left panel*), and HNC (1−0) (*middle right panel*) taken toward the strong OH-emitting region W3(OH), and CS (2−1) map taken toward W3 IRS 5 (*lower left panel*). Observations were carried out between 2001 November and 2002 February. Contours are drawn for the signals stronger than 0.4 K, with ∼5 σ. While the CS (2−1) map (*lower right*) of G34.3+0.15 drawn with the data taken from the independent project is an integrated intensity map, other map figures are contoured using the peak of signal taken from this project.

TABLE 2

Observed Transitions in W3(OH) and W3 IRS 5 from a 1 MHz and 250 kHz Resolution Spectrometer

ν(rest) (GHz)	Species	Transition	T_A^* (K)		$\Delta\nu$ (km s^{-1})		$\int T_A^* dv$ (K km s^{-1})		Notes
			W3(OH)	W3 IRS 5	W3(OH)	W3 IRS 5	W3(OH)	W3 IRS 5	
85.1391	OCS	7–6	0.15		7.02		1.11		
85.3389	C$_3$H$_2$	2(1, 2)–1(0, 1)	0.16	0.21	6.88	8.29	1.17	1.91	
			0.15		9.39			1.50	1 MHz
85.4507	CH$_3$CCH	5(2)–4(2)	0.17		2.81		0.50		
85.4557	CH$_3$CCH	5(1)–4(1)	0.14		2.52		0.38		
85.4573	CH$_3$CCH	5(0)–4(0)	0.10		7.79		0.22		
			0.08		11.65		1.01		1 MHz (b)
86.0935	SO	2(2)–1(1)	0.24	0.19	3.54	6.20	0.89	1.22	
86.3388	H^{13}CN	1–0, F = 1–1	0.15	0.12	8.63	6.05	1.35	0.77	
			0.26		15.46		3.55		1 MHz
86.3402		1–0, F = 2–1							
86.3423		1–0, F = 0–1							
86.7543	H^{13}CO$^+$	1–0	0.36	0.10	4.51	8.60	1.74	0.91	
86.8470	SiO	2–1, $v = 0$	0.09		5.12		0.50		
87.0907	HN^{13}C	1–0, F = 0–1	0.09		2.81		0.27		
87.0909	HN^{13}C	1–0, F = 1–1							
87.3169	C$_2$H	1–0 3/2–1/2, F = 2–1	0.52	0.19	4.29	8.35	2.34	1.66	
			0.40		4.13		1.63		1 MHz
87.3286	C$_2$H	1–0 3/2–1/2, F = 1–0	0.28	0.15	3.65	5.21	1.08	0.82	
			0.33		3.12		1.09		1 MHz
87.4020	C$_2$H	1–0 1/2–1/2, F = 1–1	0.26	0.26	3.17	3.10	0.86	0.85	
			0.25		6.28		1.71		1 MHz
87.4072	C$_2$H	1–0 1/2–1/2, F = 0–1	0.19		4.20		0.84		
87.9252	HNCO	4(0, 4)–3(0, 3)	0.09		2.04	0.17	0.19	7.69	
88.6304	HCN	1–0, F = 1–1	1.12	0.33	3.24	3.01	3.84	1.05	
88.6318	HCN	1–0, F = 2–1	1.82	0.64	3.96	3.72	7.65	2.52	
88.6339	HCN	1–0, F = 0–1	0.66	0.55	4.37	4.02	3.05	2.35	
			1.60		11.37		18.82		1 MHz (b)
89.1885	HCO$^+$	1–0	2.58	0.61	5.35	9.38	14.62	6.08	
			1.93		7.25		14.85		1 MHz
90.6635	HCN	1–0, F = 0–1	1.20	0.24	3.95	7.85	5.00	2.00	
90.6636	HCN	1–0, F = 2–1							
90.6637	HCN	1–0, F = 1–1							
			1.00		4.55		6.09		1 MHz
90.9790	HC$_3$N	10–9	0.55	0.17	3.65	5.13	2.14	0.90	
			0.35		4.87		1.86		1 MHz
91.9801	CH$_3$CN	5(2)–4(2)	0.06		3.73		0.24		
91.9853	CH$_3$CN	5(1)–4(1)	0.09		2.69		0.26		
91.9871	CH$_3$CN	5(0)–4(0)	0.16		2.70		0.46		
92.0344	H41α	42–41		0.15		21.16		3.43	
92.4943	^{13}CS	2–1	0.28		4.83		1.45		
93.1716	N$_2$H$^+$	1–0 F1 = 1–1, F = 0–1	0.60		7.03		4.46		
93.1719	N$_2$H$^+$	1–0 F1 = 1–1, F = 2–2							
93.1721	N$_2$H$^+$	1–0 F1 = 1–1, F = 1–0							
93.1735	N$_2$H$^+$	1–0 F1 = 2–1, F = 2–1							
93.1738	N$_2$H$^+$	1–0 F1 = 2–1, F = 3–2							
93.1740	N$_2$H$^+$	1–0 F1 = 2–1, F = 1–1							
			0.63		9.79		6.54		1 MHz
95.1694	CH$_3$OH	8(0)–7(1) $A+$	0.16		5.58		0.95		
95.9143	CH$_3$OH	2(1)–1(1) $A+$	0.10		4.05		0.43		
96.4130	C^{34}S	2–1	0.32		3.61		1.20		
			0.45		5.99		2.84		1 MHz
96.7394	CH$_3$OH	2(−1)–1(−1) E	0.43		3.77		1.73		
96.7414	CH$_3$OH	2(0)–1(0) $A+$	0.49		4.86		2.51		
96.7446	CH$_3$OH	2(0)–1(0) E	0.17		4.01		0.72		
			0.34		10.40		3.76		1 MHz (b)
96.7555	CH$_3$OH	2(1)–1(1) E	0.13		3.96		0.55		
			0.13		4.84		0.68		1 MHz
97.1721	C^{33}S	2–1	0.14		3.46		0.53		
97.3012	OCS	8–7	0.08		2.62		0.23		
97.9810	CS	2–1	2.43	0.87	4.50	7.47	11.60	6.92	
			2.23		5.91		13.99		1 MHz
99.2999	SO	3(2)–2(1)	0.92	0.48	5.84	6.70	5.72	3.39	

187

TABLE 2—*Continued*

ν(rest) (GHz)	Species	Transition	T_A^* (K) W3(OH)	T_A^* (K) W3 IRS 5	$\Delta\nu$ (km s^{-1}) W3(OH)	$\Delta\nu$ (km s^{-1}) W3 IRS 5	$\int T_A^* \, dv$ (K km s^{-1}) W3(OH)	$\int T_A^* \, dv$ (K km s^{-1}) W3 IRS 5	Notes
100.0764............	HC$_3$N	11–10	0.52		3.20		1.75		
			0.33		5.34		1.88		1 MHz
101.4778............	H$_2$CS	3(1, 3)–2(1, 2)	0.20		2.49		0.53		
102.5401............	CH$_3$CCH	6(2)–5(2)	0.16		4.20		0.53		
102.5460............	CH$_3$CCH	6(1)–5(1)	0.18		1.83		0.35		
102.5480............	CH$_3$CCH	6(0)–5(0)	0.21		3.01		0.66		
103.0404............	H$_2$CS	3(0, 3)–2(0, 2)	0.21		3.82		0.86		
104.0294............	SO$_2$	3(1, 3)–2(0, 2)	0.10	0.11	4.24	7.22	0.45	0.81	
104.6170............	H$_2$CS	3(1, 2)–2(1, 1)	0.26		4.36		1.18		
107.0139............	CH$_3$OH	3(1)–4(0) $A+$	0.17		4.62		0.82		1 MHz
108.8939............	CH$_3$OH	0(0)–1(−1) E	0.19		3.29		0.65		
109.1736............	HC$_3$N	12–11	0.45		3.45		1.66		
109.7822............	C^{18}O	1–0	0.44	0.61	4.25	3.81	1.96	2.45	
			0.56		4.24		2.50		1 MHz
110.2014............	^{13}CO	1–0	4.51	4.50	4.48	6.21	21.39	29.65	
			4.69		5.09		25.30		1 MHz
110.3650............	CH$_3$CN	6(3)–5(3)	0.10		4.75		0.52		
110.3761............	CH$_3$CN	6(2)–5(2)	0.11		1.97		0.24		
110.3814............	CH$_3$CN	6(1)–5(1)	0.10		6.17		0.62		(b)
110.3835............	CH$_3$CN	6(0)–5(0)							
112.3588............	C^{17}O	1–0, $F = 3/2$–5/2	0.28	0.13	4.33	5.34	1.29	0.72	
112.3590............	C^{17}O	1–0, $F = 7/2$–5/2							
112.3600............	C^{17}O	1–0, $F = 5/2$–5/2							
113.1442............	CN	1–0, $J = 1/2$–1/2, $F = 1/2$–3/2	0.28	0.19	2.05	5.40	0.62	1.07	
			0.34		3.41		1.25		1 MHz
113.1705............		1–0, $J = 1/2$–1/2, $F = 3/2$–1/2	0.23		4.66		1.11		1 MHz
113.1913............		1–0, $J = 1/2$–1/2, $F = 3/2$–3/2	0.35		4.27		1.59		1 MHz
113.4881............		1–0, $J = 3/2$–1/2, $F = 3/2$–1/2	0.37	0.21	4.71	8.16	1.84	1.78	
			0.31		2.82		1.32		1 MHz
113.4910............		1–0, $J = 3/2$–1/2, $F = 5/2$–3/2	0.55		5.34		3.11		
			0.60		5.02		3.19		1 MHz
113.4996............		1–0, $J = 3/2$–1/2, $F = 1/2$–1/2	0.21		4.49		0.98		
			0.10		2.46		0.50		1 MHz
113.5089............		1–0, $J = 3/2$–1/2, $F = 3/2$–3/2	0.25	0.19	2.91	4.80	0.76	0.94	
			0.25		4.15		1.12		1 MHz (b)
115.2712............	CO	1–0	10.49	9.91	7.51	9.73	83.48	102.16	
			10.85		8.01		92.16		1 MHz

Notes.—Results of detected molecules and their transitions with a 1 MHz and 250 kHz filter bank. Some blended spectral features are marked by "(b)." Several spectra, for example, HCN, show a large difference in line width between 1 MHz and 250 kHz. This is mostly due to blending at 1 MHz spectra, and, hence, fitting errors are expected to be significant, but errors for some molecules, e.g., C^{34}S, are probably due to uncertainties. Line identifications were made after correcting Doppler shift with the velocity of local standard of rest of −46 km s^{-1} for W3(OH) and −39 km s^{-1} for W3 IRS 5.

densities up to 10^6 cm^{-3} and used a kinetic temperature of 20 K, approximately the value of T_R^* found from the CO (1–0) line of W3(OH). Input parameters such as column densities, optical depths, and fractional abundances for the LVG calculations were taken from Table 4. Good agreements in line intensities between models and the observational results were found at hydrogen densities of $n_{H_2} = 3 \times 10^4$ cm^{-3} and $n_{H_2} = 2 \times 10^4$ cm^{-3} for G34.3+0.15 and W3(OH), respectively. As demonstrated in Figure 8, the molecular hydrogen densities, optical depths, and excitation temperatures are determined at the points where observed temperatures (T_{ex}) and theoretical temperatures (T_R^*) meet. Good agreement in the excitation temperatures and optical depths between observations and LVG models were also found at the crossing points where hydrogen densities are $n_{H_2} = (3$–$4) \times 10^4$ cm^{-3}. In Figure 8, the horizontal line is the observed T_R^*, the solid line is the variation of the excitation temperature (T_{ex}), the dotted line is the variation of T_R^*, and the dashed line is the variation of the optical depth.

We detected SO [3(2)–2(1)] in W3(OH), W3 IRS 5 and G34.3+0.15, but the detection of SO [2(1)–1(0)] in W3 IRS 5 was marginal. Lower limits to SO column densities were estimated for the three sources. From SO isotopic variants, ^{34}SO, ^{33}SO, and S^{18}O, N(SO) = 1.3×10^{15} cm^{-2} in W3(H$_2$O) and N(SO) = 5.0×10^{15} cm^{-2} in W3 IRS 5 were derived by Helmich & van Dishoeck (1997). We obtained N(SO) = 1.5×10^{14} cm^{-2} in W3(OH) and 8.7×10^{13} cm^{-2} in W3 IRS 5 from the SO [3(2)–2(1)] transition (Table 4). Contrary to the observations of Helmich & van Dishoeck, which show a high abundance of SO in W3(OH) compared to that in W3 IRS 5, we found the opposite result. Although the lower limit column densities were derived for the three sources, the abundances of SO in W3(OH) and G34.3+0.15 seem to be high, because even the lower limit column densities approach to the column density derived from the optically thick CS line. On the other hand, N(SO) in W3 IRS 5 was found to be greater than N(CS).

The destruction of SO may be contributing to the formation of SO$_2$. The SO$_2$ line intensity of W3 IRS 5 was observed to be

TABLE 3
High-Resolution (250 kHz) Observations of Missing Lines (Kim et al. 2000) and New Observations of Interesting Molecules and Isotopic Variants of G34.3+0.15

ν(obs)[a] (GHz)	T_A^* (K)	$\Delta\nu$ (km s^{-1})	Species	Transition	ν(rest) (GHz)	$\int T_A^* \, dv$ (K km s^{-1})	Notes
86.3397...............	0.54	10.63	H^{13}CN	1–0, $F = 1$–1	86.3388	6.08	
				1–0, $F = 2$–1	86.3402		
				1–0, $F = 0$–1	86.3423		
86.7544...............	0.59	4.85	H^{13}CO$^+$	1–0	86.7543	3.05	
87.0908...............	0.34	4.39	HN^{13}C	1–0, $F = 0$–1	87.0907	1.56	
			HN^{13}C	1–0, $F = 2$–1	87.0909		
			HN^{13}C	1–0, $F = 1$–1	87.0909		
87.9256...............	0.33	4.45	HNCO	4(0, 4)–3(0, 3)	87.9252	1.58	
88.6303...............	0.34	0.88	HCN	1–0, $F = 1$–1	88.6304	0.31	
88.6322...............	1.20	2.80	HCN	1–0, $F = 2$–1	88.6318	3.56	
88.6343...............	1.28	2.30	HCN	1–0, $F = 0$–1	88.6339	4.07	
89.1889...............	2.54	2.99	HCO$^+$	1–0	89.1885	8.03	Self-absorbed
90.6639...............	2.91	3.63	HNC	1–0, $F = 0$–1	90.6635	11.20	(b)
			HNC	1–0	90.6635		
			HNC	1–0, $F = 2$–1	90.6636		
			HNC	1–0, $F = 1$–1	90.6637		
91.9794...............	0.07	5.21	CH$_3$CN	5(2)–4(2) $F = 6$–5	91.9801	0.40	
91.9863...............	0.19	12.12	CH$_3$CN	5(1)–4(1)	91.9853	2.40	(b)
			CH$_3$CN	5(0)–4(0)	91.9871		
97.1721...............	0.21	3.43	C^{33}S	2–1	97.1721	0.76	
97.5826...............	0.31	2.75	CH$_3$OH	2(1)–1(1) $A-$	97.5828	0.89	
97.9812...............	4.58	4.42	CS	2–1	97.9810	21.44	
104.0291..............	0.13	5.93	SO$_2$	3(1, 3)–2(0, 2)	104.0294	0.84	
107.0615..............	0.27	1.36	SO$_2$	27(3, 25)–26(4, 22)	107.0603	0.40	(?)
108.8939..............	0.51	5.46	CH$_3$OH	0(0)–1(−1) E	108.8939	2.93	
109.9056..............	0.23	6.46	HNCO	5(0, 5)–4(0, 4)	109.9057	1.60	

Notes.—Results of detected molecules and their transitions with a 250 kHz filter bank. Some blended spectral features are marked by "(b)". The SO$_2$ 27(3, 25)–26(4, 22) transition marked by "?" is a probable detection (see Fig. 4).
[a] Observed frequencies are obtained after correcting Doppler shift with the velocity of the local standard of rest 58 km s^{-1}.

stronger than that in W3(OH). Helmich & van Dishoeck (1997) attribute it to a more active outflow in W3 IRS 5 than that in W3(OH). The column density of SO$_2$ in the three sources appears to be less abundant than that of SO by a factor of 4–10.

The molecule OCS ($J = 7$–6) would be detected in W3(OH) and G34.3+0.15, but not in W3 IRS 5. On the other hand, two weak lines of OCS were observed in W3 IRS 5 from submillimeter observations by Helmich & van Dishoeck (1997). The

Fig. 6.—Line profiles of a point source, χ Cygni, in the SiO ($v = 1$, $J = 2$–1) line obtained with a 250 kHz and a 1 MHz spectrometer.

OCS (8–7) transition was also seen in W3(OH), but it was not detected in G34.3+0.15, where only 1 MHz observations are available. Since G34.3+0.15 was identified as a site rich in molecules compared with W3(OH) and W3 IRS 5, OCS (8–7) should have been detected if the observations had been carried out deep with the high-resolution spectrometer. Our measurements for OCS (7–6) in W3(OH) were performed twice on different dates, because of its weak signal-to-noise ratio. The weak line intensity of OCS implies a low abundance compared with other S-bearing species detected in our observations. The probable reason is that the local temperature is not high enough for the active formation of OCS via a chemical reaction of CS with atomic oxygen. In addition, according to a reaction process postulated by Prasad & Huntress (1982), the nondetection of H$_2$CS—a precursor of OCS in the reaction scheme—is another possible reason accounting for the nondetection of OCS in W3 IRS 5.

5.3. HCN and HNC

Both HCN and HNC have the same precursors, HCNH$^+$ and H$_2$CN$^+$, and have almost the same dipole moments, from which a similar HNC/HCN abundance ratio is expected. HCN has three hyperfine transitions ($F = 0$–1, $F = 1$–1, and $F = 2$–1), and their intensity ratio (i.e., statistical weight) of those components in the LTE and optically thin conditions is 1 : 3 : 5.

The chemical model of Brown et al. (1989) predicted an HNC/HCN ratio of 0.05, whereas Herbst (1978) inferred 0.9. Herbst's ratio is consistent with the one derived in cold clouds, where chemical reactions are dominated by gas-phase reactions (Wootten et al.
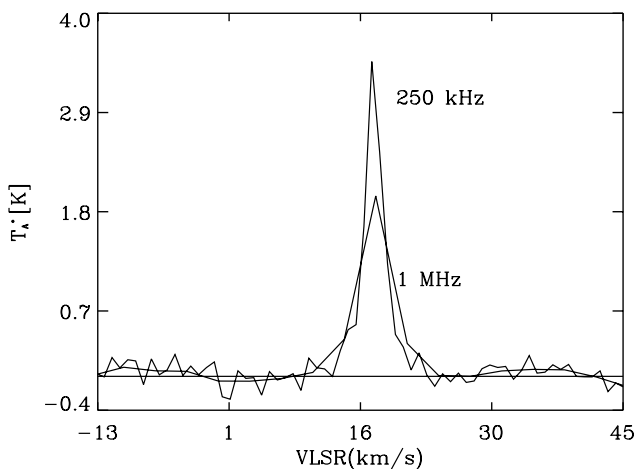
TABLE 4

Column Densities for W3(OH), W3 IRS 5, and G34.3+0.15

Molecule	Column Density (10^{13} cm^{-2})			Optical Depth (τ)			T_{ex} (K)			$N(X)/N(H_2)^a$ (10^{-10} cm^{-2})			From
	W3(OH)	W3 IRS 5	G34.3+0.15	W3(OH)	W3 IRS 5	G34.3+0.15	W3(OH)	W3 IRS 5	G34.3+0.15	W3(OH)	W3 IRS 5	G34.3+0.15	
OCS	>13.6	...	>8.8	...	...	...	16.4	...	16.4	<16.0	...	5.5	$J = 7-6$
	>2.8	...	...	...	...	...	21.0	...	...	>3.2	...	...	$J = 8-7$
C$_3$H$_2$	>0.6	>0.9	...	...	...	...	7.0	7.0	...	>0.7	...	...	...
SO	>10.7	>14.7	>16.8	...	...	...	19.3	19.3	19.3	>12.6	>12.3	>0.8	2(2)−1(1)
	>14.6	>0.1	>14.1	...	...	...	9.2	9.2	9.2	>17.2	>0.1	>8.8	3(2)−2(1)
SiO	>0.1	...	>0.4	...	...	...	7.1	...	...	>0.2	...	>0.2	...
HNCO	>0.2	>1.7	>1.9	...	...	...	7.0	7.0	7.0	>0.3	>1.4	>1.2	4(0, 4)−3(0, 3)
	...	...	2.2	...	...	...	...	...	10.6	...	...	>1.4	5(0, 5)−4(0, 4)
HCN [2−1]	7.6	0.3	3.6	4.2	3.3	3.8	5.7	3.8	4.7	8.9	2.5	2.3	...
HCN [1−1]	3.9	1.6	0.1	3.8	2.7	0.3	4.6	3.3	5.0	4.6	1.4	0.1	...
HCN [0−1]	3.2	2.9	3.1	3.3	3.2	3.9	3.8	3.7	4.8	3.8	2.5	2.0	...
H^{13}CN	0.3	0.2	2.1	0.1	0.2	0.6	5.7	3.8	4.7	0.4	0.3	1.3	...
	0.4	0.5	1.9	0.1	0.4	0.5	4.6	3.3	5.0	0.5	0.4	1.2	...
	0.5	0.3	2.0	0.3	0.2	0.5	3.8	3.7	4.8	0.6	0.3	1.3	...
HCO$^+$	12.3	5.9	6.7	4.4	3.2	4.4	6.8	3.8	6.8	14.4	5.0	4.3	...
H^{13}CO$^+$	0.3	0.3	0.7	0.2	0.2	0.3	6.8	3.8	...	0.4	0.2	0.4	...
HNC	5.5	0.4	13.0	3.4	...	4.1	4.7	4.4	7.4	6.5	...	8.2	...
HN^{13}C	0.1	...	0.5	0.1	...	0.1	4.7	...	...	0.1	...	0.3	...
N$_2$H$^+$	>0.6	...	>2.1	...	...	...	4.5	...	4.5	>0.7	...	>1.3	...
CS	20.0	>3.7	45.1	3.6	...	4.1	6.7	7.1	9.9	23.6	>3.1	28.5	^{13}CS
	29.2	...	62.8	5.5	...	6.0	6.7	...	...	34.4	...	39.7	C^{33}S
	25.9^b	...	56.3	4.8	...	5.4	6.7	...	...	30.5	...	35.6	C^{34}S
^{13}CS	0.7	...	1.2	0.1	...	0.1	6.7	...	...	0.9	...	0.8	^{13}CS
C^{33}S	0.2	...	0.4	0.1	...	0.1	6.7	...	...	0.3	...	0.2	C^{33}S
C^{34}S	1.5	...	2.7	0.2	...	0.2	6.7	...	...	1.8	...	1.7	C^{34}S
SO$_2$	>1.2	>1.9	>2.2	...	...	...	5.2	5.2	...	>1.4	>1.6	>1.4	3(1, 3)−2(0, 2)
	...	...	>224	...	...	...	...	...	246	...	...	...	27(3, 25)−26(4, 22)
HC$_3$N	...	>0.1	...	...	...	...	...	24.0	...	...	>0.1	...	27(3, 25)−26(4, 22)
CO	69309	81502	...	5.0	4.9	...	18.9	18.0	...	81606	69400	...	^{13}CO
	75564	88950	...	5.5	5.5	...	18.9	...	...	88972	75786	...	C^{17}O
	68462	80493	...	4.9	4.8	...	18.9	...	...	80610	68581	...	C^{18}O
^{13}CO	4834	6612	24696	0.6	0.6	4.8	11.4	...	...	5692	5634	15599	...
	...	...	36309	...	...	6.9	...	...	...	...	...	22936	...
C^{17}O	227	120	490	0.0	0.0	0.1	...	...	...	267	103	310	...
C^{18}O	451	430	1622	0.1	0.1	0.4	...	...	...	531	366	1025	...
From rotation diagram:													
HC$_3$N	0.4 ± 0.1	...	1.5 ± 0.1	...	...	...	16.8 ± 1	...	18.9 ± 1	0.5	...	0.9	...
CH$_3$OH	15.5 ± 0.5	...	20.0^c	...	...	...	9.7 ± 1	...	9.9	18.3	...	12.5	...
H$_2$CS	11.2 ± 1.5	...	114.8 ± 80	...	...	...	12.5	...	157.4	13.2	...	71.8	...
CH$_3$CN	0.2 ± 1.0	...	1.1 ± 0.1	...	...	...	36.2 ± 7	...	35.0 ± 3	0.3	...	0.7	...
CH$_3$CCH	5.1 ± 1.2	...	11.2 ± 0.1	...	...	...	25.5 ± 0.5	...	27.0 ± 0.2	5.1	...	13.2	...

^{a} The density $N_{H_2} = 8.5 \times 10^{22}$ cm^{-2} for W3(OH), $N_{H_2} = 1.2 \times 10^{23}$ cm^{-2} for W3 IRS 5, and $N_{H_2} = 1.6 \times 10^{23}$ cm^{-2} for G34.3+0.15 derived from $N_{H_2} = 2.7 \times 10^{21}$ cm^{-2} $\int T_R^*(^{13}CO)dv$ (Sanders et al. 1984).

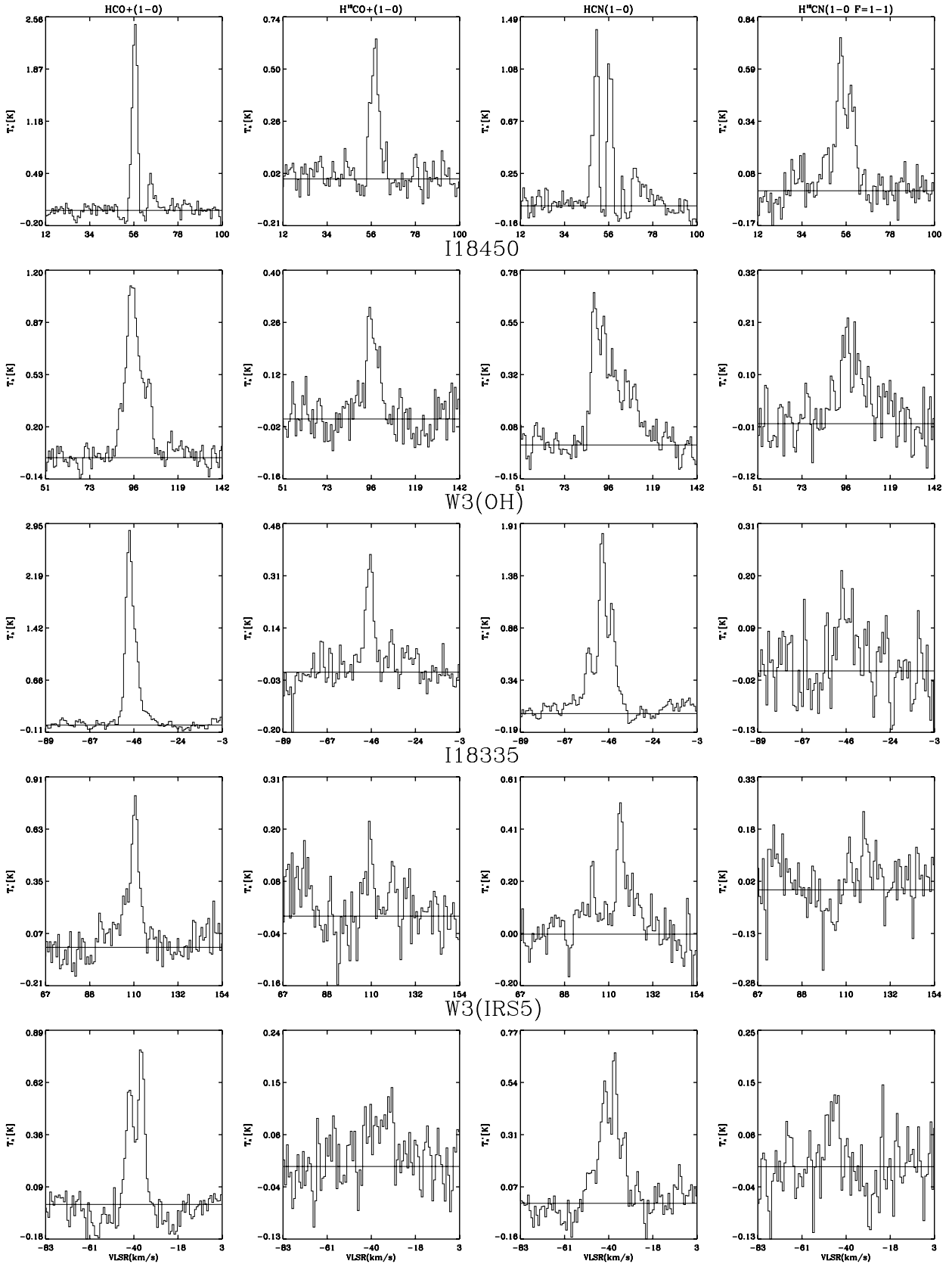^{b} Derived from 1 MHz data of C^{34}S.

^{c} From Kim et al. (2000).

FIG. 7.—Spectral lines of HCO⁺, H¹³CO⁺, HCN, and HNC observed toward G34.3+0.15, IRAS 18335−0711, IRAS 18450−0200, W3(OH), and W3 IRS 5.
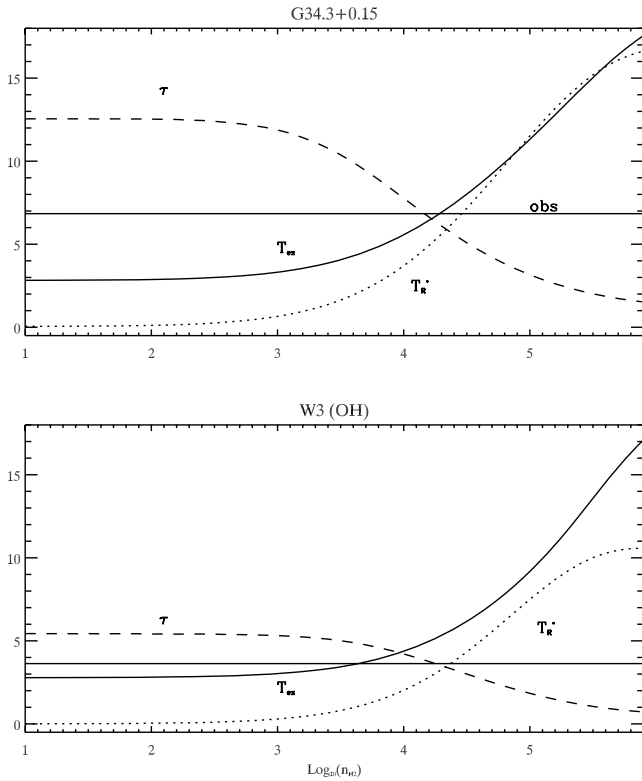
191

FIG. 8.—LVG model calculations of CS (2−1) for G34.3+0.15 and W3(OH) with a kinematic temperature of 20 K, which was obtained from CO (1−0). The horizontal lines represent observed T_R^*; solid lines represent excitation temperature; dotted lines represent the model variation of T_R^*; and dashed lines represent the variation of optical depth.

1978). A ratio higher than 1.0 is also observed in TMC-1 (Irvine & Schloerb 1984). The chemical environment seems to be different in warm and giant molecular clouds in which the HNC/HCN ratios are observed to be between 0.015 and 0.40 (Goldsmith et al. 1981). Since the small ratio in the warm clouds could not be accounted for solely by the gas-phase reaction with a precursor H_2CN^+, Goldsmith et al. (1981) proposed a neutral-atom molecular reaction, $CH_2+H\rightarrow HCN+H$. Talbi et al. (1996) introduced an exchange reaction, $H+CNH\leftrightarrow HCN+H$, to account for the low ratio with increased temperatures. The abundance variation of HCN and HNC between giant molecular clouds and cold clouds is due the particular neutral-neutral reaction, which is important for HCN formation (Millar & Freeman 1984). This neutral-neutral reaction has a small activation barrier. While the reaction is switched off in cold clouds, it proceeds efficiently in the warmer giant molecular clouds, leading to the enhancement of HCN.

In the LTE and optically thin conditions, the three hyperfine structure (hfs) ratio ($F = 0-1$, $F = 1-1$, and $F = 2-1$) in HCN is $1:3:5$, and, therefore, deviations from the intensity ratio allows one to investigate optical depth effects. Emission of $H^{13}CN$ is assumed to be optically thin, and the hyperfine ratio is expected to retain the LTE ratio. Zinchenko et al. (1993) observed a peculiar HCN hfs ratio toward an H_2O maser source S76E, where the $F = 1-1$ intensity is stronger than those of $F = 2-1$ and $F = 0-1$. They attributed it to a shielding by blueshifted low density and cold gas in the line of sight. Guilloteau & Baudry (1981) estimated $\tau = 1-3$ from the HCN lines they studied. In contrast to cold clouds, where the $F = 1-1$ component is observed to be stronger than $F = 2-1$ or $F = 0-1$, in warmer clouds the $F = 1-1$ component is observed to be weaker than the two other components

(Walmsley et al. 1982). To account for the widespread HCN anomalies, Cernicharo et al. (1984) proposed a scattering process by a diffuse envelope for emission from optically thick hot cores. The first two components are optically thick lines, whereas the last 0−1 component is an optically thin line. Radiation from the hot core of the first two components becomes scattered by the surrounding envelope, whereas the emission of the optical thin component ($F = 0-1$) penetrates without being scattered. Therefore, the 0−1 component is observed to be relatively stronger than the intensity predicted from LTE.

Among three sources we observed, an hfs ratio close to LTE was observed in W3(OH), and the $F = 0-1$ component in G34.3+0.15 was observed to be the strongest among the hfs components (Fig. 7). Our 250 kHz spectrum of G34.3+0.15 shows an evident absorption that was not seen in W3(OH) and W3 IRS 5. Hence, as will be described later in detail, the absorption/scattering by cold gas of the optically thick component ($F = 2-1$) in G34.3+ 0.15 may be responsible for the observed hfs ratio. The hyperfine ratios of $H^{13}CN$, as was supposed, are found to be consistent with the LTE ratios in the three sources, supporting our assumption that the hfs anomaly seen in the HCN lines can be explained by optical depth effects.

As shown in Figure 7, typical hyperfine ratios are found from our high-resolution (250 kHz) observations of G34.3+0.15, W3(OH), W3 IRS 5, IRAS 18450−0200, and IRAS 18335−0711 (S.-J. Kim et al. 2006, in preparation), and from Mopra surveys of IRAS 17470−2853 (Kim et al. 2002).

1. $F = 0-1 < F = 1-1 < F = 2-1$, which is the LTE ratio and is seen in W3(OH) and IRAS 17470−2853.
2. $F = 1-1 < F = 0-1 < F = 2-1$, which is seen in W3 IRS 5.
3. $F = 1-1 < F = 2-1 < F = 0-1$, which is seen in G34.3+0.15 and in IRAS 18450−0200.
4. $F = 2-1 < F = 0-1 < F = 1-1$, which is seen IRAS 18335−0711.

We also observed a strong absorption feature in the HCO^+ spectrum in G34.3+0.15. From this result, we speculate there might be a strong relationship between the HCN hfs ratio and the degree of HCO^+ absorption, an optical depth effect proposed by Cernicharo et al. (1984). Thermal overlap effects introduced by Gottlieb et al. (1975) and developed by Guilloteau & Baudry (1981) have been used to account for the anomaly. The model predicts the thermalization occurs for $N > 10^{16}$ cm^{-2}, and the LTE ratio deviates at $N > 3 \times 10^{12}$ cm^{-2}. However, the model fails to predict $R_{02} > 1$ seen from our observations in IRAS 18335−0711 (Fig. 7) and S76E (Zinchenko et al. 1993), up to $N \cong 10^{16}$ cm^{-2}, a kinetic temperature of 30 K, and $n_{H_2} = 10^5$ cm^{-2}.

Though $HN^{13}C$ was observed in G34.3+0.15 and W3(OH), it was not observed in W3 IRS 5. The nondetection indicates that the $HN^{13}C$/HNC ratio in W3 IRS 5 is lower than that in the other two sources. Since three hyperfine components of HCN were resolved by the 250 kHz observations, we derived column densities for three hyperfine components separately. As a result, a high abundance in three HCN components was obtained in W3(OH). The derived T_A^*(HNC)/T_A^*[HCN($F = 2-1$)] ratios are 0.7 and 0.4 for W3(OH) and W3 IRS 5, respectively. We obtained only a lower limit column density of HNC in W3 IRS 5, since $HN^{13}C$ was not detected. The derived HNC column density ($N = 5.68 \times 10^{13}$ cm^{-2}) in W3(OH) is close to that from submillimeter observations by Helmich & van Dishoeck (1997). This similarity indicates that HNC is an extended component. The highest abundance and optical depth of HNC were found in G34.3+0.15 (Table 4).

Intensities of CS and HCN ($F = 2-1$) in molecular clouds are quite similar, but Dickel et al. (1980) observed a strong intensity of HCN in W3 IRS 5, where weak CS lines were observed. Our results for $T_A^*(CS)/T_A^*[HCN(F = 2-1)]$ are 1.4 and 1.3–1.4 for W3 IRS 5 and W3(OH), respectively, which imply a similar density distribution for the species in the regions, as proposed by Dickel et al. (1980). The ratios are very close to each other, even though two sources seem to be in a significantly different evolutionary stages. The similarity in the ratio might be widespread in the interstellar molecular clouds, although it might be premature to conclude this.

5.4. Carbon-bearing Species—CCH, CN, C_3H_2, and HC_3N

Unsaturated carbon-chain species such as CCH, CN, and HC_3N are common components of cold molecular clouds, and they have been widely observed in dark clouds. Among them, HC_3N is a useful tracer of density of both cold clouds and hot cores.

We observed three transitions of HC_3N in W3(OH), whereas we have just one clear detection of the 10–9 transition in W3 IRS 5, where it is weak compared to that in W3(OH). With the nondetections of the other two transitions in W3 IRS 5, it implies a relatively low abundance of HC_3N in this region and suggests that the HC_3N abundance is enhanced in the later evolutionary phase (e.g., the hot core/ H II phase) rather than in the earlier phase. From the rotation diagram analysis for HC_3N of W3(OH), a rotation temperature of 17 K and a column density of 5×10^{12} cm^{-2} was derived (Table 4). In comparison with those of G34.3+0.15, temperature and density are similar when 3 mm transitions are used in the rotation analysis, but the analysis using 2 mm transitions results in a somewhat large difference in the column density. The derived column densities and temperatures from the three sources are summarized in Table 4, in which the column density of C_3H_2 is a lower limit.

5.5. Symmetric and Asymmetric Species—CH_3CN, CH_3OH, CH_3CCH, H_2CS, and HNCO

The molecules CH_3CN and CH_3CCH have been widely used to obtain physical and chemical information in hot molecular cores, as they have several transitions with wide excitation energies in close frequency ranges. Therefore, simultaneous observations of several K-ladder transitions of a molecule can reduce observational errors arising from uncertainties in telescope pointing, beam efficiency, and calibrations.

The molecule CH_3OH is a slightly asymmetric top molecule and is one of the most common species in the envelopes and the hot cores of star-forming clouds. It is a useful molecule for investigating the evolutionary stage of molecular clouds, because it has many transitions with a wide range of energies from <10 K to >100 K in the millimeter wavelength range. Transitions with energy <20 K above ground state are usually detected in the 3 mm wavelength range, allowing detailed investigations of cold envelope regions rather than warm, hot core regions. A few transitions with large energy differences are also detected.

For a given T (rotational excitation temperature) line intensities can be calculated using the following relation (Loren et al. 1981; Townes & Schawlow 1975):

$$\gamma = g(K) \frac{8\pi N f |\mu_{ij}|^2 \nu_0^2}{3ckT\Delta\nu}, \qquad (1)$$

where $g(K)$ is the K level statistical weight, f is the fractional population of each rotational level, and $|\mu_{ij}|^2 = \mu^2(J^2 - K^2)/$

$[J(2J + 1)]$. The statistical weight $g(K)$ for $K = 3, 6, 9, \ldots$, is twice those of other K lines (Townes & Schawlow 1975).

The molecule CH_3CCH has a lower dipole moment than CH_3CN, so the relative population of CH_3CCH should be much closer to being thermalized as its critical density is $n \sim 10^4$ cm^{-3}. The relatively high dipole moment of CH_3CN requires densities much higher than 10^4 cm^{-3} to approach thermalization (Askne et al. 1984; Andersson et al. 1984). CH_3CCH is abundant in halos surrounding hot cores, but CH_3CN is not seen in halos due to the low excitation temperature there (Andersson et al. 1984). Our measured CH_3CN column density, therefore, is presumed to be affected by beam dilution, resulting in a low measured density.

We detected CH_3CN and CH_3CCH in W3(OH) and G34.3+0.15, but neither was detected in W3 IRS 5 in our survey. Assuming an early evolutionary phase for W3 IRS 5, according to current chemical models, the nondetection of the two species indicates that their precursors, CH_3^+, CH_4, and H_2O may be highly depleted on the grain surface. On the other hand, according to equation (1), intensities of $K = 3n$ (where n is an integer) lines of CH_3CN based on its statistical weight are expected to be stronger than $K = 2$ components. Contrary to the theoretical prediction, however, the 6(3)–5(3) transition was found to be equal or weaker than the $K = 2$ components; however, all the transitions observed being weak prevents a definite conclusion. Similar differences between the observed line intensities and the statistical weights are also found in the prestellar object IRAS 17470−2853 (Kim et al. 2002).

A column density $N = (2.1 \pm 1.0) \times 10^{12}$ cm^{-2} and a rotation temperature (36 ± 7 K) of CH_3CN were obtained in W3(OH) using rotation diagram analysis (see Appendix). While a full rotation diagram analysis for the 3 and 2 mm transitions of CH_3CN observed in the G34.3+0.15 was performed (Kim et al. 2001), we also made a rotation diagram with the 3 mm data only to compare its column density to the result from W3(OH) (Fig. 9). This enables a direct comparison of the physical and chemical characteristics of the two regions. In the G34.3+0.15, a column density $N = (1.1 \pm 0.1) \times 10^{13}$ cm^{-2} and a temperature 35.0 ± 3 K were obtained (Table 4). While we find a good agreement between the rotational temperatures, the column densities differ by $\sim$1 order of magnitude, implying that the physical and chemical states of the warm or hot cores are not identical, though they seem to be in a similar evolutionary stage. From CH_3CCH, we obtained $N = (5.1 \pm 1.2) \times 10^{13}$ cm^{-2} and $T_{rot} = 25.5 \pm 0.5$ K in W3(OH); and $N = (1.1 \pm 0.1) \times 10^{14}$ cm^{-2} and $T_{rot} = 27.0 \pm 0.2$ K in G34.3+0.15 (Table 4). The results of W3(OH) clearly support our assumption: a low temperature and a high column density of CH_3CCH relative to CH_3CN. In comparison with OSO-20 m observations by Askne et al. (1984), who obtained a column density $N = (2.8 \pm 0.4) \times 10^{14}$ cm^{-2} and a rotational temperature 40–60 K for CH_3CCH toward G34.3+0.15 and W3(OH), our observations provide lower column density values, possibly a result of beam dilution because of the larger beam.

The scatter of the data points in the CH_3CN and CH_3CCH rotation diagrams is not very significant in the two sources (Fig. 9), except for one data point of CH_3CN and two points of CH_3CCH of W3(OH). These all have higher excitation energies and are weak lines. Three points are supposed to correspond to very hot core emission as they deviate from the model fit, which is close to a warm core model. There might be, however, some possibility of line misidentification. These lines are weak, and moreover, they were not designated as detections in G34.3+0.15, and only a 1 MHz spectrum is available (Kim et al. 2000).

Seven CH_3OH transitions were observed in W3(OH), but none of them were observed in W3 IRS 5. The 0(0)–1(−1) E and
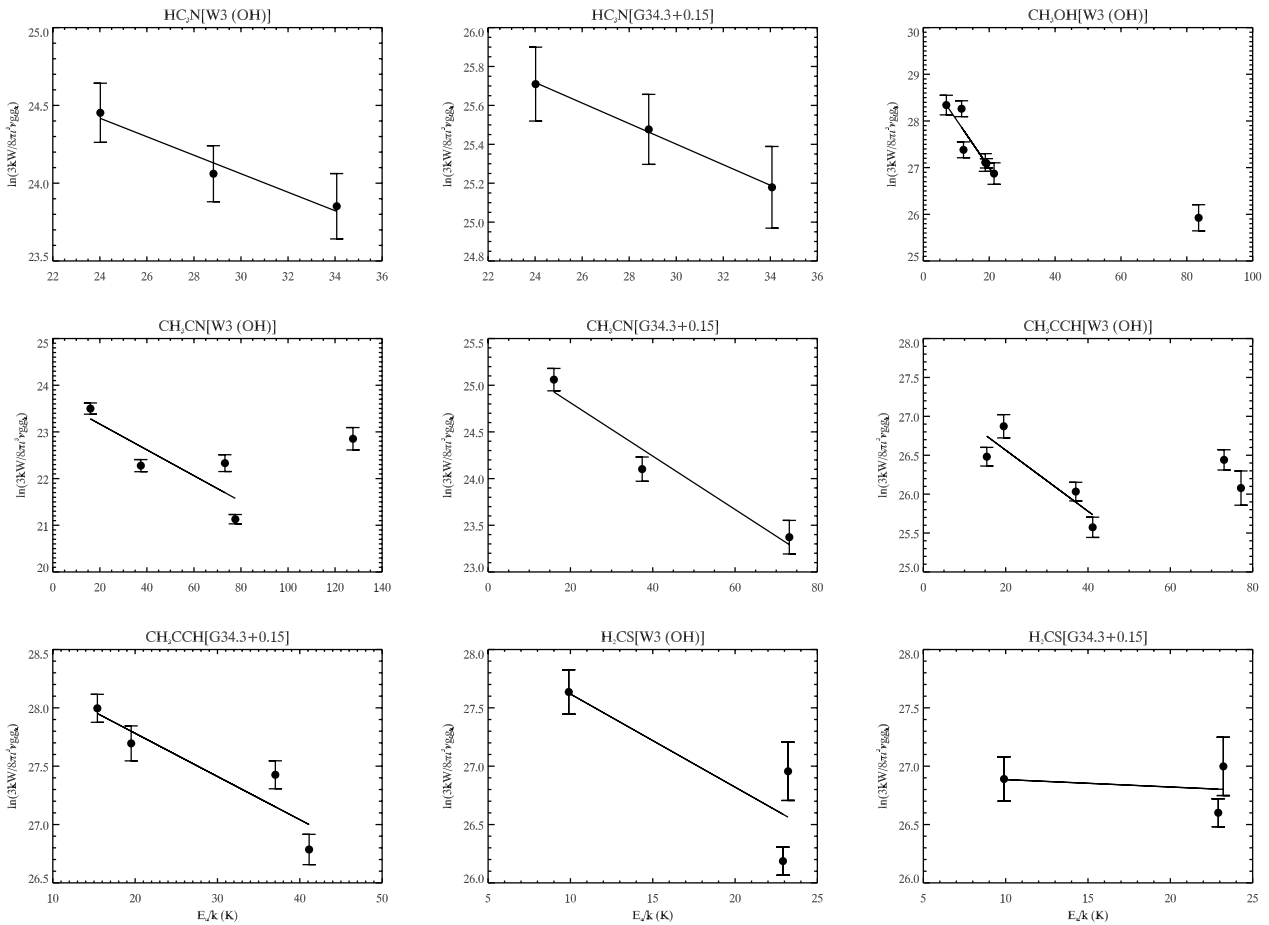
Fig. 9.—Rotation diagrams for CH₃CN, CH₃CCH, H₂CS, and CH₃OH for W3(OH) and G34.3+0.15. We have used 3 mm transitions exclusively to make direct comparisons of the excitation conditions of the molecules between G34.3+0.15 and W3(OH).

2(1)–1(1) A transitions of CH₃OH, which were not reported in the previous study of G343+0.15 (Kim et al. 2000), were detected in W3(OH). Rotation diagram analysis for the lines of A and E types yielded a rotational temperature (9.7 ± 1 K) and a column density [$(1.6 \pm 0.5) \times 10^{14}$ cm^{-2}] from W3(OH) data (Table 4). The rotational temperature and the column density appear to be in good agreement with those obtained from the lower energy transitions ($Eu/k < 45$ K) of CH₃OH observed in G34.3+0.15. We employed molecular parameters calculated by Anderson & De Lucia (1990) for the rotation diagram. As shown in Figure 9, all the transitions except for a transition with a large energy level difference are aligned in the linear fitting. Most of the detected transitions have upper energy states <20 K, and, therefore, they tend to be excited easily at low temperatures in the cold outer halos of hot molecular cores. However, the 8(0)–7(1) A+ transition, with a high energy (84 K), deviates from the linear fit. The detections of CH₃OH transitions with high excitation energies, as also in CH₃CN, tend to confirm the existence of a hot core in W3(OH). For G34.3+0.15, a two-component fit in the rotation diagram with a energy value of 45 K was more successful than a one-component fit (Kim et al. 2000, 2001).

Apart from the nondetection of CH₃CN in W3 IRS 5, the nondetection of any CH₃OH transitions in W3 IRS 5 is a remarkable result. From rotation diagram analysis for CH₃OH transitions in W3(OH) and G34.3+0.15, many rotational transitions with low excitation temperatures are found to be excited in the regions far away from the hot cores. Therefore, the nondetection

of methanol implies that methanol or its reaction partners are probably to be frozen on dust grains, which is similar to the cases of CH₃CN and CH₃CCH. Allamandola et al. (1992) found a high abundance of solid state methanol in W3 IRS 5 4 orders of magnitude larger than the gas-phase abundance, supporting our results and the evolution scenario. The derived column densities, without consideration of the interaction of dust and gas phase in the dense clouds, must underestimate the total column densities (e.g., Sandford & Allamandola 1993).

Thioformaldehyde (H₂CS) like H₂CO has two distinct rotational energy states: ortho with parallel nuclear spins and para with antiparallel. They cannot be interconverted by radiative transitions (Gardner et al. 1985). While three transitions of H₂CS, two of which are ortho, were observed in W3(OH) and G34.3+0.15, there was no detection in W3 IRS 5. An ortho-to-para ratio of 0.81 in W3(OH) and 0.48 in G34.3+0.15 were found. With nuclear spin degeneracy $g_I = 1/4$ for para and $g_I = 3/4$ for ortho (Turner 1991), we obtained a rotation temperature of 12.5 K, and a column density of 1.1×10^{14} cm^{-2} for W3(OH) using the rotation diagram analysis. In G34.3+0.15, a model fit of three 3 mm transitions gave a very high temperature of 157.5 K, and a column density of 1.2×10^{14} cm^{-2} was derived. However, since the fit as shown in Figure 9 relies on one para transition, 3(0, 3)–2(0, 2), column densities and temperatures derived from W3(OH) or from G34.3+0.15 may not be very accurate.

The HNCO [4(0, 4)–3(0, 3)] transition was observed in W3(OH), W3 IRS 5, and G34.3+0.15, but the [5(0, 5)–4(0, 4)]

line was only detected in G34.3+0.15. The [4(0, 4)–3(0, 3)] transition of W3(OH) was weak, just above the detection limit. The column density derived from HNCO [4(0, 4)–3(0, 3)] in W3 IRS 5 was close to that of G34.3+0.15, and more abundant by 1 order of magnitude compared to that in W3(OH). However, the line width in W3 IRS 5 appears to be significantly broader than that of other species. Such a broad line width was unexpected considering the nature of thermal emission for the lines. Potential implications are either a severe contamination by noise or turbulence caused by the strong outflows (Churchwell et al. 1986) in W3 IRS 5. However, with the assumption that HNCO line is thermal—using the normal line width seen in other species—we performed Gaussian fitting to derive the line width and intensity. The derived column density ignoring nonthermal effects is 1.7×10^{13} cm^{-2}, which is comparable with that of G34.3+0.15.

Jackson et al. (1984) surveyed HNCO in 18 molecular clouds including W3(OH) using 4_{04}–3_{03} and 5_{05}–4_{04} transitions, but the detections of the two transitions toward W3(OH) were negative. Solomon (1973) analyzed that the intensity ratio of $T_A^*(5$–$4)/T_A^*(4$–$3)$ is 1.56 in the case of $T_R \gg 2hBJ/k$. While his observations yield the ratio of 0.44, we have found the ratio of 0.7 toward G34.3+0.15.

6. CHEMICAL VARIATION OF W3(OH), W3 IRS 5, AND G34.3+0.15

We have so far investigated chemistry of several species of interest by categorizing them into four groups: ionized, sulfur-bearing, HCN and HNC, and symmetric and asymmetric molecules. They were grouped in accordance with characteristics of their excitation conditions, reaction processes, and internal structure. In this section, we discuss their chemistry and summarize our findings through considering the chemistry of G34.3+0.15, where complete surveys were carried out (Kim et al. 2000) and complementary observations were performed during this season.

Our observational results show remarkable chemical and intensity variations in several molecules observed in W3(OH), W3 IRS 5, and G34.3+0.15 (Fig. 10 and Table 4). In comparison with W3(OH), high abundances of saturated molecules such as CH$_3$CN and CH$_3$CCH were derived in G34.3+0.15. Molecules detected in W3 IRS 5 are mostly simple molecules such as CO and CN, but many S-bearing species were observed. The line width of SO$_2$ is about 2 times larger than that of W3(OH), indicating that W3 IRS 5 is experiencing strong shocks occurring in the earlier evolutionary stage. The most striking difference in the list of detected molecules in the three sources is the nondetection of any methanol transitions in W3 IRS 5. We expected to see a few methanol transitions, because many transitions at the 3 mm region have low upper state energies, and many of them are detected both in G34.3+0.15 and in W3(OH), and, of course, in the other star-forming regions. In the submillimeter observations conducted by Helmich et al. (1994), however, many methanol transitions are detected in W3 IRS 5, although the intensities of the transitions compared with corresponding transitions observed in W3(H$_2$O) and W3 IRS 4 are weak.

From the results of our and Helmich's observations, we have come up with the following scientific questions on the chemical properties of W3 IRS 5. Why is methanol so rare in W3 IRS 5? Is this direct evidence of adsorption onto grain surfaces? If so, why is the molecule still residing on the surface? Werner et al. (1980) argued that W3 IRS 5 is in a stage just prior to the formation of an H II region and estimated an age of $(1$–$3) \times 10^5$ yr. Based on their estimation of the age and the contemporary evolutionary scenario of molecular clouds, we would expect that hot cores (reservoirs
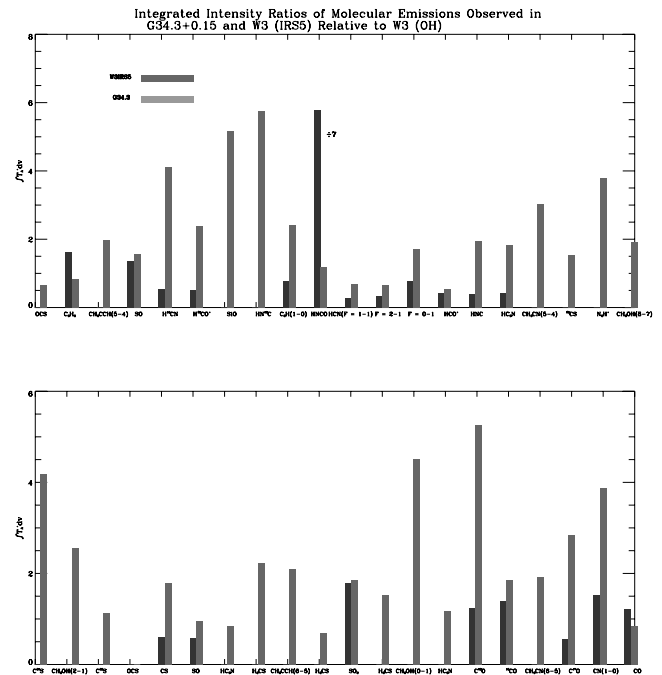

Fig. 10.—Histogram showing the variations of integrated intensities of G34.3+0.15 and W3 IRS 5 relative to W3(OH). In this plot, we considered both the 3 mm survey of this work and a previous survey (Kim et al. 2000).

of heavy species) may exist in it. However, our observational results are not consistent with the scenario. If hot cores are embedded in W3 IRS 5, some molecules that are known as a probe of hot cores, e.g., CH$_3$OH or CH$_3$CN, should be observed, but those molecules have also not been observed. Thus, does the onset of the H II phase, which is considered the next phase of the hot core stage, such as G34.3+0.15 and W3(OH), play a critical role in the formation of complex molecules including methanol? Or, are the molecules CH$_3$CN and CH$_3$OH already destroyed or converted to other species in W3 IRS 5?

The CH$_3$CN column density in W3(OH) is found to be low by 1 order of magnitude compared to G34.3+0.15, where only 3 mm transitions were used for a consistent comparison of the column densities with W3(OH) (Table 4). Since its emissions arise from hot or warm regions, the lower column density in W3(OH) compared to that in G34.3+0.15 reflects different formation environments through collisional rates, hydrogen densities, hot core size, etc. In the submillimeter (~345 GHz) wavelength region, MacDonald et al (1996) found a high CH$_3$CN column density in G34.3+0.15, 1 order of magnitude higher than in W3(OH) determined by Helmich & van Dishoeck (1997). On the other hand, it appears that the CH$_3$OH column densities and temperatures are similar in W3(OH) and G34.3+0.15 (Table 4). This may support an idea that the steady-state gas-phase reaction of CH$_3$OH, which was inferred from a low excitation temperature (10 K) derived from our rotation diagram analyses, produces uniform molecular abundances in the regions in a similar evolutionary stage.

A significant difference in the column densities of HC$_3$N was also found between W3(OH) and G34.3+0.15 (Table 4). Although a similar temperature (~15 K) for HC$_3$N was found in the two regions, our calculation yields a column density in G34.3+0.15, which is 2 orders of magnitude higher than that in W3(OH), implying an HC$_3$N abundance, like CH$_3$CN, highly dependent on excitation processes in the regions.

TABLE 5
Isotopic Ratios of W3(OH), W3 IRS 5, and G34.3+0.15

ISM	HCO$^+$/H^{13}CO$^+$	CS/^{13}CS	CS/C^{33}S	CS/C^{34}S	CO/^{13}CO	CO/C^{17}O	CO/C^{18}O	HCN/H^{13}CN[a]	HCN/H^{13}NC
W3(OH)	35	27.0	120	17	14	333	152	22	62
W3 IRS 5	21	...	...	...	12	739	187	10	...
G34.3+0.15	6[b]	37	165	21	...[c]	...	...	...	27

[a] From the HCN (1–0, $F = 2-1$) transition. Severe absorption in HCN is seen in G34.3+0.15.
[b] Absorption in HCO$^+$ results in a low value in G34.3+0.15.
[c] Absorption in CO is seen, and ^{13}CO/C^{17}O = 50 and ^{13}CO/C^{18}O = 22 are derived in G34.3+0.15.

Dickel (1980) found a decrease of CS abundance in W3 IRS 5 from CS (2–1) mapping observations and accounted for it by time-dependent ion-molecule chemistry. Our CS (2–1) map revealed that the CS peak was displaced from the W3 IRS 5 position by ∼60″ west, which is close to the strong radio emission observed by Dickel et al. (1980). W3 IRS 5 is not bright in radio emission, but it is bright in far-infrared as observed by Werner et al. (1980), suggesting that W3 IRS 5 is deeply embedded in dense dust. W3(OH) seems to be a good site to test an LTE condition, derivations of isotopic ratios, and chemical clocks, because no absorption features of CO or HCO$^+$ were seen in W3(OH) spectra, and the derived HCN hyperfine ratio is very close to the LTE ratio, which was not found in the other sources we observed.

As the variation of chemical abundances in the sources was determined, an examination of isotopic ratios and their dependence on evolutionary phase or chemical properties should be of interest (Table 5). In W3(OH), isotopic ratios of CS/^{13}CS, CS/C^{33}S, and CS/C^{34}S are found to be 27, 120, and 17, respectively. While ^{13}CS was not detected in 1 MHz observations, C^{34}S was detected in W3(OH). However, both of them were detected in 250 kHz resolution with high intensities in C^{34}S, indicating that the C^{34}S line is more optically thick than that of ^{13}CS. On the other hand, the C^{34}S line taken with 250 kHz resolution appears to be weaker than that taken with 1 MHz, suggesting observational errors in the 250 kHz data. Therefore, we used the 1 MHz data for C^{34}S and derived an isotopic ratio of 17 for CS/C^{34}S. In G34.3+0.15, isotopic ratios of 37 for CS/^{13}CS, 165 for CS/C^{33}S, and 21 for CS/C^{34}S have been derived. None of isotopic lines of ^{13}CS, C^{33}S, and C^{34}S were detected in W3 IRS 5. HCN/H^{13}CN ratios of 22 and 10 are found in W3(OH) and G34.3+0.15, respectively.

It was found that the HCO$^+$/H^{13}CO$^+$ ratios were 36, 21, and 6 in W3(OH), W3 IRS 5, and G34.3+0.15 respectively. The lower value in W3 IRS 5, compared with that in W3(OH), is probably due to weak absorption feature in the HCO$^+$ lines caused by interstellar matter in the line of sight. This absorption in G34.3+0.15 is also shown in CO (Kim et al. 2000). While the absorption in the HCO$^+$ line in W3 IRS 5 is not strong enough to give a significant effect on its column density, its absorption strength in G34.3+0.15 is significant and results in a lower value for HCO$^+$/H^{13}CO$^+$ ratio.

Derived isotopic ratios of ^{12}CO/^{13}CO for W3(OH), W3 IRS 5, and G34.3+0.15 are listed in Table 5. The following isotopic ratios have also been derived: CO/C^{17}O = 333, CO/C^{18}O = 152, and C^{18}O/C^{17}O = 22 in W3(OH); CO/C^{17}O = 739, CO/C^{18}O = 187, and C^{18}O/C^{17}O = 10 in W3 IRS 5. The strong and weak absorptions in the CO emission lines observed from G34.3+0.15 and W3 IRS 5, respectively, make a direct comparison difficult.

Wilson & Rood (1994) derived [^{12}C]/[^{13}C] ∼ 20, [^{16}O]/[^{18}O] = 250, and [^{32}S]/[^{34}S] ∼ 22 in the direction of the Galactic center. According to their study, the isotopic ratios of C and S are

found to depend on the positions sampled. Our results seem to be much closer to those in the Galactic center compared to those in the local ISM or in the solar system.

7. MAPS OF CS, HCO$^+$, HCN, AND HNC EMISSIONS

We mapped W3(OH) and W3 IRS 5 in the transitions of CS (2–1) and HCO$^+$ (1–0) to determine their distributions and sizes for chemical modeling. We also carried out similar observations for HCN and HNC to obtain their spatial distribution toward W3(OH), as the chemical reactions of these species are known to be closely related to each other.

The CS map (Figs. 5 and 11) of W3(OH) shows several small clumps to the northwest, northeast, and south of W3(OH). In the CS map of W3 IRS 5, the peak (2.4 K) is seen at ∼60″ west from the central position of our observations; and the peak position corresponds to W3 IRS 4. Dickel et al. (1980) saw that the CS peak falls to 0.5 K in the direction of W3 IRS 5. The peak position for the CS emission agrees well between this and our observations, but the peak intensity (0.9 K) of CS we measured is stronger than that of Dickel et al. (1980). The CS intensity of W3 IRS 5 was observed to be weaker than W3(OH) by a factor of 2.5.

The HCO$^+$ intensity distribution of W3(OH) shows a more diffuse emission than in CS. The HCN map of W3(OH) shows a southwest-northeast elongated distribution, whereas the HNC
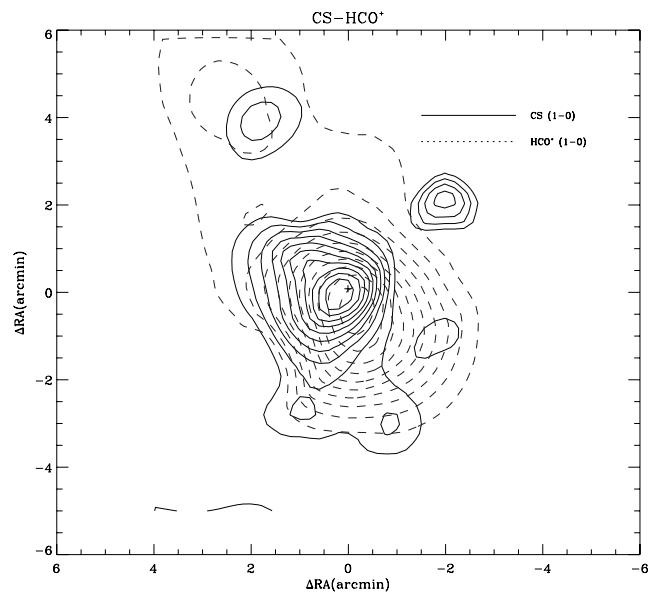

Fig. 11.—Overlaid images of HCO$^+$ and CS in W3(OH). The solid and dashed lines are for CS and HCO$^+$, respectively. This plot shows a slight deviation of the peak positions of the species, and HCO$^+$ is more widely distributed than CS.
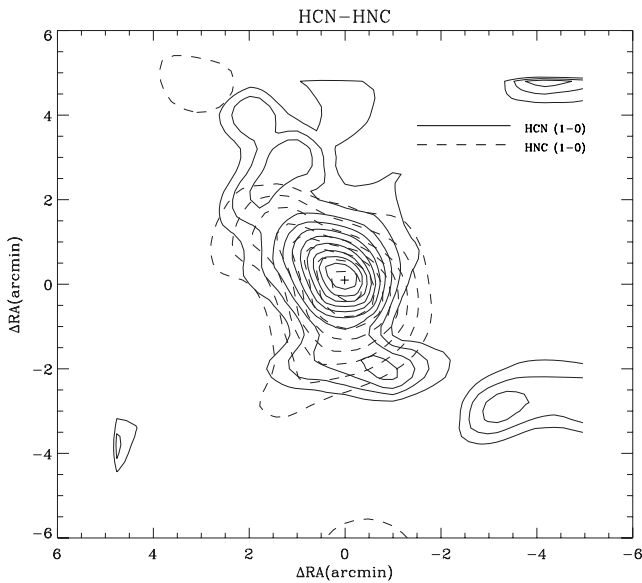
Fig. 12.—Overlaid images of HCN and HNC in W3(OH). The solid and dashed lines are for HCN and HNC, respectively. It shows an identical peak for HCN and HNC and a more dense distribution of HNC than HCN.

distribution appears to be more compact, in addition with one or two embedded clumps in the northeast and southwest directions (Figs. 5 and 12). The HCO$^+$ distribution is the most extended of the three molecules.

8. COMPARISONS WITH CHEMICAL MODELS

Chemical model calculations have been performed by several authors to explain different chemical characteristics of Orion-KL and TMC-1 (Caselli et al. 1993; Millar & Freeman 1984). Chemical models have been improved, as various laboratory measurements of molecular reactions have provided proper reaction rates between important reaction chains (Caselli et al. 1993). Recently, the ultracompact hot core, G34.3+0.15, has been comprehensively studied with model comparisons by Millar et al. (1997). Thus far, chemical model calculations have been concentrated on either cold or innermost hot cores. We have carried out the calculations for a warm core with an intermediate temperature ~35 K and for a halo with low temperatures ~10 K, because the two components are found from our observations and analyses.

Our observations at the 3 mm wavelength seem to provide a better opportunity in the study of chemistry of the warm and cold halo regions. Most emissions at this wavelength have lower energy than those of submillimeter wavelength, providing better conditions for deriving physical values such as temperature and density, which are input parameters in the model calculations. The telescope beam size at this wavelength can cover warm and halo regions at the same time. Although model calculations for a hot core with typical temperatures of >100 K and core size <0.1 pc may have some significant inaccuracies, we carried out hot core model calculations to show that low-temperature models are more consistent with the 3 mm observations than 100 K models, <0.1 pc.

In the W3(OH) model calculations, we used distinct shell layers with certain temperatures and densities, because two distinct layers were revealed from the analyses of the observed data. We used a model code developed for G34.3+0.15 by Millar et al. (1997). In the model, we used temperatures and densities derived from our observations and rotation diagram analyses. Our line survey shows that W3(OH) has at least two distinct components having different temperatures and densities. They are a cold halo with a temperature of 10 K, a volume density of 2×10^4 cm^{-3}, and a radius of 1.5 pc; and a warm/hot core with temperatures in the range of 35–100 K, densities 2×10^5, 5×10^5, or 3×10^6 cm^{-3}, and radii ranging from 0.1 to 1.0 pc. The input parameters for the model calculations are summarized in Table 6.

The visual extinction values adopted in our model calculations are somewhat different from those used for hot cores such as G34.3+0.15 by Millar et al. (1997). We used an H$_2$ and A_v relation [$A_v = N(^{13}CO)/(0.15 \times 10^{16})$ cm^{-2}] that is more valid in the cold outer region than the inner hot region. It is known that there is 1.6 mag of extinction per a column of hydrogen of 3×10^{21} cm^{-2}. The uncertainty in the visual extinction does not affect the chemical model, because 72 mag of visual extinction as used in Figure 13 is equivalent to about 300 mag in the UV, and, therefore, there are no UV photons to affect the chemistry.

Figure 13 shows results of the calculations considering grain-surface reaction routes, where the calculations were performed with a temperature of 100 K, and a density of 3×10^6 cm^{-3}. The input values for the 100 K model are assumed, as they are found to be typical in hot cores. The chemical model code was set, as a default, to perform calculations using desorption of molecules from grains in the innermost region (<0.1 pc), where evaporations of mantle components and then gas-phase reactions are known to be significant. Initial values used in the model calculations such as hydrogen density, cloud temperature, extinction, and cloud radius are given in the plot. A sharp increase of abundances occurs at an early time, ~3×10^4 yr, in this model. The abundances then drop rapidly after 10^5 yr. The rapid abundance

TABLE 6
Physical Parameters Adopted for Model Calculation of W3(OH)

Component	Mass ($M_\odot$)	$n(H_2)$ (cm^{-3})	T (K)	Outer Radius (pc)	$N(H_2)$ (cm^{-2})	A_V (mag)	Comments
Warm/hot core..........	50[a]	~10^{7a}–3×10^{6b}	100[c]–35[d]	0.1[a]	4×10^{23b}	73[e]	W3(OH)/W3(H$_2$O)
Extended halo	2×10^{3a}–6×10^{3f}	10^{5a}–10^{4g}	35–6[h]	1–1.5[i]	8.5×10^{22j}	32[e]	

[a] Wilson et al. (1991).
[b] Helmich & van Dishoeck (1994).
[c] Helmich & van Dishoeck (1994); Mauersberger et al. (1988); Wilson et al. (1991).
[d] From CH$_3$CN rotation diagram.
[e] From $A_V = N(^{13}CO)/0.15 \times 10^{16}$ [Strohacker 1978; $N(^{13}CO)$ from Helmich & van Dishoeck (1994)] and from this work.
[f] From the relation $M_{vir} = 125 FWHM^2_{HCO^+} D$ (Strong-Jones et al. 1991).
[g] From this work.
[h] From the rotation diagrams of CH$_3$OH, CH$_3$CCH, and CH$_3$CN, from the excitation temperature of HCO$^+$ and CS, and from this work.
[i] From CS (2–1) and HCO$^+$ (1–0) maps and from this work.
[j] From the relation $N_{H_2} = 2.7 \times 10^{21} \int T^R_*(^{13}CO) dv$ (Sanders et al. 1984) and from this work.
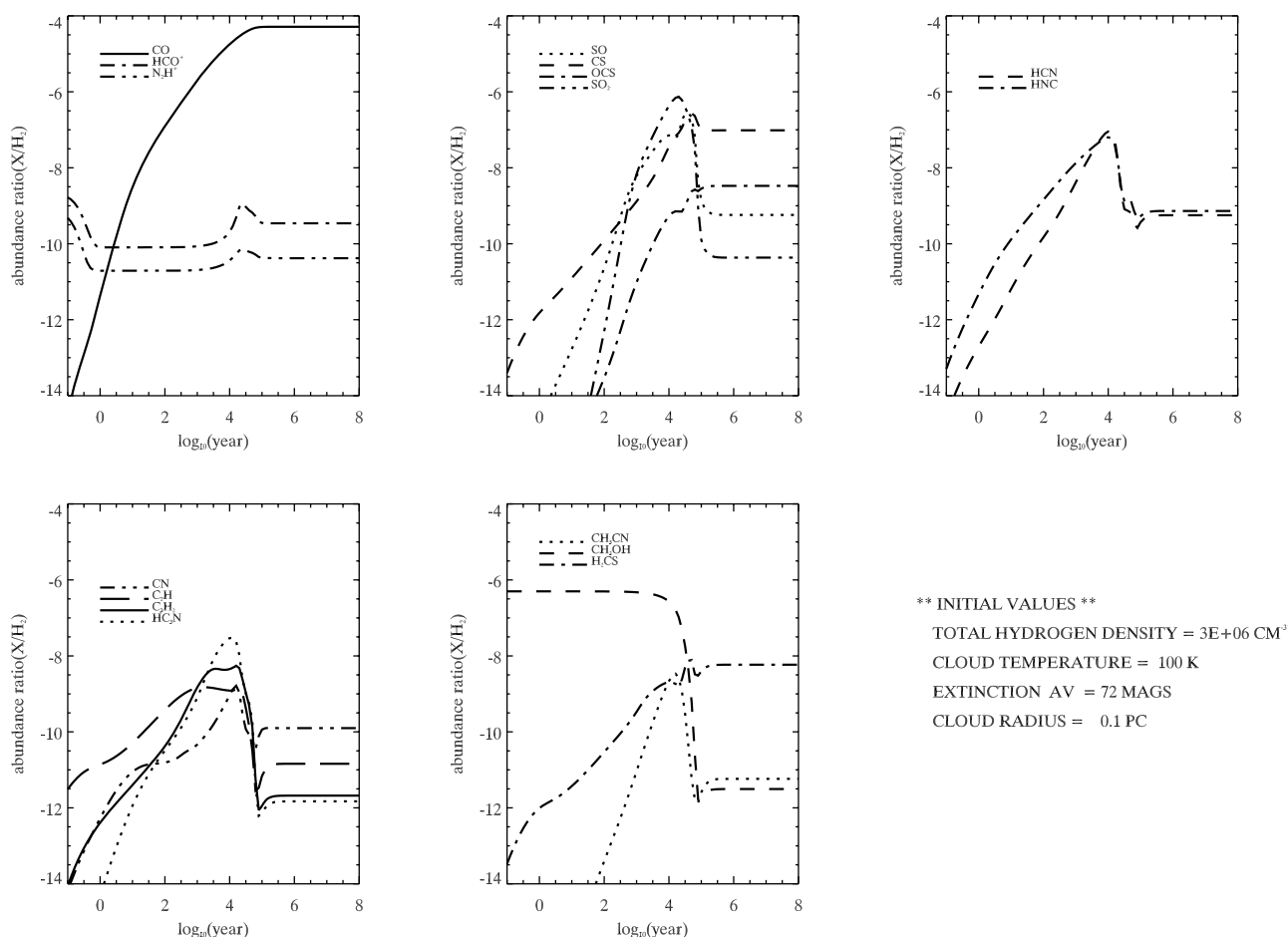
Fig. 13.—Time evolution of fractional abundances of molecules resulting from 100 K model calculations, which include grain-surface reactions and effects of mantle evaporation.

decrease in hot cores is related with the change of fractional ion density, which is inversely proportional to the square root of gas density (Caselli et al. 1993). The plot of N_2H^+ and HCO^+ shows that N_2H^+ is more abundant than HCO^+ and sharply increased at 10^4 yr.

The H_2S molecule is known to be critical in the formation of S-bearing species in a region having a temperature >100 K. H_2S is evaporated from mantle and it seems to survive about 10^3–10^4 yr. Molecules O_2 and OH are more abundant than H_2S, although the plots for these reactants are not presented here. According to Millar et al. (1997), the SH radical that is liberated through reaction with atomic hydrogen is destroyed by an H atom, creating an S atom. The S atom reacts with O_2 and OH to form SO, followed by the formation of SO_2 from SO with the reaction with OH. In a longer timescale, CS is the most abundant species after SO_2. The plot shows that SO_2 is most abundant between 10^3 and 10^4 yr, but after 10^4 yr CS is most abundant, followed by OCS, SO, and SO_2.

The HCN and HNC plot demonstrates that HNC is more abundant than HNC for $<10^3$ yr due to the recombination of H_2NC^+, which is formed by the reaction of C^+ and NH_3^+. Their abundances become almost the same up to 10^8 yr as neutral-neutral reactions become efficient for producing HCN (Millar et al. 1997).

The plot of C-containing species shows that C_2H is most abundant for $<10^3$ yr, followed by CN, C_3H_2, and HC_3N. The abun-

dances of the species drop at the core age of 10^4. After 10^5 yr, CN is most abundant, followed by C_2H, C_3H, and H_3CN. The HC_3N molecules are effectively produced in the hot gas through the reaction of C_2H_2 and CN. Its abundance has a peak at 5×10^3 yr, and its reactant C_2H_2 drops sharply at the age of 10^4 yr, although the C_2H_2 model is not included in this plot.

The plot of CH_3OH, CH_3CN, CH_3CCH, and H_2CS is most interesting, as these molecules are known to form effectively through reactions with mantle components. In the hot gas, the formation of CH_3CN is mainly driven by radiative recombination of CH_3^+ with HCN, which is also the major formation in the halo (Millar et al. 1997). H_2CS becomes the most abundant molecule after 10^4 yr, and the abundances of CH_3CN and CH_3OH are roughly equal.

Figure 14 presents plots of 60 K models for several molecules, adopting a hydrogen volume density of 5×10^5 cm^{-3}. The 60 K model calculations have been performed including the assumed input parameters, but with a lower density of hydrogen molecule and with an increased source radius compared with those of the 100 K model. The models exclude grain-surface reactions to be different from the 100 K models, because the return of mantle molecules should be less important in cooler gas.

The HCO^+ and N_2H^+ plot shows that HCO^+ is abundant by more than 1 order of magnitude compared with N_2H^+ (Table 4). The plot shows that the difference of the abundances is significant in the earlier stage in contrast to the 100 K model.
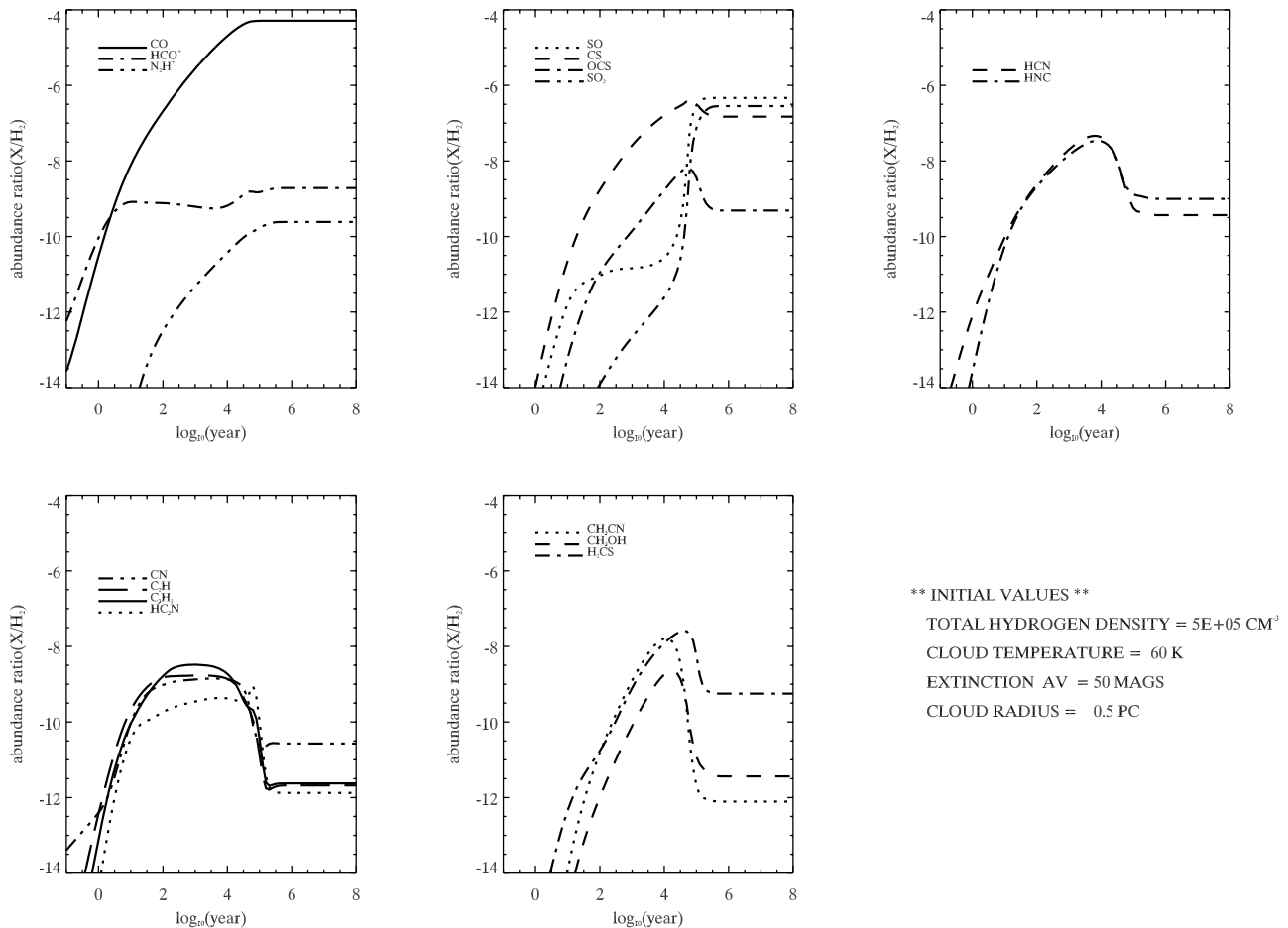
Fig. 14.—Time evolution of fractional abundances of molecules resulting from 60 K model calculations in which pure gas-phase reactions were included, but the effects of mantle evaporation were not included.

The plot of S-bearing species shows that CS is still the most abundant for $<10^5$ yr. After 10^5 yr, CS, SO, SO_2 is roughly equal, whereas the abundance of OCS is very low. The calculation of column density (Table 4) indicates that SO_2 is the least abundant molecule, followed by OCS, the abundance of which was derived from the 8–7 transition. The OCS abundance derived from the $J = 7-6$ transition in the table seems to have a somewhat large error bar, as the line is weak and contaminated by noise.

The HCN and HNC plot shows that their abundances are almost the same throughout the evolutionary time, but HNC becomes more abundant after 10^5 yr. Table 4 shows that column densities for HCN and HNC are very close each other and consistent with the model.

The plot of C-containing species shows that their abundances are almost the same for $<10^5$ yr, and then CN is the most abundant for $>10^5$ yr, as also seen in the 100 K model. We were not able to derive the column densities of CN and C_2H due to the complexity of their hyperfine structures. We could obtain a more accurate excitation temperature of HC_3N from rotation diagram analyses than an approximate value used for C_3H_2 (see Appendix). Therefore, the column density of HC_3N seems to be more reliable than C_3H_2.

The plot of CH_3OH, H_2CS, and CH_3CN shows that there are minor differences in the fractional abundances before 10^4 yr, but after 10^4 yr H_2CS is most abundant, followed by CH_3OH and CH_3CN. The model shows an increase of fractional abundances

smoothly up to 10^4 yr compared to the 100 K model. Among the three species, CH_3CN is least abundant (Table 4), which is consistent with the model. The largest abundance of H_2CS is found in G34.3+0.15, whereas CH_3OH and H_2CS abundances are almost the same in W3(OH).

As the maximum temperature of 35 K is derived from the CH_3CN rotation diagram analyses, a boundary of two components with a warm core and cold envelope was assumed to exist around 35 K with a hydrogen volume density of 2×10^5 cm^{-3} (Fig. 15). In fact, the temperature range of a warm core is known to be 30–100 K (Garay & Rodriguez 1990; Andersson & Garay 1986). Therefore, we expect that the 35 and 60 K models would produce similar results and may agree with molecular abundances of a warm core, for example, CH_3CN, in our observations. The hydrogen volume density adopted in the 35 K model calculation is very close to that found from the LVG calculation of CS. This 35 K model generates similar results to those from the 60 K model as expected, since there are only minor differences in temperature and density as well as a minor difference in A_v. The decrease of CS and increases of SO_2 and SO are seen in this model as well as seen in the 60 K model.

Figure 16 presents results of the model calculations taking a temperature of 10 K for the envelope component, which was derived from the rotational analyses of methanol lines. The HCO^+ and N_2H^+ plot shows a sharp decrease after 10^6 yr, but the plot is similar to those in the 35 and 60 K models. The plot of
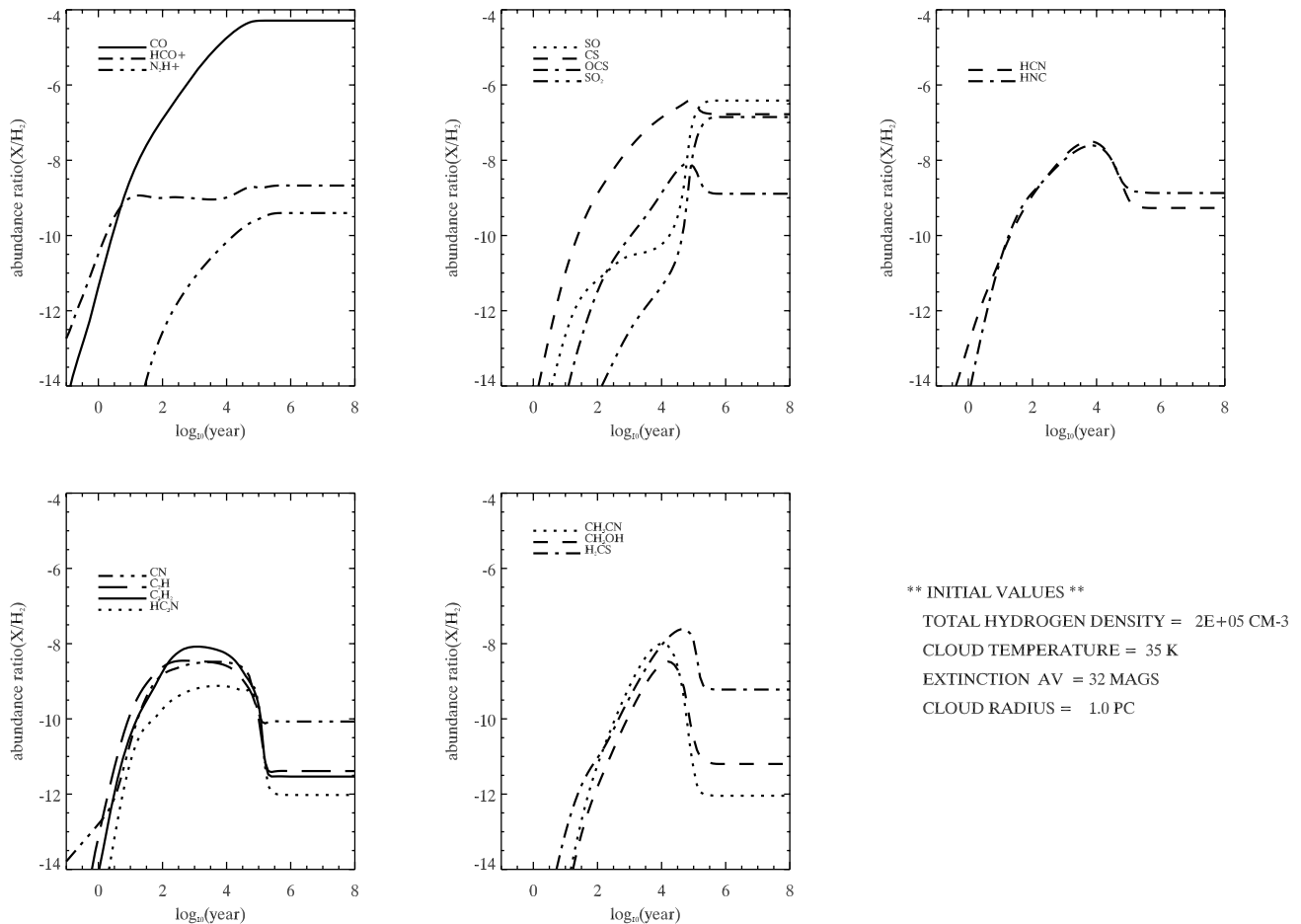
Fig. 15.—Time evolution of fractional abundances of molecules obtained from 35 K model calculations. Pure gas-phase chemical reactions only were included, but with different input parameters as shown in the plot.

S-bearing species shows that the abundances of SO and SO_2 drop sharply after 10^6 yr, and SO_2 seems to be almost destroyed. The decrease of SO is very different from the results of the 35 and 60 K models, where SO increases as CS decreases. HCN and HNC remain almost the same throughout the time span. The plot of C-containing species shows that the abundance of these species are roughly equal before 10^4 yr, since then CN is the most abundant molecule, whereas HC_3N becomes the least abundant molecule.

By examining fractional abundances derived from the theoretical modelings and the observations, we may be able to estimate the age of W3(OH). The CO is best fitted in the 10 K model with a cloud age between 10^4 and 10^5 yr. HCO^+ shows steady variation in density regardless of models except at 100 K, which is far from consideration for this molecule. The amount of ionization is determined by cosmic rays, and therefore affects overall chemical evolution. Therefore, ionized species including HCO^+ is significantly influenced by the increase of cosmic rays. We took the same cosmic-ray value for the model calculations, resulting in steady variations of HCO^+ and N_2H^+. Since 10 K was obtained from the rotation diagram of CH_3OH, we expected that a 10 K model of the molecule would produce a good agreement with observations. However, the resultant 10 K model value is found to be 4 times higher than observations. Among conceivable possibilities accounting for this difference, the hot core emission seems to be one of major reasons. The best fits of CH_3CN have been found at the 35 K model and the 60 K model.

However, H_2CS shows a large difference between the model and observation, as occurs for other S-bearing species. The rotation diagram of HC_3N results in an excitation temperature of 17 K, which comes between the warm core and halo. The best agreement of HC_3N is found at the 35 K model. Our models produce similar density variations over the ages of the clouds, and the best fits were seen at 35 K or at 10 K.

Since Orion-KL is the most extensively studied star-forming region through observations and model calculations, our observations and models have been compared with those of Orion-KL. Three distinct components having different physical and chemical characteristics are found, which are hot core, plateau, and ridge (extended and compact; Blake et al. 1987). The physical condition of the hot core of Orion-KL is not consistent with the warm and cold component of W3(OH). Emission lines from the plateau are broad indicating outflow effects. Our survey shows evidence of outflows in W3(OH) from the observations of SiO, SO_2, and SO. We are not sure whether these emissions are in fact coming from the interaction with outflows, whereas emissions from the molecules in W3 IRS 5 seem to be highly influenced by outflows evidenced by large line widths compared with W3(OH) (Table 1). Then, the most interesting region among the three components of Orion-KL is the ridge (extended and compact), because it shows relatively close agreement in temperature with the warm core of W3(OH) considering the analyses by Blake et al. (1987).
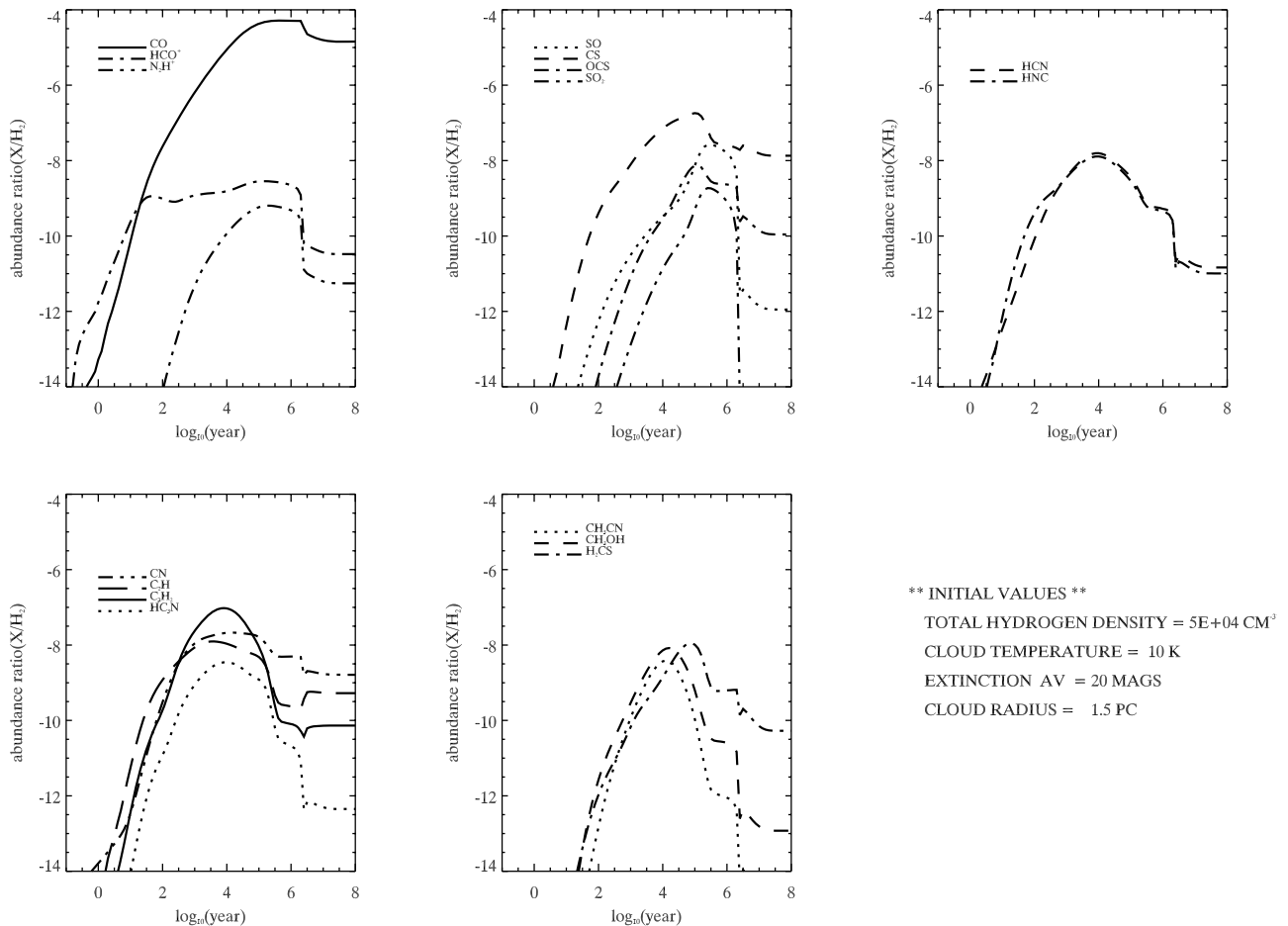
Fig. 16.—Plot of fractional abundances derived from 10 K model calculations. A temperature of 10 K was derived from the rotation diagram analysis of methanol.

The extended ridge of Orion-KL is dominated by species containing many carbons, whereas the compact ridge has more complex species including CH_3CN, CH_3OH, $HCOOCH_3$, etc. The temperature of the compact ridge is 3 times higher, and the extended ridge has a temperature 2 times higher than the warm component of W3(OH). Despite the fact that the detected molecules in W3(OH) and in the ridge components of Orion-KL are similar, there are differences in heavy molecules such as $HCOOCH_3$ and CH_3OCH_3. These undetected heavy species are known to form by ion-molecule reaction starting from CH_3OH and H_2CO, which are abundant in the compact ridge (Caselli et al. 1993). CH_3OH is detected from our survey, but none of the heavier species such as $HCOOCH_3$ and CH_3OCH_3 are detected even from the G34.3+0.15 survey of Kim et al. (2001). This implies that a temperature of 35 K for a warm component is not suitable for efficient formations of the next generation of CH_3OH and H_2CO, although Caselli et al. (1993) assume evaporation of hot cores to occur at 40 K to explain well-known early-time peaks at 3×10^4 yr. The possible reasons are (1) precursors CH_3OH and H_2CO are not abundant in the warm region of W3(OH); (2) the temperature of 35 K not enough for the efficient evaporation of those species from the grain mantles; (3) heavy species may be confined to small clumps, making it hard to detect them with our large-beam telescope, as the estimated core size of W3(OH) is very small compared to that of Orion-KL.

On the other hand, the 10 K model shows relatively high abundances of reactive C-bearing species than other models.

These carbon species are observed to be abundant in cold, dark clouds such as TMC-1, where gas-phase reaction is dominant. We could not note any significant difference among three models (10, 35, and 60 K) because those models assume that gas-phase reaction is particularly dominant in the intermediate- or low-temperature region, rather than grain-surface chemistry as applied to our 100 K model. However, we could obtain high abundances of CH_3CN and H_2CS in the 60 K model, which are presumably due to thermal effects, known to be particularly efficient in star-forming regions (Caselli et al. 1993).

Overall, the 35, 60, and 10 K models with cloud ages of 10^4–10^5 yr show better agreement with the observations compared to the 100 K model (Table 7). Helmich et al. (1994) estimated that the age for $W3(H_2O)$ is less than 10^5 yr and is probably of the order of several times 10^4 yr, which appears to be close to our estimation. However, a significant disagreement in the abundances of sulfur-bearing species such as SO, CS, OCS, SO_2, and H_2CS is found. Similar substantial disagreements between models and observations had also been found for several hot cores (Hatchell et al. 1998). The chemical abundances of sulfur-bearing species are highly dependent on initial injections of H_2S from grain surface to gas phase (Hatchell et al. 1998), but our chemical model usually adopts the fractional abundance relative to hydrogen molecule to be 10^{-6} previously found in the Orion hot core and plateau (Minh et al. 1990). Reduced initial abundances for H_2S from 10^{-6} to 10^{-8} or $\sim 10^{-7}$ produce good agreements with observations (Hatchell et al. 1998). Our model calculations and those

TABLE 7

THE RATIOS OF MODEL FRACTIONAL ABUNDANCE TO OBSERVED FRACTIONAL ABUNDANCE

MOLECULE	100 K MODEL			60 K MODEL			35 K MODEL			10 K MODEL		
	1.0×10^4 yr	1.0×10^5 yr	1.0×10^6 yr	1.0×10^4 yr	1.0×10^5 yr	1.0×10^6 yr	1.0×10^4 yr	1.0×10^5 yr	1.0×10^6 yr	1.0×10^4 yr	1.0×10^5 yr	1.0×10^6 yr
CO................	0.05	0.65	4.04	0.79	4.52	6.31	2.19	6.25	6.31	1.09	5.25	6.28
HCO^+............	0.06	0.07	0.83	0.39	0.76	1.27	0.71	1.29	1.48	1.07	1.95	1.55
N_2H^+............	0.31	0.34	1.09	0.17	1.22	3.57	1.02	4.20	6.07	1.78	8.94	7.40
SO	0.21	16.67	142.86	0.01	0.09	366.11	0.05	99.21	306.35	0.26	5.90	12.47
CS................	0.13	1.65	46.61	25.24	108.90	69.45	57.92	150.97	71.02	30.06	76.99	10.84
OCS...............	0.00	0.04	0.44	0.23	2.62	0.38	0.84	4.18	0.80	0.18	4.58	1.45
SO_2...............	0.21	321.43	4357.14	0.00	0.09	1806.43	0.03	133.43	1005.71	0.10	3.62	5.86
HCN...............	0.54	20.22	2.36	40.61	18.69	0.45	32.53	1.02	0.60	17.66	4.04	0.59
HNC...............	5.54	43.08	4.46	38.57	24.72	1.64	36.58	2.71	2.07	19.80	4.42	0.69
C_3H_2.............	2.15	63.08	36.92	47.80	8.89	0.03	82.31	3.21	0.05	1437.38	138.09	1.23
HC_3N.............	1.85	101.92	44.23	7.82	6.44	0.03	14.06	4.47	0.02	67.35	23.31	0.40
CH_3CN............	267.76	234.97	27.87	0.19	1.05	0.00	1.56	0.02	0.00	3.94	0.34	0.01
CH_3OH............	0.01	3.96	48.00	194.04	304.24	0.03	399.44	0.19	0.04	147.88	4.32	0.04
H_2CS.............	2.88	39.60	96.00	116.32	901.60	24.79	364.12	462.40	24.04	56.12	407.60	25.12

NOTES.—While fractional abundances of model calculations are calculated from a single line of sight, observational results are obtained with the beam-averaged column densities. Detailed discussions on model calculations and beam averaged column density are discussed in Thompson & MacDonald (1999).

conducted by Hatchell et al. (1998), therefore, suggest that the reduced initial abundance of H_2S should be adopted in the chemical models for molecular clouds other than Orion-KL, Sgr B2, and Sgr A.

The model code involves major assumptions in the chemical reaction rates, particularly in the desorption of molecules from the grains so that they can participate in gas-phase chemistry. While basic input physical parameters in the model calculations are properly obtained, uncertainties still exist not only in the observations but also in the model calculations in which dynamical effects, for example, are not included (Millar et al. 1997). Nevertheless, we could obtain reasonable agreements between the observations and the warm/halo models, in which we turned off grain-surface reactions.

9. SUMMARY

A total of 45 transitions from 17 species in the 1 MHz resolution observations of W3(OH) have been detected in the TRAO 3 mm surveys toward W3(OH). On the other hand, 68 transitions from 28 species are detected from detailed high-resolution (250 kHz) observations in W3(OH), whereas 33 transitions from 17 species are detected in W3 IRS 5. Several molecules and transitions missing from an earlier survey do in fact exist, such as HNCO [4(0, 4)–3(0, 3)], [5(0, 5)–4(0, 4)], CH_3OH [(2(1)–1(1) $A-$, 0(0)–1(−1) E), and SO_2 [3[(1, 3)–2(0, 2), 27(3, 25)– 26(4, 22)] toward G34.3+0.15. These are observed to be weak (∼0.3 K) except for CH_3OH [0(0)–1(−1) E]] transition, indicating that those weak lines might have been observed in the marginal detection limit of previous 1 MHz observations (Kim et al. 2000).

We estimated column densities from isotopic ratios for molecules where one transition was detected. In particular, the rotation diagram method for HC_3N, CH_3CN, and CH_3OH, where several transitions were observed was used to derive temperature and column density of the species. Lower limits to the column density for species having one or two transitions were also estimated. Significant differences in the chemical properties and abundances in the three regions are found. G34.3+0.15, in comparison with W3(OH) and W3 IRS 5, shows a high detection ratio of saturated molecules such as CH_3OH and CH_3CN as well as SO_2. We also found significant chemical differences between W3(OH) and W3 IRS 5, which is consistent with the observations by Helmich et al. (1994) and Helmich & van Dishoeck (1997), who concluded that W3 IRS 5 was in a less evolved stage and has a lower excitation temperature than W3(OH). The core sizes of W3(OH) and W3 IRS 5 are estimated to be ∼2 and 1.3 pc, respectively, from the CS (2–1) map.

Our major results are summarized as follows:

1. The chemical compositions of W3(OH) and W3 IRS 5 are quite different, implying they are in different evolutionary stages, supporting the results of Helmich et al. (1994).

2. Variations of observed line intensities in the three regions (Fig. 10 and Tables 2 and 3) seems to be evident. Among these three sources, G34.3+0.15 is found to be richest in organic species as well as other radical species.

3. Species such as SO, SO_2, and SiO are detected in W3(OH), but SiO is not detected in W3 IRS 5. Species (SO and SO_2) detected in W3 IRS 5 may result from shocks induced by outflows. However, the non detection of SiO in W3 IRS 5 is a little perplexing as its abundance is also known to be enhanced in the postshock gas. Therefore, more sensitive searches for SiO in W3 IRS 5 are required. Most of the detected lines in W3 IRS 5 are

from simple linear molecules, except for SO_2, C_3H_2, and HNCO, suggesting that W3 IRS 5 is in a state prior to the formation of the hot core or H II phase. There are significant abundance differences between the observations and model calculations, especially in the S-bearing species such as SO and SO_2. Large line widths of SO and SO_2 in W3 IRS 5 imply that W3 IRS 5 is experiencing shocks from outflows in an early evolutionary phase.

4. Absorption features in the HCO^+ (1–0) and CO (1–0) spectra of W3 IRS 5 and G34.3+0.15 indicates the presence of cold material along the line of sight or the presence of a surrounding cold collapsing envelope. For W3 IRS 5, the line feature of the CO (1–0) profile is consistent with the collapsing or infalling cloud model (Zhou et al. 1993), whereas it is not for HCO^+ (1–0). We attributed this to shocks generated by outflows active in the earlier evolutionary phase of molecular clouds, but more detailed observations are needed to test this. On the other hand, a strong absorption feature in the HCN (1–0) and HCO^+ (1–0) transitions is seen toward G34.3+0.15. These are consistent with the collapsing cloud model.

5. The nondetection of N_2H^+ toward W3 IRS 5, considering gas-phase chemical reactions in the earlier evolutionary stage, is contrary to our expectation. It is possible that the nondetection is due to depletion observed in cold dark clouds (Bergin et al. 2002).

6. H41α is detected only toward W3 IRS 5, whereas OCS, CH_3CN, H_2CS, CH_3CCH, and CH_3OH are only seen in W3(OH). The nondetection of H41α toward W3(OH) means that the line relative to W3 IRS 5 is optically thin. Its detection toward W3 IRS 5 is presumed to be due to the emission by the compact H II regions physically associated with W3 IRS 5. A detection of H41α having broader FWHM (21 km s^{-1}) and high energy (Eu = 94 K) in the direction of W3 IRS 5, and its nondetection toward W3(OH), is far from our expectations. We tentatively attribute the detection of the recombination line in W3 IRS 5 to several compact H II regions physically associated with W3 IRS 5, based on its emission velocity (VLSR = −40 km s^{-1}). The ultracompact H II regions W3F or W3M found near IRS 7 and IRS 5 (Colley 1980) are possible candidates.

7. The 5 σ extent of the CS (2–1) and HNC (1–0) maps of W3(OH) is estimated to be ∼0.6 pc at a distance of 2.2 kpc. Although HCN distribution is similar to CS, it is slightly elongated (Fig. 5). In the direction of W3 IRS 5 a large clump comparable to that of central clump of W3(OH) is identified at ∼60″ west from the central position. The HCO^+ (1–0) image of W3(OH), compared to CS and HNC, shows rather diffuse distribution having a radius of about 1.5 pc.

8. We confirm that the chemical variation of molecular clouds in different evolutionary phases is evident, as predicted by chemical models. However, we emphasize the importance of more sensitive measurements, especially for H_2S, and for consideration of shock chemistry to provide more robust predictions of S-bearing species.

APPENDIX

COLUMN DENSITIES

A1. LTE: FROM MEASUREMENTS OF OPTICALLY THIN LINES

When optically thin lines are detected, we can derive column density and excitation temperature from the relative intensity ratios:

$$T_R^* = \eta_f [J(T_{ex}) - J(T_{bg})](1 - e^{-\tau}), \tag{A1}$$

with

$$J(T) = T_0 \left(e^{h\nu/kT} - 1 \right)^{-1}, \tag{A2}$$

where η_f is the beam-filling factor, which is 1 for extended source, and $T_0 = h\nu/k$.

For an optically thick line ($\tau \gg 1$),

$$T_{ex} = T_0 \left\{ \ln \left[\frac{T_0}{T_R^* + J(T_{bg})} + 1 \right] \right\}^{-1}. \tag{A3}$$

On the other hand, if the excitation temperature, T_{ex}, is known, then the optical depth is given by

$$\tau_{iso} = - \ln \left[1 - \frac{T_R^*}{J(T_{ex}) - J(T_{bg})} \right]. \tag{A4}$$

The optical depth, τ, is related to the column density and excitation temperature by

$$\tau = \frac{8\pi^3 \mu^2 SN}{3h\Delta vQ} (\exp^{-h\nu/kT_{ex}} - 1) \exp^{-E_u/kT_{ex}}. \tag{A5}$$

The column density of an optically thin, isotopic line is given by

$$N_{iso} = \frac{3h\Delta v_{iso}\tau_{iso}Q(T_{ex})}{8\pi^3 \mu_{iso}^2 S_{iso}(\exp^{h\nu/kT_{ex}} - 1) \exp^{-E_u/kT_{ex}}}. \tag{A6}$$

In the high-temperature limit ($hB \ll kT$) diatomic and linear molecules have a partition function,

$$Q(T_{ex}) = \sigma \frac{kT_{ex}}{hB}, \tag{A7}$$

where $\sigma = 1$ for HCN, HNC, HCO$^+$, and SiO, and $\sigma = 3$ for HC$_3$N to account for the hyperfine splitting and $^3\Sigma$ species such as SO and C$_2$S (Blake et al. 1987; Turner 1991). In the high-temperature limit ($hA \ll kT, hB \ll kT$) the partition function for the symmetric molecules CH$_3$CN and CH$_3$OH have the form (Turner 1991)

$$Q_{rot} = \sigma [\pi(kT_{ex})^3/h^3 AB^2]^{1/2}, \tag{A8}$$

where $\sigma = 1/3$ (Blake et al. 1987) and $\sigma = 2/3$ (Turner 1991). The CH$_3$OH molecule has torsional, A, and E states. Assuming that they have the same partition function value,

$$Q_{rot} = Q_{rot}(A) + Q_{rot}(E) = 2[\pi(kT_{ex})^3/h^3 AB^2]^{1/2}. \tag{A9}$$

From equation (A5) we can also relate the optical depth of the main line and the isotope by

$$\frac{\tau_{main}}{\tau_{iso}} = \frac{N_{main}\Delta v_{iso}(\exp^{h\nu_{main}/kT_{ex}} - 1) \exp^{-E_u(main)/kT_{ex}}}{N_{iso}\Delta v_{main}(\exp^{h\nu_{iso}/kT_{ex}} - 1) \exp^{-E_u(iso)/kT_{ex}}}. \tag{A10}$$

From equation (A1), the ratio of the measured intensities, R, is given by

$$R = \frac{T^*_{R,\,\mathrm{main}}}{T^*_{R,\,\mathrm{iso}}} \sim \frac{1 - e^{-\tau_{\mathrm{main}}}}{1 - e^{-\tau_{\mathrm{iso}}}}, \tag{A11}$$

which lets us calculate τ_{main},

$$\tau_{\mathrm{main}} = -a \log\left\{1 - [1 - \exp(-\tau_{\mathrm{iso}})]R\right\}. \tag{A12}$$

From equation (A10), the column density of the main line is given by

$$N_{\mathrm{main}} = \frac{N_{\mathrm{iso}} \Delta v_{\mathrm{main}} \exp(h\nu_{\mathrm{iso}}/kT_{\mathrm{ex}} - 1) \exp[-E_u(\mathrm{iso})/kT_{\mathrm{ex}}]}{\tau_{\mathrm{iso}} \Delta v_{\mathrm{iso}} \exp(h\nu_{\mathrm{main}}/kT_{\mathrm{ex}} - 1) \exp[-E_u(\mathrm{main})/kT_{\mathrm{ex}}]}, \tag{A13}$$

and the abundance ratio X is determined by

$$X = \frac{N_{\mathrm{main}}}{N_{\mathrm{iso}}}. \tag{A14}$$

A2. LOWER LIMIT COLUMN DENSITY

For molecules having only one detected transition without isotopic species, we derive a lower limit to the column densities by assuming that the rotation temperature of linear molecules is $T_{\mathrm{rot}} = E_u/k$, and for symmetric or slightly asymmetric tops is $T_{\mathrm{rot}} = (2/3)E_u/k$ (see MacDonald et al. 1996). Then, a lower limit to the column density of linear molecules is given by

$$N_{\mathrm{min}} = \frac{3k \int T^*_R\, dv}{8\pi^3 \nu \mu^2 S g_I g_K} Q(T_{\mathrm{rot}}) e, \tag{A15}$$

and for symmetric or slightly asymmetric top molecules by

$$N_{\mathrm{min}} = \frac{3k \int T^*_R\, dv}{8\pi^3 \nu \mu^2 S g_I g_K} Q(T_{\mathrm{rot}}) e^{3/2}. \tag{A16}$$

A3. ROTATION DIAGRAM

Column densities and rotational temperatures of molecules with several detected transitions are derived from the rotation diagram method with several assumptions: $T_{\mathrm{rot}} \gg T_{\mathrm{bg}}$, the lines are optically thin, and all the level populations are in thermal equilibrium (Blake et al. 1987; MacDonald et al. 1996):

$$\frac{N_u}{g_u} = \frac{3k \int T^*_R\, dv}{8\pi^3 \nu \mu^2 S g_I g_K}, \tag{A17}$$

and

$$\frac{N_u}{g_u} = \frac{N_T}{Q(T_{\mathrm{rot}})} \exp^{-E_u/kT_{\mathrm{rot}}}. \tag{A18}$$

Setting equation (A17) equal to equation (A18), and taking natural logs, one finds the relationship

$$\ln \frac{3k \int T^*_R\, dv}{8\pi^3 \nu \mu^2 S g_I g_K} = \ln \frac{N_T}{Q(T_{\mathrm{rot}})} - \frac{E_u}{kT_{\mathrm{rot}}}, \tag{A19}$$

where ν is the transition frequency, μ is the permanent electric dipole moment, k is the Boltzmann constant, g_I and g_K are degeneracies, E_u is the upper state energy, S is the line strength, $Q(T_{\mathrm{rot}})$ is the partition function for the rotational excitation temperature T_{rot}, N_T is total column density; and $\int T^*_R\, dv$ is the integrated line intensity. The reduced nuclear spin weight, g_I, and K-level degeneracy, g_K, of linear molecules are both 1. For C_{2v} species such as CH_3CN and CH_3CCH, however, $g_K = 1$ for $K = 0$ and $g_K = 2$ for $K \neq 0$, and $g_I = 1/2$ for $K = 3n$ and $g_I = 1/4$ for $K \neq 3n$ (where n is an integer; Turner 1991).

If several lines are observed, it is possible to fit a straight line to a plot of $\ln N_u/g_u = \ln N_T/Q_{\exp}(-E_u/kT)$ against E_u/k, where N_u is the upper state column density, to yield the temperature from the slope and the column density from the intercept. Therefore, the total column density can be derived by the relation

$$N_T = \exp(y_p) Q(T_{\mathrm{rot}}), \tag{A20}$$

where y_p is the intercept on the y-axis obtained from the fit to equation (A19).

REFERENCES

Allamandola, L. J., Sandford, S. A., & Tielens, G. G. M. 1992, ApJ, 399, 134
Anderson, T., & De Lucia, F. C. 1990, ApJS, 72, 797
Andersson, M., Askne, J., & Hjalmarson, A. 1984, A&A, 136, 243
Andersson, M., & Garay, G. 1986, A&A, 167, L1
Askne, J., Hoglund, B., Hjalmarson, A., & Irvine, W. M. 1984, A&A, 130, 311
Bachiller, R. 1996a, IAU Symp. 178, Molecules in Astrophysics: Probes and Processes, ed. E. F. van Dishoeck (Dordrecht: Kluwer), 103
———. 1996b, ARA&A, 34, 111
Bally, J., & Lada, C. 1983, ApJ, 265, 824
Bergin, E. A., Alves, J., Huard, T. L., & Lada, C. J. 2002, ApJ, 570, L101
Blake, G. A., Mundy, L. G., Carlstrom, J. E., Padin, S., Scott, S. L., Scoville, N. Z., & Woody, D. P. 1996, ApJ, 472, L49
Blake, G. A., Sutton, E. C., Masson, C. R., & Phillips, T. G. 1986, ApJS, 60, 357
———. 1987, ApJ, 315, 621
Brown, R. D., Burden, F. R., Cuno, A. 1989, ApJ, 347, 855
Campbell, M. F., Butner, H. M., Harvey, P. M., Evans, N. J., II, Campbell, M. B., & Sabbey, C. N. 1995, ApJ, 454, 831
Caselli, P., Hasegawa, T. I., & Herbst, E. 1993, ApJ, 408, 548
Cernicharo, J., Castets, A., Duvert, G., & Guilloteau, S. 1984, A&A, 139, L13
Cernicharo, J., Guelin, M., & Kahane, C. 2000, A&AS, 142, 181
Charnley, S. B. 1997, ApJ, 481, 396
Charnley, S. B., Kress, M. E., Tielens, A. G. G. M., & Millar, T. J. 1995, ApJ, 448, 232
Churchwell, E., Wood, D., Myers, P. C., & Myers, R. V. 1986, ApJ, 305, 405
Colley, D. 1980, MNRAS, 193, 495
Cummins, S. E., Linke, R. A., & Thaddeus, P. 1986, ApJS, 60, 819
Dickel, H. R. 1980, ApJ, 238, 829
Dickel, H. R., & Dickel, J. R., Wilson, W. J., & Werner, M. W. 1980, ApJ, 237, 711
Dreher, J. W., & Welch, W. J. 1981, ApJ, 245, 857
Forster, J. R., Caswell, J. L., Okumura, S. K., Hasegawa, T., & Ishiguro, M. 1990, A&A, 231, 473
Garay, G., & Rodriguez, L. 1990, ApJ, 362, 191
Gardner, F. F., Hoglund, B., Shukre, C., Stark, A. A., & Wilson, T. L. 1985, A&A, 146, 303
Goldsmith, P. F., Langer, W. D., Ellder, J., Kollberg, E., & Irvine, W. 1981, ApJ, 249, 524
Gordon, M. A. 1987, ApJ, 316, 258
Gottlieb, C. A., Lada, C. J., Gottlieb, E. W., Lilley, A. E., & Litvak, M. M. 1975, ApJ, 202, 655
Gregersen, E. M., Evans, N. J., II, Zhou, S., & Choi, M. 1997, ApJ, 484, 256
Guilloteau, S., & Baudry, A. 1981, A&A, 97, 213
Hatchell, J., Thompson, M. A., Millar, T. J., & MacDonald, G. H. 1998, A&A, 338, 713
Helmich, F. P., Jansen, D. J., De Graauw, Th., Groesbeck, T. D., & van Dishoeck, E. F. 1994, A&A, 283, 626
Helmich, F. P., & van Dishoeck, E. F. 1997, A&AS, 124, 205
Herbst, E. 1978, ApJ, 222, 508
Herbst, E., Smith, D., & Adams, N. G. 1984, A&A, 138, L13
Imai, H., et al. 2000, ApJ, 538, 751
Irvine, W. I., & Schloerb, F. P. 1984, ApJ, 282, 516
Jackson, J. M., Armstrong, J. T., & Barrett, A. H. 1984, ApJ, 280, 608
Jaffe, D. T., Hildebrand, R. H., Keene, J., & Whitcomb, S. E. 1983, ApJ, 273, L89
Jewell, P. R., Hollis, J. M., Lovas, F. J., & Snyder, L. E. 1989, ApJS, 70, 833
Johansson, L. E. B., et al. 1984, A&A, 130, 227
Kawaguchi, K., Kasai, Y., Ishikawa, S., & Kaifu, N. 1995, PASJ, 47, 853
Keto, E., Proctor, D., Ball, R., Arens, J., & Jernigan, G. 1992, ApJ, 401, L113
Kim, H.-D., Cho, S.-H., Chung, H.-S., Kim, H.-R., Roh, D.-G., Kim, H.-G., Minh, Y.-C., & Minh, Y.-K. 2000, ApJS, 131, 483
Kim, H.-D., Cho, S.-H., Lee, C.-W., & Burton, M. B. 2001, J. Korean Astron. Soc., 34, 167

Kim, H.-D., Ramesh. B., & Burton, M. G. 2002, Publ. Astron. Soc. Australia, 19, 505
Loren, R. B., Mundy, L., & Erickson, N. R. 1981, ApJ, 250, 573
Lovas, F. J. 1992, J. Phys. Chem. Ref. Data, 21, 181
MacDonald, G. H., Gibb, A. G., Habing, R. J., & Millar, T. J. 1996, A&AS, 119, 333
Mardones, D., Myers, P. C., Tafalla, M., Willner, D., Bachiller, R., & Garay, G. 1997, ApJ, 489, 719
Mauersberger, R. Wilson, T. L., & Henkel, C. 1988, A&A, 201, 123
Millar, T. J., & Freeman, A. 1984, MNRAS, 207, 405
Millar, T. J., Herbst, E., & Charnley, S. B. 1991, ApJ, 369, 147
Millar, T. J., MacDonald, G. H., & Gibb, A. G. 1997, A&A, 325, 1163
Minh, Y. C., Ziurys, L. M., Irvine, W. M., & McGonagle, D. 1990, ApJ, 360, 136
Nummelin, A., Dickens, J. E., Bergman, P., Hjalmarson, A., Irvine, W. M., Ikeda, M., & Ohishi, M. 1998, A&A, 337, 275
Persi, P., Busso, M., Corcione, L., Ferrari-Toniolo, M., & Marenzi, A. R. 1996, A&A, 306, 587
Prasad, S. S., & Huntress, W. T., Jr. 1982, ApJ, 260, 590
Rawlings, J. M. C., Taylor, S. D., & Williams, D. A. 2000, MNRAS, 313, 461
Roberts, D. A., Crutcher, R. M., & Troland, T. H. 1997, ApJ, 479, 318
Sams, B. J., III, Moran, J. M., & Reid, M. J. 1996, ApJ, 459, 632
Sanders, D. B., Solomon, P. M., & Scoville, N. Z. 1984, ApJ, 276, 182
Sandford, S. A., & Allamandola, L. 1993, ApJ, 417, 815
Schilke, P., Groesbeck, T. D., Blake, G. A., & Phillips, T. G. 1997, ApJS, 108, 301
Snyder, L. E., & Watson, W. D. 1977, ApJ, 212, 79
Solomon, P. M. 1973, ApJ, 185, L63
Strohacker, O. C. 1978, M.S. thesis, Univ. Texas at Austin
Strong-Jones, F. S., Heaton, B. D., & Little, L. T. 1991, A&A, 251, 263
Sutton, E. C., Blake, G. A., Masson, C. R., & Phillips, T. G. 1985, ApJS, 58, 341
Sutton, E. C., Jaminet, P. A., Danchi, W. C., & Blake, G. A. 1991, ApJS, 77, 255
Talbi, D., Ellinger, Y., & Herbst, E. 1996, A&A, 314, 688
Thompson, M. A., & MacDonald, G. H. 1999, A&AS, 135, 531
Townes, C. H., & Schawlow, A. L. 1975, Microwave Spectrocopy (New York: Dover)
Turner, B. E. 1989, ApJS, 70, 539
———. 1991, ApJS, 76, 617
———. 1995, ApJ, 449, 635
Ulich, B. L., & Haas, R. W. 1976, ApJS, 30, 247
van Dishoeck, E. F., & Blake, G. A. 1986, ApJS, 62, 109
———. 1988, ApJ, 334, 771
———. 1998, ARA&A, 36, 317
van Dishoeck, E. F., Blake, G. A., Jansen, D. J., & Groesbeck, T. D. 1995, ApJ, 447, 760
Walmsley, C. M., Churchwell, E., Nash, A., & Fitzpatrick, E. 1982, ApJ, 258, L75
Walsh, A. J. Burton, M. G., Hyland, A. R., & Robison, G. 1998, MNRAS, 301, 640
Werner et al. 1980, ApJ, 242, 601
Wilson, T. L., Johnston, K. J., & Mauersberger, R. 1991, A&A, 251, 220
Wilson, T. L., & Rood, R. T. 1994, ARA&A, 32, 191
Womack, M., Ziurys, L. M., & Wyckoff, S. 1992, ApJ, 387, 417
Wootten, A., Evans, N. J., II, Snell, R., & vanden Bout, P. 1978, ApJ, 225, L143
Wynn-Williams, C. G., & Becklin, E. E. 1974, PASP, 86, 5
Wyrowski, F., Schilke, P., Walmsley, C. M., & Menten, K. M. 1999, ApJ, 514, L43
Zhou, S., Evans, N. J., II, Kompe, C., & Walmsley, C. M. 1993, ApJ, 404, 232
Zinchenko, I., Forsstrom, V., & Mattila, K. 1993, A&A, 275, L9
Ziurys, L. M., & McGonagle, D. 1993, ApJS, 89, 155